Università degli Studi di Ferrara

DOCTORAL COURSE IN:
PHYSICS

CYCLE XXXII

COORDINATOR Prof. Luppi Eleonora

An experimental study of novel schemes for low-energy-threshold and low-background particle detection in rare gas crystals

Scientific/Disciplinary Sector (SDS): FIS/01

Supervisor:
Prof. Calabrese Roberto

Candidate:
Guarise Marco

Co-supervisor:
Prof. Tomassetti Luca

Years 2016 – 2019

Author's declaration

The undersigned, Marco Guarise, confirms that the entire work presented and discussed in this thesis is my own. The indication of the sources occurs where information has been derived from other authors.

Ferrara, 21 February 2020

The work contained in this thesis has been used in the following papers:

- A.F. Borghesani, et al., Cathodo- and radioluminescence of Tm^{3+}:YAG and Nd^{3+}:YAG in an extended wavelength range *J. Lumin.* 190, 29-36 (2017)
- F. Chiossi, et al., A new technique for infrared scintillation measurements *NIM A* 855, 13-15 (2017)
- M. Guarise, et al., Experimental setup for the growth of solid crystals of inert gases for particle detection *Rev. Sci. Instrum.* 88, 113303 (2017)
- C. Braggio, et al., Axion dark matter detection by laser induced fluorescence in rare-earth doped materials *Sci. Rep.* 7, 15168 (2017)
- M. Guarise, et al., Novel approaches in low energy threshold detectors for Dark Matter searches *Nucl. Instrum. Methods Phys. Res. A* 61313 (2018);

- G. Carugno et al.,Dark matter search by laser spectroscopy *Proc. 20th International Conference and School on Quantum Electronics: Laser Physics and Applications* 11047, 110470Q (2019);
- M. Guarise, et al., Particle detection in rare gas solids: DEMIURGOS experiment *Nucl. Instrum. Methods Phys. Res. A 162434* (2019);
- M. Guarise, et al.,A feasibility study for a low-energy-threshold particle detector in a xenon crystal *J. Instrum. 012P-0120* (2020);

Contents

Introduction

Nowadays, theories such as the Standard Model of particle physics (SM) or the general relativity are our best comprehension of the Universe, but, as we also know, there is also a lot of physics beyond these models that has to be discovered. One of the largest issue that we have to deal with, is the problem of the "lacking mass" of the Universe. From observations on all astrophysical and cosmological scales, an outstanding result is in fact that there is something with a gravitational effect which is not visible. Historically this hidden part of the Universe has been called Dark Matter (DM) because it does not absorb or emit electromagnetic radiation at any wavelength and it only interacts through gravitational force and, likely, the weak force. Furthermore it is surprising that the major part of the matter in galaxies and in galaxy clusters consists of DM while the ordinary visible mass represents only a minor fraction. Many observations indeed tell us that, locally, more than 84% of the matter that constitutes the Milky Way is not composed of the ordinary matter which contributes for only $\sim$15%. Moreover, the overall Universe composition is quite more complicated because of the presence of also the dark energy which is something that permeates all the Cosmos and counts for $\sim$ 70% of the Universe's energy.

From the point of view of the experimental physics there is a lot of work to do. The progress in physics, and particularly in particle physics, has in fact always been closely linked with improving detection techniques and breakthrough discoveries have been possible because of the innovation in detection. Starting from the gold-

leaf electroscope, which was the first ionizing-radiation detector, many advances have been done in the last century passing through the Geiger-Müller counter, the cloud, bubble and drift chambers and the semiconductor devices. Nowadays different scenarios are depicted as dark matter solutions and different theoretical models suggest a various panorama in which many candidates are possible. Many different kind of detectors are thus necessary to improve the devices developed in the last decades which are currently probing only few mass ranges of the possible candidates while many areas are instead not yet studied. To be able to probe the largest number of dark matter constituents, that could be as light as 10^{-22} eV, it is thus necessary to improve the performances of the current detectors making them more efficient in terms of energy threshold and volume. In this view, the biggest challenge in the scientific community is to develop innovative detectors that exploit the frontier technology in hybrid regimes in order to reach the best performances. The background scenario, in fact, was recently explained in the community report "US Cosmic Vision" [1] that has called out the importance of a broad dark matter search program across new directions also through small experiments in the near future. A comprehensive exploration of this unknown phenomena requires thus novel approaches and new ideas. Hence, innovative Research and Development (R&D) studies are of paramount importance in this view.

The purpose of this thesis work is to investigate novel detection approaches characterized by a low-energy threshold and low-background in a large active volume exploiting rare gas solids as detector media. In this manuscript I will present the preliminary tests and measurements, and their important aspects related to a future development of a working detector.

In the first chapter (1), the dark matter existence will be discussed introducing the dark matter paradigm known as the *"missing mass problem"*. The main proofs of the dark matter existence will be presented in section 1.1.1. Moreover I will describe the main characteristics that it must have. The principal possible DM particles will be defined in section 1.1.2 and especially the favorite candidates will be treated in detail. The second part of this chapter regards instead the explanation of the main detection systems developed in the last decades especially devoted to the study of dark matter. In section 1.2, I will indeed discuss about the principal characteristics of the DM detectors and the physical phenomena that they exploit to search for the DM existence. Finally the most important DM

detectors that are running nowadays, and their principal characteristics will be briefly summarized.

In chapter 2, the properties of the rare gases will be treated. This group of elements represents in fact the active medium of the proposed detection scheme. In section 2.1, the chemical and physical aspects of the rare gases will be described, especially from the point of view of particle detectors. Properties such as the energy band gap, the electron mobility, the light yield and others will be analyzed deeply. In the second part of the chapter (section 2.2) the focus will be given instead to the rare gas crystals. Their main features, besides the principal experimental growing techniques, will be presented. The last session of the chapter (section 2.3) is instead devoted to the matrix isolation technique which is an experimental method for the growth and the study of doped rare gas crystals.

In the third chapter (3) I will present the detection schemes that have been proposed in the INFN R&D projects called AXIOMA and DEMIURGOS (section 3.1) in which I have been actively involved during my PhD. The schemes can be divided into two parts, one concerns the undoped rare gas crystals while the other the doped rare gas matrices. The possible interaction of the dark matter particles with the active material of the detector will be described and analyzed in the two proposed schemes. The features expected from the proposed detector will be shown, and properties such as the energy threshold, the interaction physics, the background rate, and the sensitivity will be discussed here. I will also compare these properties with the standards of the current dark matter detectors that are taking data nowadays.

In chapter 4 I will begin the presentation of the experimental measurements and tests conducted in these R&D projects. In particular in this chapter the aspects related to the growth of rare gas solid films and their properties, including the electrons' extraction from a neon thin crystal will be addressed. The experimental apparatus and all the techniques involved in this measurements will be described in depth in section 4.1. Measurements, results and a brief explanation will finally be discussed in sections 4.2 and 4.3.

The fifth chapter (5) is devoted to a scalability study of the proposed detection scheme. Using a suitable experimental apparatus, described in section 5.1, it was possible to grow rare gas crystals of large dimensions (kg-scale) and especially in section 5.2 a proof using xenon will be described. Furthermore, a measurement

of the light yield in solid xenon and its dependence on the temperature will be treated in this chapter.

The topic of doped RG crystals will be covered in chapter 6. I started the experimental investigation of these doped matrices from the elemental aspects because only sporadic data concerning their behavior have been found in literature. Section 6.1 will describe the experimental set-up used for the growth and the studies of rare gas matrices doped with alkali metals or rare earths. The results will be shown in section 6.2 and furthermore a possible interpretation is presented in section 6.3.

Finally the results achieved in this work will be summarized in the conclusion, where also some perspectives will be discussed.

Chapter 1

Motivations and background

In this first chapter I will briefly review the main evidences that prove the DM existence. Also the principal DM candidates which were proposed in the past decades will be discussed here with a particular attention to the candidates whose masses lie in the eV-MeV energy range. Moreover the properties of the DM halo that surrounds our galaxy will be briefly summarized in section 1.1.3. Finally, the principal detectors that are used nowadays in the searches for dark matter candidates are reviewed in section 1.2, where their working principles will be also described.

1.1 Dark Matter problem

DM is a kind of matter that does not emit light and only interacts through gravitational, and likely weak, forces. The first evidence of DM dates back to 1933 and it is due to the Swiss astrophysicist F. Zwichy [2]. Measuring the velocity dispersion of the galaxies in the Coma and Virgo clusters, he found that these galaxies move at a velocity too fast to be bound to the cluster if the only luminous matter contributes to the gravitational field. A large fraction of non visible matter, which

interacts through gravitational force, need to be present in the cluster to explain the effect, and this was the first introduction of the so called dark matter.

Furthermore, numerous other indirect proofs of the dark matter existence were discovered and studied during the last 60 years and will be presented in the next sections. Evidences at different cosmological and astrophysical scales are strongly convincing that dark matter represents a substantial amount of the Universe composition.

1.1.1 Evidences of the DM existence

Up to the present, the only experimental evidences of the existence of dark matter are indirect observations of gravitational effects in the astrophysical and cosmological fields [3]. These proofs will be briefly described in the next paragraphs.

Rotation curves of galaxies The most convincing evidence for the existence of DM on galactic scales comes from the observation of the rotation curves of the spiral galaxies. These measurements were initially performed in the '70s calculating the velocity of stars along the length of a galaxy by measuring their Doppler shifts. It was observed that the rotational velocity in the galactic plane does not decrease as expected $\propto r^{-1/2}$ outside the halo of visible matter. In fact, for a gravitational system with a symmetric mass distribution, in Newtonian dynamics, we have:

$$v(r) = \sqrt{\frac{GM(r)}{r}} \tag{1.1}$$

where G is the gravitational constant and $v(r)$ is the rotational speed at a certain distance r from the center. $M(r)$ is the mass contained inside a radius r and has the following distribution in a galaxy with a density $\rho(r)$:

$$M(r) = 4\pi \int_0^R \rho(r) r^2 \, dr \tag{1.2}$$

The experimental observation does not agree with the theoretical results of equation 1.1. For example figure 1.1 shows the rotation curve of the galaxy NGC5603 [4]. The fact that $v(r)$ is approximately constant also far away from the center, implies the existence of a non visible halo of matter contributing to the galaxy mass: the dark matter. Moreover we can notice that for the DM halo at high

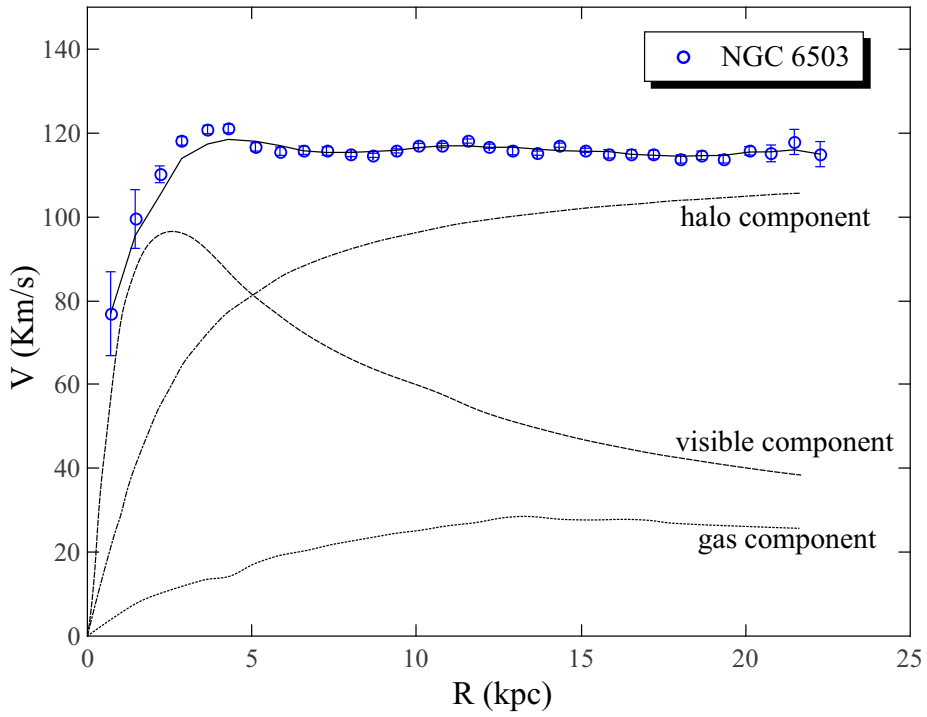

Figure 1.1: Rotation curve of the galaxy NGC 5603. The distance of this galaxy from the Earth is 5.94 Mpc, its luminosity is $4.8{\cdot}10^9\,M_\odot$ and its radius R_{25}=5.36kpc. Data and fit from [4].

distance $M_{DM}(r) \propto r$ and so $\rho_{DM}(r) \propto r^{-2}$, while at short distance $\rho_{DM}(r) \propto \rho_0$. The DM density can thus be parameterized using the following equation:

$$\rho(r) = \frac{\rho_0}{1 + (r/r_c)^2} \tag{1.3}$$

where ρ_0 is the local DM density and r_c is the core radius of the galactic center that can be obtained by experimental fit [5]. Therefore, the structure of dark matter is a spherical halo that surrounds the galactic center. Following similar consideration from the Milky Way galaxy, one can infer that the local density of DM is roughly constrained to be within $0.3 - 0.5\,\mathrm{GeV/cm^3}$ [6, 7].

Gravitational lensing The gravitational lensing is the distortion of the image of a distant object (A) due to the presence of a large amount of matter (B) along the trajectory of the light. In such a way the object B acts as a refractive lens

for an observer (O) at a certain distance. This is a well known effect of the general relativity for which a strong gravitational field modifies the space-time curvature. This phenomenon is often used in astronomy to evaluate the intensity of a gravitational field. The deflection angle of the photons can be estimated using the following equation:

$$\Delta\theta \approx \frac{2GM}{c^2 R} \tag{1.4}$$

where G and c are, as usual, the gravitational and speed of light constants, respectively, M is the mass of the object B and R is the radius of the point of closest approach of the light trajectory to the object B.

The gravitational lensing of a galaxy was firstly found in 1979 observing the image of QSO 0957+561 that appears as two images as a result of the gravitational lensing of the galaxy YGKOW G1 [8]. This effect is illustrated on figure 1.2.

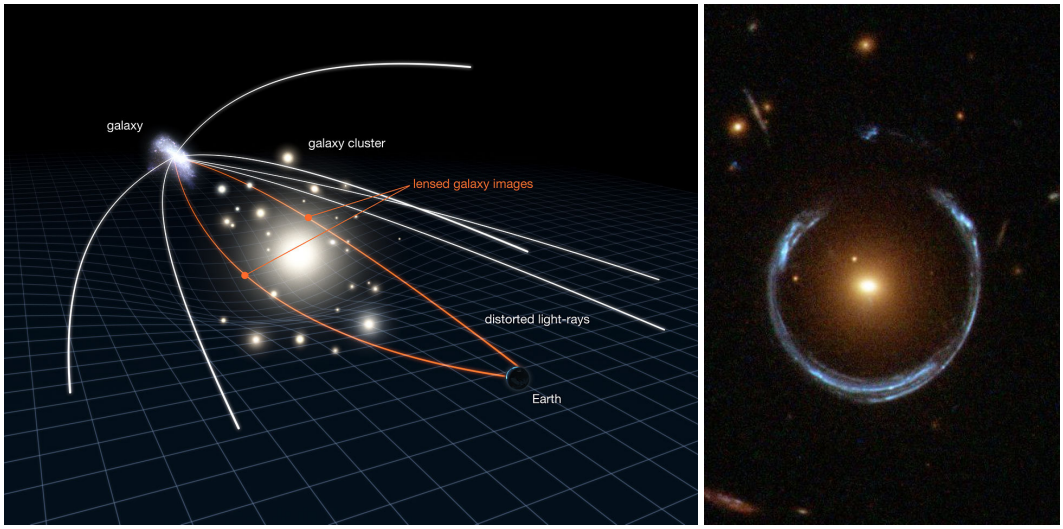

Figure 1.2: On the left side a sketch of the gravitational lensing principle where a big massive object bend the space-time curving the trajectory of the light seen from a distant observer. On the right the effect observed in LRG 3-757.

The gravitational lensing effect permits to probe the gravitational field strength and thus the amount of matter present in a galaxy that can be compared with the luminous mass. Experimental observations, for example of the galaxy cluster SDSS J0946+1006 [9] seem to confirm that these objects contain a significant quantity of dark matter, even in the central regions. Figure 1.2 shows a sketch of the

gravitational lensing principle and an experimental example in the object LRG 3-757 in the Leo constellation. The galaxy in the foreground lies in our line of sight of a more distant galaxies and the image of these last objects appears distorted shaped like a horseshoe (which is the nickname of the object). This is an example of the so called Einstein ring. It should be noted that all lensing-related methods are not applicable to low-luminosity galaxies with stellar masses $\sim 10M_{\odot}$ and below.

Galaxy clustering and Bullet cluster The term galaxy clustering refers to the 3D distribution of galaxies. In a galaxy cluster, hundreds or thousands of galaxies are bound together by gravity and joined together by a hot plasma. The typical mass of this objects ranges between 10^{14} to 10^{15} $M_{\odot}$ and, with the super-clusters, they are the largest structures known in the Universe. Due to their large mass relatively confined, these objects act as gravitational lenses and thus allow the study of the matter distribution.

Furthermore, of particular importance is the Bullet Cluster, which is a collision of two galaxy clusters. Figure 1.3 shows a composite image of this collision mixing data from the Chandra X-ray observatory and from the Hubble space telescope.

The pink halo in the figure 1.3 is the baryonic matter, which is mainly gas, detected by Chandra observatory as X-rays emission. The bullet-shaped halo on the right is the hot gas from one cluster which passed through the hot gas from the other large cluster during the collision. Since the gas interact electromagnetically, it slows down much more that the stars. The blue areas on the figure show instead where most of the mass in the clusters is located. These regions are calculated using the gravitational lensing effect to mapping the gravitational field of the clusters. Clearly, the matter in the blue clusters is separate from the baryonic matter in the pink clusters giving a direct evidence that most of the matter in the clusters is non visible.

CMB anisotropies The cosmic microwave background (CMB) is the electromagnetic radiation residual from an early stage of the Universe. This radiation was accidentally discovered in 1965 by A.A. Penzias and R. Wilson using a microwave radiometer developed for radio astronomy and satellite communications [10]. The CMB is made of photons which almost fit an ideal black body spectrum with a

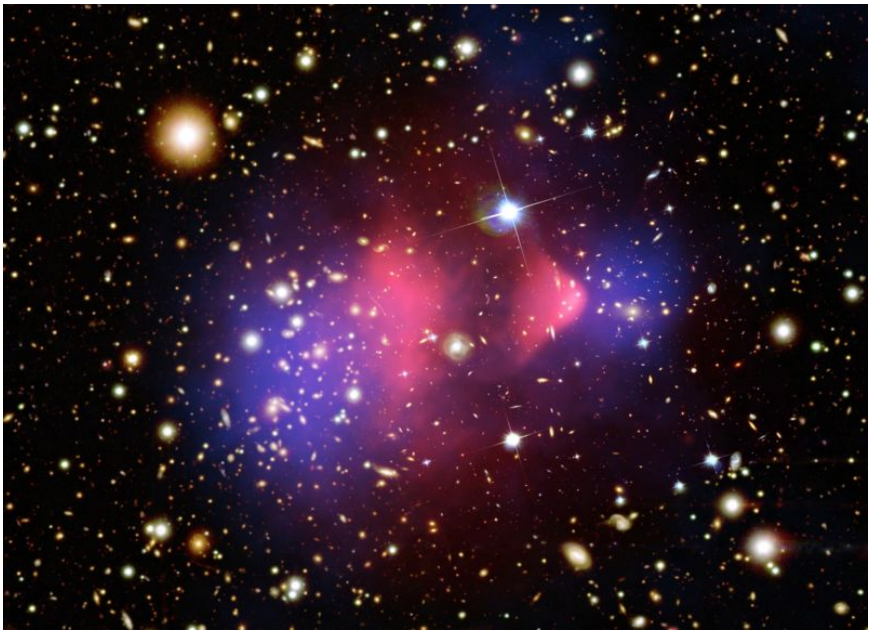

Figure 1.3: Object 1E 0657-558 also named Bullet Cluster which is the collision of two galaxy cluster. The image is a composition of data taken from Chandra telescope in the X-ray band and a visible image from the Hubble telescope.

temperature of 2.726 K. Since the CMB is a photography of the Universe when photons were well coupled and in thermal equilibrium with matter, the measurement of the anisotropies in the CMB gives crucial information about the composition of the Universe itself. The anisotropies, that represent 1 part in 10^6, can be decomposed into spherical harmonics $Y_{lm}(\theta, \phi)$ [11] following the ΛCDM theoretical model.

The figure 1.4 shows the CMB anisotropies power spectrum where the angular scale is parameterized as the multipole moment of the spherical harmonics l. The reciprocal of l corresponds to the angular scale which is called angular wavelength of the fluctuation. For example $l = 10$ corresponds to roughly 10° on the sky, while $l = 100$ corresponds to roughly 1° on the sky. The size and the position of the peaks in figure 1.4 gives information about the cosmological parameters. In cosmology it is common to express densities using the dimensionless quantity Ω defined for different species x using the following equation:

$$\Omega_x = \frac{8\pi G\rho_x}{3H^2} = \frac{\rho_x}{\rho_c} \tag{1.5}$$

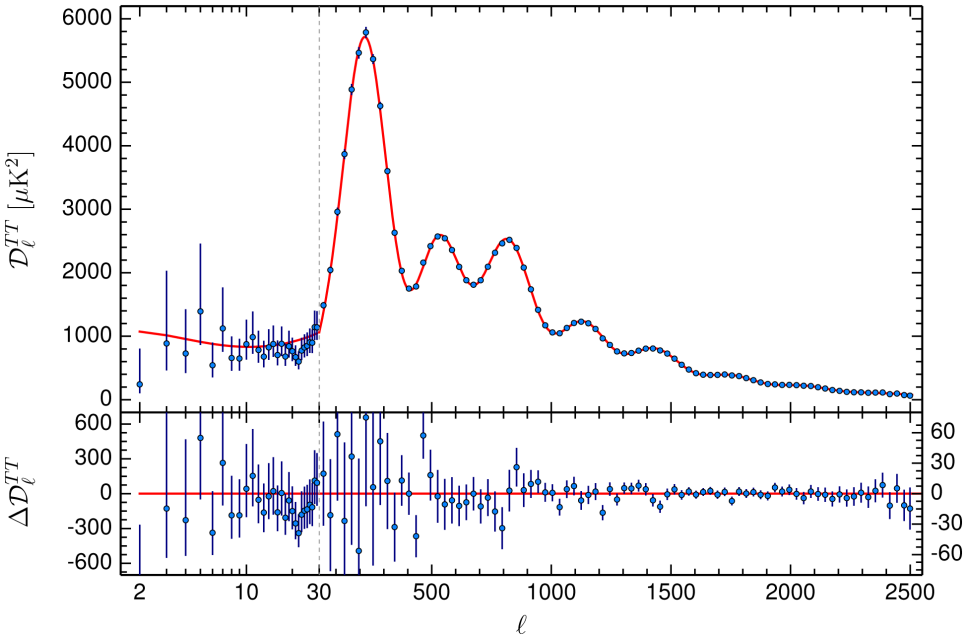

Figure 1.4: Angular power spectrum of the CMB obtained by Planck experiment in 2015. Red line in the upper panel indicates the best-fit base ΛCDM theoretical spectrum while residuals with respect to this model are shown in the lower panel. Data from ESA and Planck Collaboration [12].

where G is the gravitational constant, H is the Hubble constant, and $\rho_c = 3H^2/8\pi G$ is the critical density.

Through the CMB angular spectrum it is thus possible to infer the composition of the Universe [13] in terms of the dark energy (Λ) and the total matter (m) that can be further divided into baryonic (b) and non-baryonic or rather dark matter:

$$\begin{aligned} \Omega_\Lambda &= 0.688 \pm 0.009 \\ \Omega_m &= 0.312 \pm 0.009 \\ \Omega_b h^2 &= 0.0222 \pm 0.0002 \\ \Omega_{DM} h^2 &= 0.119 \pm 0.002 \end{aligned} \tag{1.6}$$

where the value of the parametrization constant h is 0.678 ± 0.009. The hypothesis of the existence of the dark matter is thus very strong.

Structure formation With the term structure formation we consider the period of the formation of galaxies, galaxy clusters and larger structures from small and early density fluctuations. Since from cosmological models we know that the age of the Universe is (13.799 ± 0.021) billion of years, if there were only ordinary matter in the Universe, there would not have been enough time for density perturbations to grow into the galaxies and the clusters currently seen. Simulations of clusters formation as shows in figure 1.5 requires the presence of dark matter to obtain the structures that can be observed nowadays.

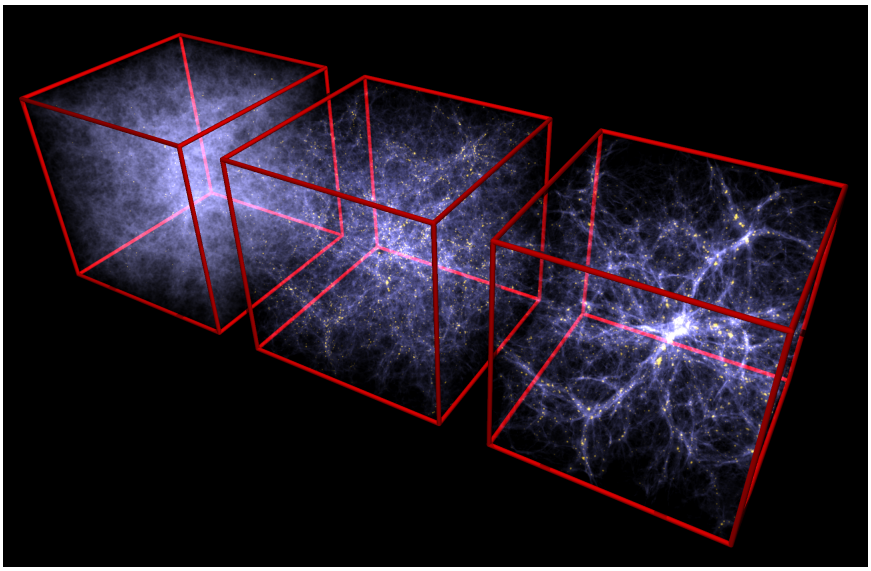

Figure 1.5: Structure formation in a simulation box. Data from Volker Springel Max Planck Institute.

1.1.2 Dark matter possible candidates

Many evidences for the existence of dark matter, all based on the gravitational interaction, have been provided in the previous section. An alternative solution of the missing-mass problem, could be the modification of the gravitational laws instead of taking into consideration the presence of new invisible matter. Following this idea, many suggestions were done in the last decades, and scientists proposed numerous, alternative theories to the gravity. Unfortunately, no one of these approaches have adequately explained the observable scenario. For instance

the Modified Newtonian Dynamics (MOND) can successfully describe the rotation curves of galaxies but it fails in the explanation of the large scale structures and of the CMB anisotropies. Moreover, the matter distribution in the bullet cluster seems to be solved only with the introduction of the dark matter. Another solution can be found introducing big massive galactic objects such as MACHOs (Massive compact halo objects). Unsuccessful searches for MACHOS in the dark halo of our galaxy ruled out this possibility and also gives an upper limit to the mass of DM candidates: $m_{max} \leq 2 \cdot 10^{-9} \mathrm{M}_{\odot} \approx 2 \cdot 10^{48}\,\mathrm{GeV/c^2}$. The limits just presented and the lack of other candidates besides primordial black holes, constitute the observational arguments we have in favor of elementary particles as DM candidates [14, 3, 15].

Neutrino Remaining within the Standard Model, neutrinos were one of the first candidates proposed to solve the DM problem due to their very weak interaction with ordinary matter. Similarly from equation 1.6, from the measurement of the CMB temperature [16], the relic density of the neutrinos is given by:

$$\Omega_{\nu} = \frac{\sum m_i}{h^2 \cdot 93.14\,eV} \tag{1.7}$$

where m_i are the masses of the three different families of neutrinos. Considering also the constrain to the mass ($\sum m_{\nu} < 0.15\,\mathrm{eV}$) [17], one can estimate an upper limit also to the density $\Omega_{\nu} h^2 < 0.0013$ which is not enough to consider DM composed of neutrinos. Furthermore, the neutrinos' relativistic speed in the early Universe would not have induced such a large scale structure as observed today.

Axion The axion is a particle introduced by R. Peccei and H. Quinn in the '70s to solve the strong charge-conjugation-parity (CP) problem of the SM, i.e. the absence of CP symmetry violation in the strong interaction [18]. They introduced a new global symmetry $U(1)_{PQ}$ which is spontaneously broken at a certain energy scale f_a and compensate the CP-invariant term of the QCD Lagrangian. In particular, the axion is a Nambu-Goldstone boson [19] which corresponds to the phase of the Peccei-Quinn complex field and its mass m_a can be expressed in terms of the neutral pion properties as follows:

$$m_a \approx \frac{f_{\pi} m_{\pi}}{f_a} \frac{\sqrt{z}}{1+z} \tag{1.8}$$

where m_π and f_π are respectively the mass and the decay constant of the pion π^0 and z is the ratio between the mass of the quark up and the quark down. Taking into account the values of the parameters of equation 1.8, a direct relation between the axion mass and the symmetry breaking scale [20] is given by:

$$m_a \approx 5.70\,\mu\text{eV}\left(\frac{10^{12}\,\text{GeV}}{f_a}\right) \tag{1.9}$$

Astrophysical constraints bound f_a between $10^8\,\text{GeV}$ and $10^{17}\,\text{GeV}$ and thus the mass is expected to be very light (under the eV) [21]. Axions are expected to be uniformly distributed with a density of around $10^{14}\,\text{cm}^{-3}$ and both the mean velocity and the velocity distribution width are about $10^{-3}c$. Also a small spread in the velocity of 1 part over 10^6 is expected [22]. A well-established theoretical result in the two most accredited "invisible axion" models, the Kim-Shifman-Vainstein-Zacharov (KSVZ) model [23] and the Dine-Fischler-Srednicki-Zhitnitsky (DFSZ) model [24] is that dark matter axions can interact both with fermions and with photons [22].

Axions and also axion-like-particles (ALPs) are one of the favored lightest candidates for the solution of the dark matter problem. The present experimental limits on the axion coupling to the ordinary matter obtained in different experiments are shown in figure 1.6.

Supersymmetry In the theory of supersymmetry (SUSY), each particle in the SM has a partner particle. Theoreticians proposed the supersimmetry to address numerous phenomenological problems of the SM, as for instance the hierarchy or the Higgs mass fine tuning. SUSY particles could furthermore provide candidates for dark matter, especially s-neutrinos and gravitinos have been investigated in the past [25, 26]. In the theory, these particles are respectively the partners of neutrinos and gravitons. Another excellent dark matter candidate is also the lightest supersymmetric fermion particle, the neutralino, which is predicted to be stable and it can only be destroyed through pair annihilation [27]. Theory foresees that SUSY particles can be generated in the collisions of the high energy accelerators such as LHC, but unfortunately no evidence for SUSY particles has been found yet.

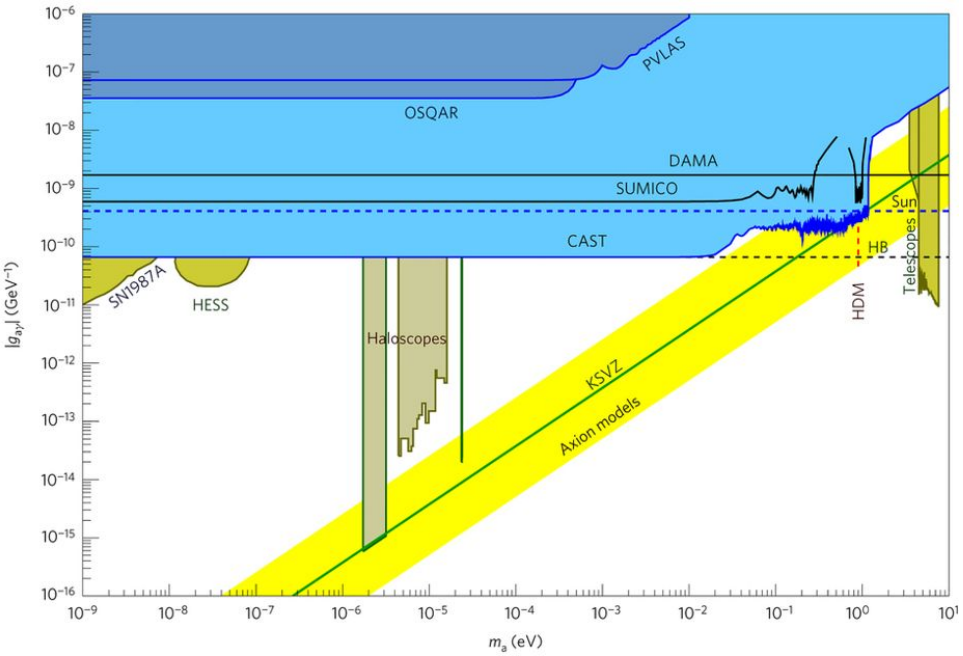

Figure 1.6: Experimental limits on the coupling constant between axion and photon as a function of the axion mass.

Weakly Interacting Massive Particles The generic class of particles known as Weakly Interacting Massive Particles (WIMPs) are one of the favored candidates for the DM problem solution in a scenario of physics beyond the Standard Model [28]. These non-baryonic particles do not have charge and color, and can only interact through the gravitational and the weak force. The dark matter WIMPs are assumed to be Majorana particles i.e. they are equal to their antiparticle and stable or with an extremely long lifetime (lower bound ≈160 Gyr) [29]. Furthermore, WIMPs satisfy the so called "WIMP miracle": at a certain point during the Universe expansion, the annihilation rate of the particles has become negligible and thus the abundance of the particles has been fixed (freeze-out). The resulting current relic abundance can be expressed as a function of the annihilation rate as:

$$\Omega_X h^2 = \frac{m_X n_X}{\rho_c} = 3 \cdot 10^{-27} \frac{\mathrm{cm}^3 \mathrm{s}^{-1}}{\langle \sigma_a v \rangle} \tag{1.10}$$

where the label X is the dark matter particle and m_X and n_X are its mass and its density at thermal equilibrium, respectively. $\langle \sigma_a v \rangle$ is the average total annihilation

cross section multiplied by the particle velocity. Since the dark matter abundance in the Universe is known, equations 1.10 and 1.6 can be compared. It is thus possible to infer that the cross section and the mass of the particle X lie in the electro-weak scale and GeV/c^2−TeV/c^2 range, respectively. Those are exactly the conditions expected for the WIMPs particles and this is the "WIMP miracle".

Figure 1.7 shows exclusion limits for WIMPs mass between 1 and 10^4 GeV/c^2 for different experiments that are now taking data. In particular, the best lower limit for the WIMP-nucleon cross section is currently given by $\sigma_{\mathrm{WIMP-Xe}} = 4.1 \cdot 10^{-47}\,\mathrm{cm}^2$ at $m_{\mathrm{WIMP}} = 30\,\mathrm{GeV/c^2}$, obtained by the XENON1T collaboration [30].

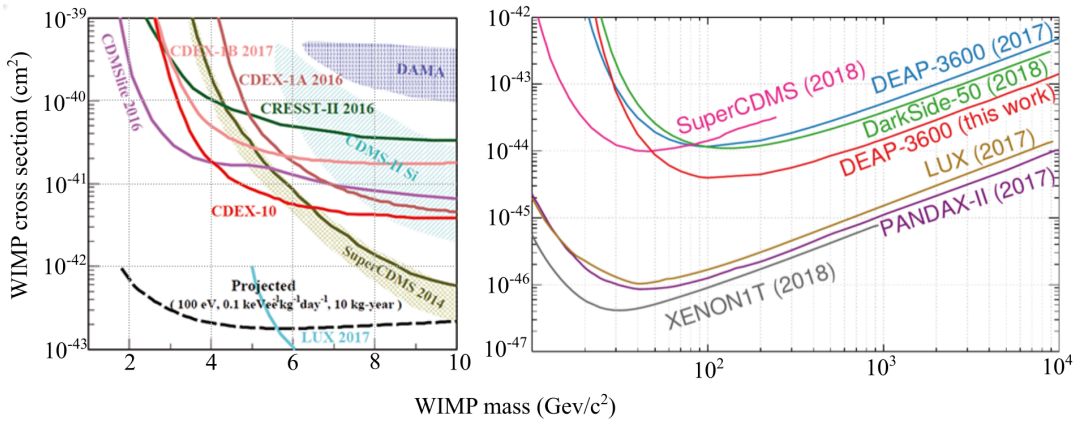

Figure 1.7: Spin independent WIMP-nucleon cross section for WIMP masses in the range $1 - 10\,\mathrm{GeV/c^2}$ (left) and $10 - 10^4\,\mathrm{GeV/c^2}$ (right). Different curves show the limit obtained by different experiments. Data from the publications of the experiments' collaborations.

1.1.3 Features of the dark halo

In general, starting from simulations of the behavior of single galaxies, the scientific community agrees to define standard properties for the dark matter halo that surrounds each galaxy. It is assumed that the dark halo is spherical, isotropic, pseudo-isothermal and made of cold and non- or weakly-interacting particles [31].

A more precise density function with respect to the equation 1.3 is the Navarro-

Frenk-White density profile:

$$\rho(r) = \frac{\rho_0}{\frac{r}{R_s}\left(1+\frac{r}{R_s}\right)^2} \tag{1.11}$$

where r is the radial coordinate while ρ_0 is the Universe density at the formation of the halo and R_s is the characteristic radius of the halo itself. ρ_0 and R_s are two parameters specific of any halo. For the Milky Way galaxy, the local dark matter density is expected to be constrained between :$\rho \sim 0.3 - 0.5\,\mathrm{GeV/cm^3}$ [32, 6].

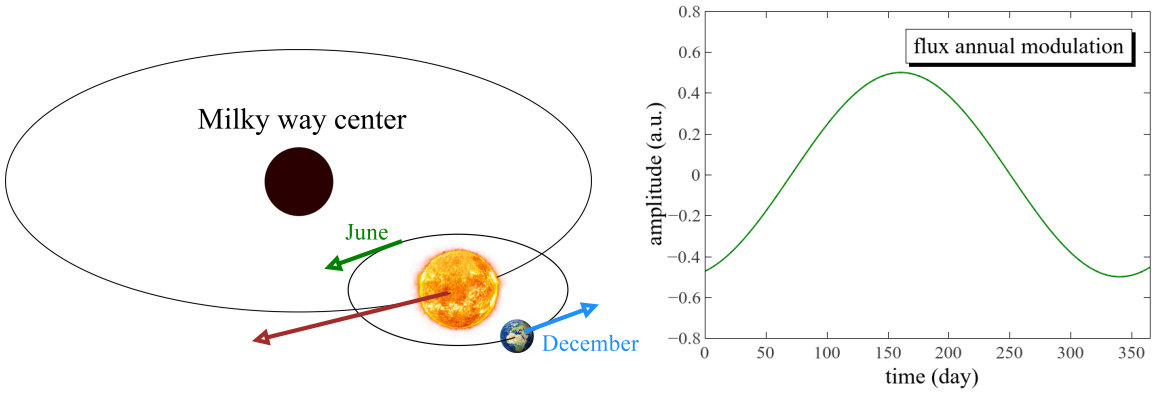

Figure 1.8: On the left a schematic picture of the Milky Way with the Sun and the Earth motions. Red arrow is the Sun velocity while blue and green arrows are the orbit velocity of the Earth in December and June, respectively. On the right, a simulated plot of the annual modulation of the DM particle flux.

Another important property that can be inferred from the simulation is the velocity of the particles that compose dark matter in the halo. A widely used function for the velocity distribution of the particles in the halo is the Maxwell-Boltzmann distribution given by the following equation [31]:

$$f(v) = \frac{4}{\sqrt{\pi}}\beta^{3/2}v^2e^{-\beta v^2} \tag{1.12}$$

where $\beta = 3/(2v_{rms}^2)$ is the root mean square velocity dispersion. The equation 1.12 can be used to calculate the halo velocity with respect to the Earth frame of reference moving with a velocity $v_\oplus$:

$$
\begin{aligned}
f(v) &= 2\left(\frac{\beta}{\pi}\right)^{1/2} \frac{v_a}{v_e} e^{-\beta(v_a^2+v_e^2)} \sinh\left(2\beta v_e v_a\right) \\
&\approx 2\left(\frac{\beta}{\pi}\right)^{1/2} \frac{v_a}{v_e} e^{-\beta(v_a-v_e)^2}
\end{aligned}
\tag{1.13}
$$

Where v_e is the earth velocity while v_a is the halo velocity. With these assumptions, the velocity has a maximum at $\sim$ 350 km/s and a spread of about 300 km/s. Furthermore, the DM particles flux on Earth can be calculated as:

$$\Phi = \frac{\rho}{m_X} \times \langle v \rangle \tag{1.14}$$

where m_X is the mass of the dark matter particles and v the relative velocity between DM particles and the target in the Earth. Moreover considering that the Earth is rotating around the Sun, we have that in June the orbital velocity has the same sign of the Sun velocity while in December the two velocities are opposite [33]:

$$v_\oplus = v_\odot + v_{orb} cos(\pi/3) cos[\omega(t - t_0)] \tag{1.15}$$

where the Sun tangential velocity is $v_\odot \approx$232 km/s and the Earth orbital velocity is $v_{orb} \approx$30 km/s. Consequently, it results that the flux of DM particles on Earth is modulated with a sinusoidal function with a period of $2\pi/\omega$ in one year. In particular, the maximum ($t = t_0$) is the 2^{nd} of June [34]. Figure 1.8 shows a schematic representation of the Earth motion in the Milky Way galaxy and the annual modulation of the DM particle flux.

1.2 Dark matter detectors: state-of-the-art

Besides some ad hoc schemes, such as direct conversion of DM particles into visible ones, the standard detection techniques can be summarize in three large categories depending on the signal they exploit [35]:

- scintillation signal;
- ionization signal;
- phonons signal.

Figure 1.9 shows a visual representation of these detectors categories and the corresponding dark matter experiments. Projects name connected by two arrows indicate experiments characterized by a composition of two different kind of signals. These three categories of detectors will be discussed in more detail and a brief review concerning the main dark matter experiments, will be presented in the next paragraphs

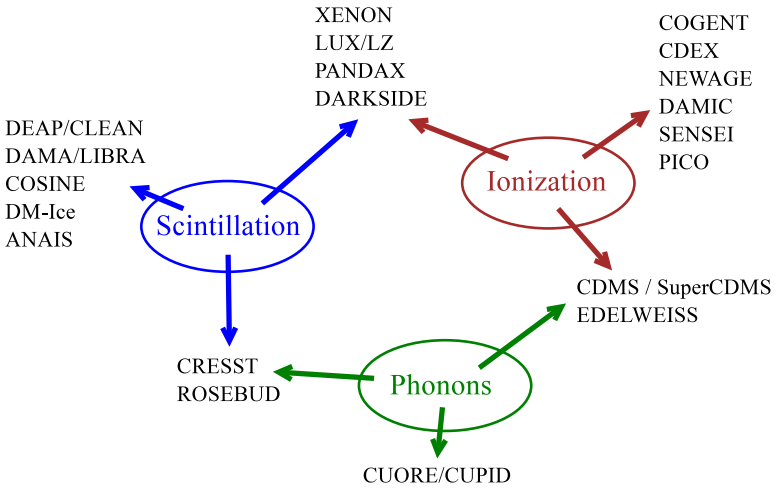

Figure 1.9: Visual representation of the standard signals used in DM searches. Acronyms of different experiments are also shown, correspondingly to the signal they use.

Scintillation signal In scintillators, the energy released by the incident particle is converted into photons in the detector medium. The effect of the particle is indeed to excite the electrons (e^-) in the medium and the light output is a consequence of their relaxation. In a typical scintillating material the valence and conduction bands are separated by few eV so that the wavelength of the emitted photon is in the ultraviolet (UV) or visible (VIS) regions. To avoid the self reabsorption of the light emitted by the scintillator, the absorption band needs to be separated with respect to the emission band. Often, this characteristic is obtained introducing atoms of different species (dopants) inside the material, such as rare earth atoms, that introduce energy levels in the band gap.

A convenient parameter used to describe the quality of the scintillator is the light yield (LY) which gives the number of photons produced as a function of the

incident energy expressed in MeV. Another important parameter of the scintillators is the time resolution which is basically given by the fluorescence lifetime (τ_{scint}) and so it is related to the strength of the transition between the electronic states. Forbidden transitions, such as between 4f-4f states in trivalent rare earths, can have a long lifetime up to milliseconds [36]. Some interesting properties of the inorganic and organic scintillating materials are listed in table 1.1.

The light coming from the scintillating crystals is then collected using appropriate photon detectors such as photomultiplier tubes (PMTs), Silicon photomultipliers (SiPMs), or semiconductor photodiodes, which are characterized by a high collection efficiency and a high gain.

Crystal	$\rho\,(\mathrm{g/cm^3})$	LY (ph/MeV)	$\tau\,(\mathrm{ns})$	$\lambda_{max}\,(\mathrm{nm})$
NaI(Ti)	3.67	$4 \cdot 10^4$	240	410
BGO	7.13	$4 \cdot 10^3$	300	480
CSI(Ti)	4.51	$2 \cdot 10^4$	1000	565
antracene	1.25	$4 \cdot 10^4$	30	448
p-terphenil	1.23	$1.2 \cdot 10^4$	6-12	391

Table 1.1: Density, light yield, fluorescence lifetime and maximum emission wavelength for some inorganic and organic scintillators.

Considering a standard scintillating crystal with a light yield of $\sim$40 ph/keV and taking into account both the efficiency of the light collection (solid angle and quantum efficiency of PMT) and the limiting physical parameters, such as the quenching and the Fano factors, the energy threshold for a detector that exploits scintillation signal can difficultly be lower than a few keV.

Numerous detectors designed for dark matter searches exploit scintillation signal. The main experiments that are taking data nowadays are the following:

- The DEAP/CLEAN family of detectors exploits liquid argon or neon as scintillating media. These experiments operate in the underground laboratory of SNOLAB in Canada since 2009 [37].

- The DAMA/LIBRA (Large sodium Iodide Bulk for RAre processes) is a large detector based on a matrix of NaI(Tl) scintillators which operates in the Gran Sasso Laboratory of INFN in Italy. Since it has begun operation in the 1995

(initially it was DAMA/NaI) this detector collected many annual cycles signals. This experiment has confirmed the presence of a model-independent annual modulation effect in the data in the $2-6\,\mathrm{keV}$ range that satisfy all the features expected for a dark matter signal with high statistical significance [38, 39]. However in 2019 the COSINE-100 collaboration, using an array of the same NaI(Tl) scintillating crystals of DAMA/LIBRA, rules out WIMP–nucleon interactions as the cause of the annual modulation observed by the DAMA experiment [40].

- DM-ice [41] and ANAIS [42] are two additional experiments that exploit NaI(Tl) as scintillating medium. They are placed in the South Pole and in the Canfranc Underground Laboratory in the Spanish Pyrenees, respectively.

Ionization signal The ionization process occurs when a couple electron-ion is created in the detector medium following the energy release of the incident particle. Electrons, that are not more bounded, can then be measured in different ways. First examples of ionization detectors were the cloud chambers and the bubble chambers developed in the early years of the 1900. Nowadays, the more promising detectors that exploit ionization signals are the semiconductor devices such as silicon or germanium detectors and the gas ionization chambers.

An important parameter is the W-value, which is the energy (E_{in}) necessary to create an electron-hole pair (N_{charge}) in the material:

$$N_{charge} = \frac{E_{in}}{W} \tag{1.16}$$

When electrons and holes are generated within the medium, they can drift under an electric field, which is opportunely applied between two electrodes: the anode and the cathode. Here, the Shockley-Ramo theorem allows to calculate the induced electric current. Since semiconductors have a lower W-value with respect to the gas, these detectors have a better energy resolution and furthermore, as the electrons mobility is high, also the time resolution is satisfactory in semiconductor devices. Finally it is worth noting that, since W depends on the energy band gap, it depends on the temperature and thus the detector response changes as a function of the temperature.

One of the best performance in terms of energy threshold for this kind of

detectors is about 220 eV which was obtained in high purity germanium crystals kept at cryogenic temperature [43].

In the following list, the major detectors that exploit ionization signals are reported:

- The CoGeNT project uses a single crystal of Germanium of ∼100 g as a cryogenic detector for WIMPs [44]. This experiment has operated in the Soudan Underground Laboratory since 2009.
- The CDEX experiment exploit p-type point contact germanium detectors (pPCGe) sensitive to sub-keV recoil energy. This experiment is located at the China Jinping Underground Laboratory and started taking data since 2014 [45].
- The NEWAGE experiment consists in a time projection chamber filled with 0.1 bar of CF_4 gas placed at Kamioka in Japan.
- DAMIC is a gram-scale detector installed at SNOLAB in Canada that uses very thick CCDs of almost 1 mm bulk silicon detector [46]. A future kg-scale volume with the same technology is planned to be installed at the Modane laboratory.
- Also SENSEI [47] experiment at FERMILAB takes advantage of the CCD technology to detect sub-Gev dark matter particles.
- Finally, another kind of detector that exploits the ionization is PICO-60 which is a bubble chamber filled with CF_3F_8 which is taking data in the SNOLAB area since 2013 [48]. A larger chamber with an active volume of 500 litres is expected to start this year in the same laboratory.

Phonon signal Bolometers are a class of detectors that exploit phonons signal. Phonons are quasi-particles that represent excited states of the modes of vibration of elastic structures such as lattice bonding. In the bolometers the energy of the detectable particle is released in the absorber medium causing an increase of temperature that can be expressed as:

$$\Delta T = \frac{E_{in}}{C} \tag{1.17}$$

where E_{in} is the incident energy and C is the heat capacity of the absorber. The temperature change can be directly measured through a temperature sensor precisely coupled to the absorber. From equation 1.17 it is clear that the limiting factor is related to the heat capacity C of the system. In fact, in order to have a measurable signal, C must be low and thus, since C is proportional to the mass of the absorber, the bolometers must be of small dimensions. Using this kind of sensors, a very low energy threshold can be obtained in small systems, and a value of $E_{th} \sim 20\,\text{eV}$ was recently reached in an extra pure Al_2O_3 crystal of $\sim$0.5 g mass by a German-Austrian-Portuguese collaboration [49].

The technology involved in the bolometer detectors concerns both the ultra-cryogenics and the high efficiency temperature sensors. These fields have been developed at a level necessary for the application in large scale particle detectors only during the last few decades and for this reason bolometers have become crucial in the detector scenario only in the last few years. Important bolometric experiments are the following:

- The family of detectors CUORE [50] and CUPID [51] consists of a large array (towers) of tellurium oxide (TeO_2) for CUORE and zinc selenide (ZnSe) crystals for CUPID, kept at few milliKelvin. The temperature sensors are constituted by neutron-transmutation-doped-germanium-thermistors kept in contact with everyone of the 988 crystals [52]. Even if the scientific goal of CUORE and CUPID is to explore the inverted hierarchy of neutrino masses, this experiment can also give some limits in the dark matter research field.

- It is worth noting also that many CMB measurements were done using polarization-sensitive arrays of transition-edge-sensor (TES) bolometers [53].

Hybrid signals There are many detectors that exploit a composition of different types of signals. There are in fact hybrid detectors that take advantages of scintillation and ionization, others that exploit ionization and phonons and finally experiments that use scintillation and phonons. Even if these multiple approaches require a more complex design, they can exploit many advantages which are very promising in the search for dark matter candidates.

As concerns the experiments that exploit both scintillation and ionization signals it is important to recall the time projection chambers (TPC). During the

last years the major experiments of this type that have been running successfully were LUX [54, 55], XENON [56, 57, 58], PANDAX [59, 60] and DarkSide [61], and upgrades of these detectors are currently underway [62, 63, 64]. Dual phase xenon TPC detectors are currently leading in the search for dark matter WIMPs with mass ranging between few GeV/c^2 to several TeV/c^2. These detectors are a modification of the single phase TPC that were invented in the late '70s by D.R. Nygren. In dual phase noble liquid TPC detectors, the incoming WIMP particle induces a nuclear recoil (NR) event when the hit occurs. NR events have two signatures: a prompt S1 light signal due to the scintillation of noble liquid, and a delayed S2 light signal related to the ionization electrons in the gas phase. Typically S1 and S2 signals are collected by two arrays of phtomultiplier tubes (PMTs) which are placed respectively in the top and in the bottom plane of the detector. The vertex of interaction between the WIMP and the target nucleus of the detector can be reconstructed using the photon pattern on the PMT arrays and also using the time difference between the S1 and the S2 signals. Most of the background events in these detectors are due to the electron recoil (ER) which have a different proportion and shape in the S1 and S2 signals compared to the NR events and so a large number can be identified and removed through offline analysis algorithms.

Another group of hybrid detectors is the scintillating bolometers. These devices are designed to simultaneously measure the heat and the light produced by the interaction of a particle in the medium. The ROSEBUD (Rare Objects SEarch) experiment started its activity in the Canfranc Underground Laboratory during 1998 and complete its activity in 2014. This experiment used many different kind of scintillators such as BGO, LIF, sapphire, Al_2O_3, cooled down to $\sim$20 mK and mounted in a double bolometer configuration. In fact, also scintillating photons produced in the absorber and escaping from it are re-absorbed in a thin layer of germanium that acts as a second bolometer [65]. Another experiment is CRESST (Cryogenic Rare Event Search using Superconducting Thermometers) which consists of ultra-pure, scintillating calcium tungstate crystals ($CaWO_4$) whose operating temperature is $\sim$15 mK. Temperature sensors are made of superconducting-transition-edge sensors (TES) read by Superconducting Quantum Interference Devices (SQUID). Also in this experiment, the light is measured by a second bolometer based on a silicon on sapphire absorber and a TES sensor glued to the crystals. The total mass of the detector is about 250 grams [66]. Finally, another project in this class is the

LUMINEU experiment, which is a very large scale scintillating bolometer designed to prepare the construction of a next-generation neutrinoless double beta decay experiment [67].

The last category of hybrid detectors exploits ionization and phonon signals. The majour experiments of this class are: CDMS (Cryogenic Dark Matter Search), its upgrade SuperCDMS and EDELWEISS (Expérience pour DEtecter Les WIMPs En Site Souterrai). CDMS and SuperCDMS are a family of experiments located in North-America at Stanford, Soudan and SNOLAB, that uses an array of semiconductor detectors kept at milliKelvin temperatures [68, 69]. Phonon detection is accomplished with TES read by SQUID amplifiers, while ionization signals are read using FET amplifiers. An important aspect of these detectors is the capability to provide phonon pulse-shape signals which is crucial to reject near-surface background data. EDELWEISS is instead a collaboration based on Modane Underground Laboratory in France. The last science run of this experiment used 40 high purity germanium cryogenic bolometers cooled to 20 mK.

Other detectors for dark matter axions Besides all the experiments previously described, which are basically focused on the searches of WIMPs, there is a large group of DM detectors devoted to the search of axions [70]. Many of the axion detectors exploit the axion interaction with photons and thus the detection problem is related to the high efficiency detection of photons with a high level of background suppression.

ADMX (Axion Dark Matter eXperiment) is currently the leading experiment in axion searches and it uses a microwave resonant cavity within a large superconducting magnet. The principle of operation is the conversion of the dark matter axions into microwave photons in the presence of a strong magnetic field (about 8 T magnet). The microwave resonant cavity with a high-Q value, i.e. low energy loss, is cooled down to liquid helium temperature to suppress the thermal noise which is the dominant background. To further lower the noise it is foreseen to reduce the temperature down to 100 mK or less using dilution refrigerators. The cavity is tunable by adjusting the positions of two tuning rods within the resonator. This allows the scanning of the cavity resonant frequency in the region of interest. Finally, a high sensitive microwave receiver arranged by an exotic SQUID amplifier allows axion searches in the $2 - 4\,\mu$eV [71, 72].

HAYSTAC (Haloscope at Yale Sensitive To Axion CDM) is another experiment that exploits axion photon conversion into microwave cavity. In particular HAYSTAC is a high-frequency offshoot of the earlier ADMX experiment that is searching for axions in the mass range $19 - 24\,\mu$eV [73].

QUAX is a ferromagnetic haloscope and it exploits the axion to photons conversion within the ferromagnetic media YIG (Yttrium Iron Garnet) in microwave resonant cavity. The axion interacts with the electrons in the material and acts as a source of spin flip. The cavity frequency is strongly coupled with the Larmor frequency of the YIG and this gives rise to a hybrid system of coupled oscillators. The high Q-value cavity is kept at $\sim$50 mK to suppress the thermal noise. The axion interaction with the spin of the YIG leads in the production of microwave photons in the GHz range, i.e. an excess of power in the cavity. Photons can then be measured using appropriate photon counters in that region. This experiment is an italian collaboration based at the Legnaro National Laboratory of INFN and is currently looking for the axion in the mass range around 70 μeV [74].

CAST is the acronym of CERN Axion solar telescope. It looks for the axion produced in the Sun's core when X-rays scatter off electrons and protons in the presence of strong electric fields [75]. This experiment is located at the CERN in Switzerland and is a worldwide collaboration. The detection idea is that the magnetic field acts as a catalyst to transform axions into X-rays, making them relatively easy to detect using appropriate detectors. As the conversion efficiency for axions increases as the square of the product of the transverse magnetic field component and its length, CAST uses a high strength superconducting dipole magnet with a long length, ensuring thus the efficiency of the process. The best limit on axion-photon coupling strength given by this experiment is of $0.66{\cdot}10^{-10}\,\mathrm{GeV}^{-1}$ in the axion mass range between $10^{-4} - 10^{-2}$ eV. A much larger, new-generation, solar axion detector (helioscope), the International Axion Observatory (IAXO), has been proposed and is now in preparation [76].

CASPEr (Cosmic Axion Spin Precession Experiment) is another experiment devoted for the search of QCD axions and ALPs exploiting their couplings with baryonic matter that enable their detection via nuclear magnetic resonance (NMR). This experiment exploits thus the precession of nuclear spins in a material sample in the presence of an electric field. Precision magnetometry can then be used to search for such precession in the range $0.01 - 0.8\,\mu$eV [77].

MADMAX (Magnetized Disc and Mirror Axion Experiment) is a German-French-Spanish collaboration that would take advantage of the static magnetic field necessary to convert the axion into microwave radiation at the transition between two non-conducting materials with different refractive indices. The MADMAX project is designed to be sensitive for axions with masses in the range $40-400\,\mu$eV. A final design of the experiment is planned after the R&D phase and it will use 80 dielectric disks of a few mm thickness aligned in a large microwave cavity [78].

Many other experiments that carry out axion searches both exploiting the axion-photons interaction, and the axion-fermions coupling have been proposed and are in their R&D phase.

1.3 Dark matter production at accelerators

Among the direct searches through the experiment above described, dark matter direct production in colliders offers another possible way to search for DM candidates. Since in most scenarios dark matter coupling and mass ranges are close to the electro-weak symmetry breaking scale, dark matter particles can be produced in accelerators if the center-of-mass energy is high enough. Colliders experiments such as CMS or ATLAS at the Large Hadron Collider at CERN analyze their data looking for missing energy in the reconstructed events of the hadronic collisions. These experiments interpret constraints on production cross sections in terms of effective field theories and simplified models [79, 80, 81, 82, 83]. The direct production at accelerator is of particular importance in the case of spin-dependent cross section, where the direct searches constraints are less stringent. This can give a comparison between direct searches and indirect experiments that can be of great help in understanding the DM nature.

Chapter 2

The rare gases

The family of rare gases (RG) also known as noble or inert gases are the six elements of the VIII group of the periodic table. They are: helium (He), neon (Ne), argon (Ar), kripton (Kr), xenon (Xe) and radon (Rn). Moreover oganesson (Og), which was firstly synthesized in 2002, is predicted to be a rare gas but its chemistry has not yet been investigated.

Rare gases have been used in the last four decades as an active media for particle detectors. They have in fact a very exclusive combination of properties (for instance the high stopping power, the small Fano factor and the relatively low energy required for electron-ion or photon production) that make them interesting in the field of radiation and particle detections. Furthermore, rare gases have crucial benefits not only in scientific and research areas but also in industrial, medical and everyday life applications, e.g. neon is important in corneas' surgery, krypton is used as a filler gas between insulated glass windows and xenon has applications in plasma screens, car headlights and anesthetics.

In this chapter I will briefly summarize the principal chemical and physical properties of rare gases, looking especially at the parameters related to the particle detection field. The fundamental methods for the growth of rare gases crystals and the main features concerning the crystal characterization will also be discussed.

Finally, last section is dedicated to the matrix isolation technique, a method used for the growth of doped crystals of inert gases.

2.1 Principal properties

Nevertheless their name, several of RG elements are quite abundant on Earth and in the rest of the Universe, so the designation rare is misleading. In fact, collectively, rare gases make up about one percent of Earth's atmosphere and helium is the most abundant element in the Universe except hydrogen. Commercially, they are obtained from the air by first cooling it until it liquefies, then selectively distilling the components at their various boiling temperatures. The naturally isotopic abundances of the rare gases are shown in table 2.1.

The atoms of this group have a stable electronic configuration in the form $1s^2$ or ns^2np^6. This implies that their outer shell of valence electrons is considered to be "full" making them highly unreactive except under particular extreme conditions.

The principal chemical and physical properties, especially regarding the field of particle detection, will be presented in this section.

2.1.1 Chemical properties

Due to their similar electronic configuration, RG are characterized by some common features. The principal chemical properties of rare gases are shown in the table 2.2.

The temperatures of boiling and melting at 1 bar pressure of every RG, as shown in the table, are very close (less than 5 K). This feature is strictly related to the weak inter-molecular forces that characterize the liquid and the solid phases, as will be discussed in the section 2.2. Furthermore, since these dispersion forces depend on the size of the atoms, and in particular they increase with the radius, it is clear why neon has the lower boiling point after helium. It is worth noting that helium does not have a solid phase at atmospheric pressure. Due to the quantum effect of the "zero point energy", the root-mean-square displacement of He atoms at absolute zero is about 30% of the crystal lattice spacing, and He can be solid only at a pressure higher that ≈25 bar. The density of the RG at different phases is also shown in the table 2.2. A high density of the active medium of the detector

RG	Atomic mass	Natural abundance(%)
$_2He^3$	3.01603	$1.3 \cdot 10^{-4}$
$_2He^4$	4.00260	100
$_10Ne^{20}$	19.99244	90.92
$_10Ne^{21}$	20.99244	0.257
$_10Ne^{22}$	21.99138	8.82
$_18Ar^{36}$	35.96755	0.337
$_18Ar^{38}$	37.96272	0.063
$_18Ar^{40}$	39.96238	99.60
$_36Kr^{78}$	77.9204	0.35
$_36Kr^{80}$	79.9164	2.27
$_36Kr^{82}$	81.9135	11.56
$_36Kr^{83}$	82.9114	11.55
$_36Kr^{84}$	83.9115	56.90
$_36Kr^{86}$	83.9106	17.37
$_54Xe^{124}$	123.9061	0.096
$_54Xe^{126}$	125.9042	0.090
$_54Xe^{128}$	127.9035	1.92
$_54Xe^{129}$	128.9048	26.44
$_54Xe^{130}$	129.9035	4.08
$_54Xe^{131}$	130.9051	21.18
$_54Xe^{132}$	131.9042	26.89
$_54Xe^{134}$	133.9054	10.44
$_54Xe^{136}$	135.9072	8.87

Table 2.1: Atomic mass and relative abundance of the RG. Data from references [84]

is in fact of help if one wants to detect events characterized by a small cross section of interaction.

Another interesting characteristic of the RG that is important in the proposed detection scheme, is the vapor pressure. In particular it is important to know the trend of this parameter as a function of the temperature. Experimental data and

Chemical property	He	Ne	Ar	Kr	Xe
Atomic weight mean A	4.002	20.180	39.948	83.798	131.29
Melting temperature T_m (K)	–	24.56	83.81	115.78	161.40
Boiling temperature T_b (K)	4.22	27.10	87.30	119.93	165.05
gas density @ 298K ρ(g/l)	0.18	0.9 0	1.78	3.75	5.89
gas density @ T_b ρ(g/l)	16.6	9.56	5.77	8.89	9.99
liquid density @ T_b ρ(g/cm^3)	0.12	1,21	1.39	2.42	2.94
liquid density @ T_m ρ(g/cm^3)	–	1.25	1.41	2.45	3.08
solid density @ T_m ρ(g/cm^3)	–	1.44	1.62	2.83	3.54
Triple point temperature T_t (K)	–	24.56	83.81	115.77	161.41

Table 2.2: Principal properties of rare gases. T_m and T_b are at 1 bar. Data from references [85].

theoretical calculations for the vapor pressure of rare gases at cryogenic temperatures are shown in figure 2.1. The fit is given by the following function:

$$log_{10}P = A + B/T + CT \tag{2.1}$$

where P is expressed in mbar and T in Kelvin. The values of the parameters A, B, C for every rare gas are listed in table 2.3 [86].

Fit parameter	Ne	Ar	Kr	Xe
A	6.89224	7.66391	7.73270	7.78642
B	-110.809	-414.861	-578.32	-806.689
C	0.005434	0	0	0

Table 2.3: Fit parameters for the equation 2.1.

2.1.2 Physical properties

As described in section 1.2, rare gases can also be used as particle detectors. Their behavior as detectors can be described using few parameters that are commonly accepted. In the next few paragraphs these parameters will be discussed.

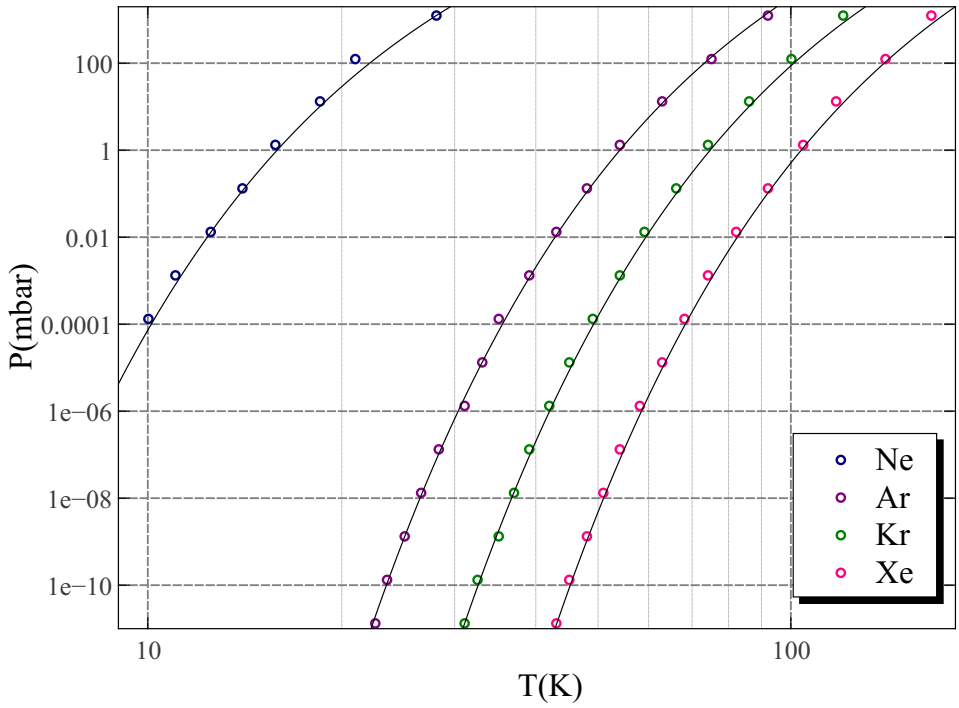

Figure 2.1: Experimental data of the vapor pressure of rare gases between 10 K and 110 K. Curves are the fits using equation 2.1.

Energy deposition One of the most important characteristic of a material in the particle detection field is its ability to stop and to absorb the incident radiation. Of course, the nature of the incoming detectable particles gives rise to different interaction mechanisms.

When a quantity of energy is deposited into RG (liquid or solid), the processes that occur are the excitation, the ionization and the sub-excitation of the electrons. The latter process occurs when the electrons liberated in the ionization, excite other atoms. The excited atoms and some of the electrons from ionization recombine and subsequently decay and emit light. The remaining electrons from ionization can instead be collected in an electrode using an electric field. The interaction between a particle and the atoms of a medium is given by the Bethe-Block equation which describes the energy loss $\partial E/\partial x$ versus the energy of the incident particle. The curve has a minimum at $\beta\gamma \sim 3$ and particles with energy that corresponds to this value are known as "minimum ionizing particles" (MIP).

For MIPs, $\partial E/\partial x$ has a constant value for a given material.

The energy deposited E_0 in the RG medium can be written using the Platzman equation [87]:

$$E_0 = N_i E_i + N_{ex} E_{ex} + N_i \epsilon \tag{2.2}$$

where N_i are the electron-ion pairs and E_i is the average energy amount to create each of them; N_{ex} and E_{ex} are the number of excited atoms and the average energy to excite them, respectively. ϵ is the average kinetic energy of sub-excitation electrons. The W-value, can be then defined as:

$$W = \frac{E_0}{N_i} = E_i + E_{ex}\frac{N_{ex}}{N_i} + \epsilon \tag{2.3}$$

and considering the electronic band structure of RG liquids and solids, it is possible to obtain the equation in term of the energy band gap E_{gap}:

$$\frac{W}{E_{gap}} = \frac{E_i}{E_{gap}} + \frac{E_{ex}N_{ex}}{E_{gap}N_i} + \frac{\epsilon}{E_{gap}} \tag{2.4}$$

For argon, kripton and xenon the ratio W/E_{gap} is constant and the calculated value is $\approx$1.65 which is in agreement with the measured data.

When a particle is absorbed in a medium, the energy deposited can also be converted into photons. The parameter used in this case is the light yield (LY) which is defined as the number of emitted photons for a given incident energy and it is often expressed in photons (γ) per MeV or KeV. The ionization yield (also charge yield) is instead the number of ionizing electrons produced per unit of absorbed energy. It is inversely proportional to the W-value [89].

All the quantity above described are summarized in the table 2.4 for all the RG. Furthermore, since these parameters are temperature dependent, when possible, is shown the value for the gas, the liquid and the solid phases.

Drift Velocity When electrons are released into the RG, they can drift under an electric field and can be collected as a charge signal. The drift velocity of electrons v_{e^-d} into the dielectric material is a function of the electric field E:

$$v_{e^-d} = \mu_e \cdot E \tag{2.5}$$

where μ_e is the electron mobility, and in case of weak electric field and small carrier concentration, μ_e is independent of the electric field and can be written using the

Physical property	Ne	Ar	Kr	Xe
Atomic number Z	10	18	36	54
Heat capacity in liquid c_p (kJ/kg K)	1.84	1.05	0.538	–
Heat capacity in solid c_p (kJ/kg K)	1.302	0.833	0.428	–
Viscosity at liquid η (10^{-7}kg/m s)	1240	2760	1600	–
Thermal conductivity in liquid λ (mW/m K)	113	125	90	71
Refractive index in liquid at 0.5 μm R_i	1.23	1.23	1.30	1.38
Refractive index in solid at 0.5 μm R_i	–	1.23	1.35	1.44
Dielectric constant in liquid ϵ	1.59	1.63	1.93	–
Dielectric constant in solid ϵ	1.67	1.80	2.23	–
Solubility in water (vol/vol)	0.014	0.0537	0.099	0.203
Energy gap in liquid E_{gap} (eV)	–	13.4	11.55	11.67
Energy gap in solid E_{gap} (eV)	21.4	14.2	11.6	9.28
W-value in liquid (eV)	–	23.6	18.4	15.6
W-value in solid (eV)	–	–	–	12.4
Electron mobility in liquid μ_e (cm^2/(Vs))	$1.6{\cdot}10^{-3}$[*]	475	1800	2950
Electron mobility in solid μ_e (cm^2/(Vs))	600	1000	3700	4500
MIP energy loss in liquid $\frac{\partial E}{\partial x}$(MeV/cm)	2.04	2.105	3.28	3.7
Ionization yield in liquid CY (e$^-$/KeV)	–	7.4	–	4.7
Ionization yield in solid CY (e$^-$/KeV)	–	–	–	–
Light Yield in liquid LY_{liquid} (γ/KeV)	7	40	25	46
Light Yield in solid LY_{solid} (γ/KeV)	–	–	–	–
Emission wavelength $\lambda_{emission}$	78	128	–	178
Polarizability $\alpha(\times 10^{-24}\text{cm}^3)$	–	1.66	–	4

Table 2.4: Principal physical properties of rare gases. "-" means that no value has been found in literature. *This value refers to the mobility of the "electron-bubble". The structure is composed of a macroscopic void that surrounds electron in liquid neon. Data from references[88, 89, 90, 91, 85].

Nernst-Einstein equation:

$$\mu_e = \frac{eD}{K_b T} \tag{2.6}$$

where e is the electron charge, D is the diffusion coefficient, T is the temperature and K_b is the Boltzman constant.

Generally, the behavior of electrons in the condensed rare gases is classified through the mobility in the zero field approximation (μ_0). If $\mu_0 > 10\,\mathrm{cm}^2/\mathrm{Vs}$ the electrons are considered "quasi-free" and it means that these electrons are very mobile, otherwise, if $\mu_0 < 0.1\,\mathrm{cm}^2/\mathrm{Vs}$ the electrons are said to be "localized" in deep traps. In heavy rare gases (liquids and solids) the electrons are mostly quasi-free due to the high polarizability of RG atoms and the strong interaction between polarized atoms in the electron field [89].

V_0 energy In dense media, such as RG in the liquid or solid phase, electrons interact with different atoms at the same time. Depending on the polarizability of the atoms, a dipole-dipole interactions can take place. To describe this phenomenon, we introduce the V_0 energy. The V_0 is the potential energy of the ground state of quasi-free electrons in the condensed media. Considering the work function in the liquid or gas phase Φ_i (where i is the gas or liquid), we can write:

$$\Phi_i = \Phi_{vac} + V_0 \tag{2.7}$$

where Φ_{vac} is the work function in vacuum. Equation 2.7 shows that V_0 is the energy necessary to bring an electron from the vacuum into the liquid or solid. Positive V_0 means that free electrons within the RG liquid or solid are more favored to be emitted [92].

Rare gas	T (K)	V_0 (eV)
Neon	37.5	0.6±0.1
Argon	85	-0.10±0.05
	82	0.00±0.05
	6	0.3±0.1
Krypton	123	-0.52±0.05
	114	-0.40±0.05
	20	-0.25±0.1
Xenon	162	-0.66±0.05
	60	-0.59±0.05
	40	-0.49±0.05

Table 2.5: Values of the V_0 parameter for RG at different temperatures.

Measured values of V_0 for rare gases at different temperatures are listed in the table 2.5 [93, 94]. The most often used experimental technique to estimate the V_0 energy is based on the measure of the work function of a photocathode in vacuum and the same photocathode immersed in the medium. The large discrepancy between the measured values reported in literature is related to the difficulty in this kind of measurements. Summarizing, the V_0 is the potential energy that exists at the interface between media and vacuum, and a positive value of V_0 means that electrons are more prone to be extracted from the condensed material.

Fluorescence In rare gases, fluorescence emission of an UV photon (γ_{UV}) follows a process that involves the excimer A_2^*:

$$A_2^* \rightarrow 2A + \gamma_{UV} \tag{2.8}$$

where A is one of the RG atoms. This process is well described in numerous studies [89, 95, 96]. Passing through rare gas atoms, the ionizing radiation (R) can generate electrons e, ions A^+ and excitons, i.e. atoms in an excited state (A^*) as follows:

$$R + A \rightarrow e + A^+; \qquad R + A \rightarrow A^* + R'; \qquad e + A^+ \rightarrow A^* \tag{2.9}$$

If the density is sufficiently high, this interaction produces excimer (A_2^*) in few picoseconds following the two processes:

$$A^* + A \rightarrow A_2^* \tag{2.10}$$

and

$$\begin{aligned} A^+ + A &\rightarrow A_2^+ \\ A_2^+ + e^- &\rightarrow A^{**} \\ A^{**} &\rightarrow A^* + \text{heat} \\ A^* + A &\rightarrow A_2^* \end{aligned} \tag{2.11}$$

Since dense RG are transparent to photons emitted through the radiative decay of excimer, this light can escape the detector media and can be opportunely detected. As an example the decay mechanism of argon is shown in the figure 2.2. A quenching mechanism of this process is related to the exciton-exciton collisions:

$$A_2^* + A_2^* \rightarrow 2A + 2A^+ + e \tag{2.12}$$

in which the electron loses kinetic energy befor recombination [96].

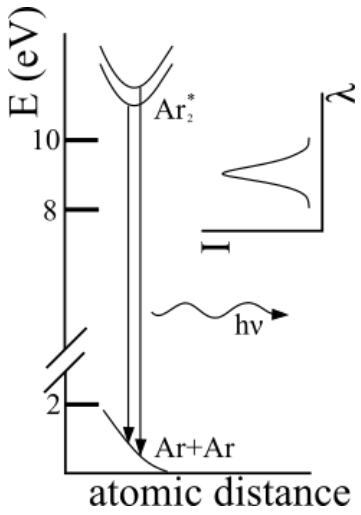

Figure 2.2: Sketch of the fluorescence decay of argon [96]. The excimer A_2^* is produced when the interacting particle releases its energy in the medium. The fluorescent UV photon ($h\nu$) is emitted consequently to the dissociation of the excimer as described in the text.

2.2 Rare gas crystals

At room temperature, rare gas atoms do not form stable chemical bonds between them. At standard temperature and pressure conditions all the rare gases are in the gaseous state; crystallization occurs only at very low temperatures and for this reason the solidified RG are called cryogenic crystals. Since the crystal lattice sites are occupied by identical atoms bound by weak and short range Van der Waals force, they belong to the class of molecular or atomic crystals [97].

Rare gas atoms do not have permanent dipole moments, thus Van der Waals force arises from correlation in the fluctuation of the dipole moments of RG. Quantum-mechanical fluctuations can in fact produce instantaneous electric dipole moment in one atom that induces dipole moments in the neighboring atoms. The attractive dipole-dipole force that results is the so-called Van der Waals force, which decreases rapidly with increasing distance. This force in fact binds atoms and molecules within few angstrom and beyond this distance the force is negligible. In the case of RG crystals, where the neighbor distance is $\sim$4 - 6 Å, the cohesive energies are typically of the order of 10 kJ/mol or 100 meV/atom. This

is the reason why RG crystals have low melting points. Furthermore, because the induced dipole moment is roughly proportional to the total number of electrons in the RG atom, the melting point of these solids increases with Z.

To describe the Van der Waals force in RG crystals, the most used empiric potential is the power function proposed by John Lennard-Jones (LJ) [98]. The LJ potential as a function of the distance r between the center of the atom, is expressed in the following equation:

$$\phi(r) = -\frac{A}{r^6} + \frac{C}{r^{12}} = 4\epsilon\left[\left(\frac{\sigma}{r}\right)^{12} - \left(\frac{\sigma}{r}\right)^{6}\right] \tag{2.13}$$

where the empirical constants ϵ and σ are the energy of interaction between two molecules and the collision diameter, respectively, the latter being the characteristic distance between two neighboring atoms. The following relations connect the parameters A and C with the empirical constants:

$$\sigma = \left(\frac{C}{A}\right)^{1/6}; \qquad \epsilon = \frac{C^2}{4A} \tag{2.14}$$

The cubic close pack (ccp) structure, which is centrosymmetric, is favored in RG due to the modification of the long-range Van der Waals force by the overlap of atomic excited states with the neighboring atoms in the crystal [97]. Figure 2.3 shows the cubic close pack structure. In this structure the lattice is a face centered cube with an RG atom at each lattice vertex. The lattice parameter (a) for the main RG solid crystals is presented in the table 2.6.

	Ne	Ar	Kr	Xe
a (Å)	4.43	5.26	5.72	6.20

Table 2.6: Lattice parameter a of RG crystals.

In view of their low melting and sublimation points, the preparation of RG crystals requires special solidification techniques. Bulk samples of large dimensions ($\gtrsim 100\,\mathrm{cm}^3$) can be grown from the liquid phase in a closed chamber following the so-called Brigman-Stockbarger modified method. Furthermore, thin samples can be grown in a cryostat by a direct condensation of the gas onto a cooled substrate. These methods are explained in the next two paragraphs.

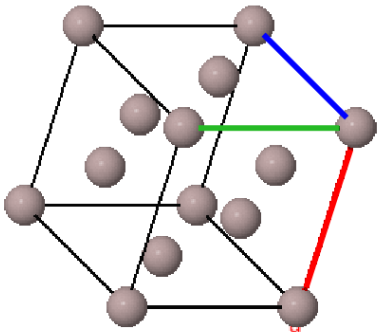

Figure 2.3: Sketch of the ccp structure with the three orientations shown by red, green and blue axes.

Vapor deposition technique The vapor-deposition-growing-technique is the easier way to form an RG solid. In this technique, the crystals are grown at a pressure and temperature below the triple point and solidification takes place directly from the vapor without the presence of the liquid phase. The gas is sprayed onto a cold surface at a temperature under the melting point. Appropriate gas nozzle ensures a uniform growth with a typical rate of 1 mm/h or even lower since the pressure of the gas inside the chamber is maintained in the 10^{-5} mbar range. Following experimental observations, it is known that the maximum thickness of the crystal that can be obtained using this method is few millimeters. Often, the vapor deposition occurs by spraying the gas onto a transparent substrate that permits optical investigation of the specimen. Particular attention have to be paid in the vapor deposition since only with a low growing rate is possible to stack properly every layer of atoms and obtain thus high-optical-quality crystals.

Such a technique is used as an example in the positron annihilation spectroscopy (PAS). In the PAS, positrons can be implanted into films of rare gases such as solid neon, cooled and then studied [99, 100].

Finally, it is also interesting to note that this technique is easily modifiable to obtain doped RG crystals. In fact it is sufficient to mix the rare gas with the doping atoms or molecules and then spray the mixtures. This experimental method, known as matrix isolation technique, will be discussed in detail in section 2.3.

Bridgman-Stockbarger modified method The Bridgman-Stockbarger (BS) technique is a growing method developed from the Nobel prize P. W. Bridgman in the 1925 for the growth of crystals from the melt phase at high temperatures. The principle of the BS technique is the slow solidification of the melt phase. This happens by translating the hot liquid-zone in the direction of growing while a solid crystal is progressively formed behind the liquid. The chamber is filled with the liquid material at a temperature just above the temperature of melting. Starting from the bottom part of the container, where a crystal seed is located, the temperature is slowly lowered at a certain rate, typically of the order of 1 Kelvin/hour. In such a way, a temperature gradient is formed along the vertical direction, which is the direction of growing. The seed is a piece of single-crystal and it ensures a single-crystal growth along a certain crystallographic orientation. Also the temperature gradient need to be fixed at $\sim 1 - 2\,\mathrm{K/cm}$. Lowering the temperature, while maintaining a fixed gradient, the portion of the container below the solidification temperature increases, and a large crystal is progressively formed. Since a uniform crystallization in the horizontal plane is necessary for the growing of a single crystal, the radial dimension of the chamber cannot be too large.

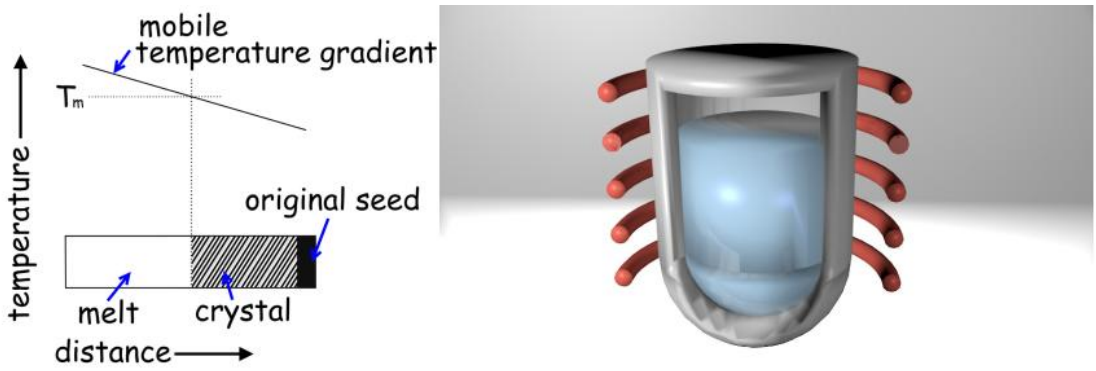

Figure 2.4: Left side: visual representation of the Bridgman-Stockbarger growing technique. Right side: drawing of a possible container surrounded by heaters.

For the growth of RG solids the Bridgman-Stockbarger method is opportunely modified to operate at cryogenic temperatures and it is also named liquid-freezing or gradient-freezing technique. Figure 2.4 shows a summary diagram and a sketch of a possible chamber for the BS growing technique.

The general rule is that the growth from the vapor produces finer grained and

more defective poly-crystals with respect to the growth from the liquid.

2.2.1 Crystal defects

Crystal defects are all the imperfections in the regular lattice arrangement of the crystalline structure.

Defects can have different origins, such as different atomic species present in the structure, deformation of the solid, rapid cooling from high temperature or high-energy ionizing radiations. These defects influence the mechanical, electrical and optical behavior of the solid crystal. The simplest type of defect in a crystal is a missing atom in a lattice site and it is called vacancy. Another type of simple defect occurs when an atom occupy an interstitial space in the lattice. These kind of dislocations include the Frenkel and the Schottky type of defects [101]. Moreover, if in the lattice structure is present an atom of a different species from the host crystal atoms, it is called an impurity. Impurities may either occupy interstitial spaces or substitute an host atom in its lattice site [102].

When these dislocations involve more points we could have different behavior. Line defects are lines along which atoms are arranged without following the principal lattice structure. When the defects group a whole plane of the crystal structure, they are called surface defects and can occur between two grains or two different structures. The external surface of a crystal is also a surface defect because the atoms on this plane adjust their positions to accommodate for the absence of neighboring atoms outside the surface [103].

In RG crystals, at a finite temperature, the Helmoltz free energy F or the Gibbs free energy G of a real crystal has a minimum for arrangements where a certain fraction of lattice sites are unfilled [86]. Vacancies are thus almost always present in RG crystals and should be considered when treating these solids since they influence various physical properties. As concerns the impurities in RG crystals the most common are other rare gases, nitrogen and water. As an example, the extremely high solubility of xenon in water, which is higher than for instance nitrogen, implies that trace of water are very difficult to remove from xenon. Recent chromatographic analysis of highly purified xenon shows that water is the dominant impurity [104]. Rare gases crystal generally can tolerate an impurity concentration in the order of part per million (ppm) without generating much

problems to the lattice. If too many impurities are present, they can coalesce to form clusters and destroy the crystal structure.

The effect of both chemical and isotopical purity on crystal grain size has not been investigated systematically for RG crystals, but experimental results with metals indicate that an impurity concentration of $\sim 50\,\mathrm{ppm}$ may limit the grain size and so limit the possibility of growing a single crystal.

Theoretically, a crystal which contains a large number of grains whose crystallographic orientations, volumes and shapes are statistically distributed over the whole crystal is defined as a poly-crystal. In poly-crystalline structures, surface defects are the majority. Single crystal or mono-crystalline solid denote instead a structure in which the lattice has the same orientation and is continuous and unbroken without grain boundaries. In single crystals, only a relatively low number of defects can be present.

Defects in general are important because they can cause an anomalous behavior of the crystal. Elastic, thermal, electrical and optical properties are strictly influenced by the presence of defects. Impurities and defects can have also important consequences in a crystals used for particle detection since they can alter the charge transport properties and the luminescence features of the solid. High-electronegativity impurity atoms can act in fact as charge trapping sites and capture the electrons during their drift within the crystal. Furthermore, also the light yield can be influenced by the presence of defects that could quench the signal. Both deep or shallow levels defects can in fact absorb fluorescence photons [105, 89].

While large voids and other coarse defects may be observed visually, structural imperfection can only studied with particular experimental technique such as the X-rays diffraction, which are difficult to apply at cryogenic temperatures. Unfortunately only an occasional investigation [86] of all these aspects have been done in solid crystals of rare gases and most of the parameters of interest are not reported in literature.

2.3 RG crystals doping: Matrix Isolation Technique

Crystals made of inert gases solidified at cryogenic temperatures have been used to trap and study reactive species in this low interacting environment. In this method, named Matrix Isolation Technique (MIT), the guest particles (atoms, molecules or ions) are embedded within a continuous matrix of solid crystals (matrices) made of the inert gases, such as RG. This technique is very useful and it presents many advantages with respect to other spectroscopic methods. In particular, as the matrices are made of un-reactive materials such as rare gases, only a feeble interaction between host and guest can take place [106].

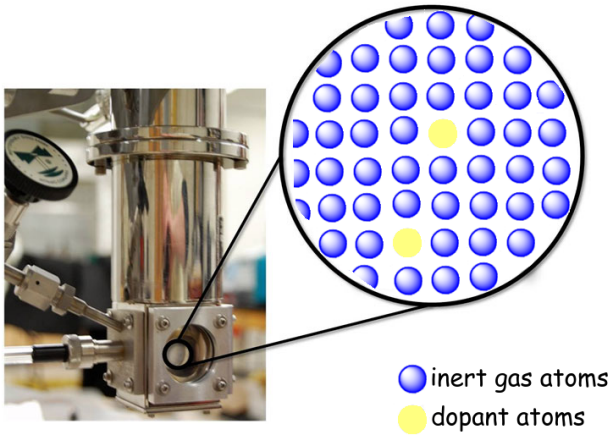

Figure 2.5: Visual representation of matrix isolation. The photo depicts the cold part of a cryostat equipped with an optical viewport that allows spectroscopic studies. The zoom sketch is an illustration of a matrix lattice with the different species of atoms (rare gas in blue and dopants in yellow).

Furthermore, since the environment is solid, the diffusion processes of the guest atoms in the matrix are strongly suppressed. Moreover, since a large number of guest atoms can be usually embedded into the solid, a higher density of guest particles with respect to spectroscopic studies in the gas phase can be obtained.

Matrix isolation has a long history in both chemical and physical communities. The first scientist that studied emission spectra of molecules of oxygen and nitrogen

embedded into solid matrices was the Nobel prize H. Kamerlingh Onnes in Leiden in 1924 [107]. But it was only in the '50s that G. Pimentel started to use solid RG as environment and invented the matrix isolation technique. In these initial experiments, since the lowest temperature available in his laboratory was 66 K, the matrices were made only of xenon [108, 107]. Finally, also the group of F. M. Pipkin gave an important contribution to the development of the matrix isolation technique with studies on the optical absorption spectra of alkali atoms in rare gas matrices [109] in the '60s. Nowadays, among chemical studies of the spectra of molecules [110, 111], matrix isolation is also a potentially useful method in quantum information and in fundamental physics researches [112, 113, 114] because of the relative experimental simplicity and the high optical density [115].

The most used experimental technique in matrix isolation is based on the vapor deposition (see the paragraph in section 2.2). The inert gas is mixed with the dopant atoms and sprayed onto the cold surface. Generally the cold surface is made of a sapphire plate which has a good thermal conductivity and is transparent in UV-VIS-NIR bands of the electromagnetic spectrum. Transmission spectroscopy is thus relatively easy to achieve with such systems. The figure 2.5 shows a sketch of a typical set-up for matrix isolation with optical viewports that allow optical spectroscopy both in absorption and in emission. Dopants excitation is mostly accomplished with pump laser systems while the light signal is often collected using spectrometers or monochromators.

Chapter 3

The proposed detection schemes

As discussed in chapter 1, many particles are possible candidates for the solution of the dark matter problem. Furthermore, all these candidates cover a very broad range of mass and thus a wide energy range must be probed with appropriate particle detectors or in high-energy accelerators. In this thesis, a particle detector based on rare gas crystals is proposed, which can be used to probe light WIMPs and axions with two different schemes. The excellent properties of rare gas atoms, previously described in chapter 2, make these materials excellent for the proposed idea. Such a hybrid detection concepts are characterized by a low energy threshold, a high detection efficiency and a low background. Furthermore, the proposed scheme can be scaled-up to a relatively large active volume. These schemes have been conceived in the framework of two INFN R&D projects named AXIOMA and DEMIURGOS, respectively. The work carried out in the framework of AXIOMA during the years 2015-2018 concerned the study of doped crystals and laser upconversion mechanisms for particle detection. Started in 2019, the DEMIURGOS project is instead focused on the study of rare gas matrices both doped and undoped as active materials for particle detection. A detailed description of the detection ideas at the basis of these two projects will be presented in the next sections.

3.1 Detection schemes

The two different detection schemes have been developed within the AXIOMA and DEMIURGOS R&D projects, they are both based on rare gas crystals and electrons' extraction from the solid-vacuum interface. The first scheme exploits undoped rare gases crystals maintained at cryogenic temperature to detect heavy particles such as dark matter WIMPs. Differently, the second scheme takes advantage of doped RG crystals. Guests atoms, such as alkali metals or rare earths can act as active centers where light particles such as axion can be absorbed. In the latter, the detection occurs using laser driven ionization techniques on the electronic energy levels of the guest atoms. In both cases, electrons detection occurs through high-efficiency charge sensors characterized also by a very low background. These two schemes are characterized by different energy threshold E_{th} i.e. the minimum detectable energy; in fact, in the undoped scheme $E_{th} \sim 100\,\text{eV}$ while in doped materials a threshold in the order of meV could be in principle reached. In this second case, the low-energy threshold can be reached only if the crystal is maintained under a laser pump providing the lacking energy necessary to ionize the atoms.

Even if the two schemes seem very different, they have many common elements, such as the matrices of rare gases, and also the development of many experimental processes is similar. In fact, the cooling system, the growing methods, the electrons' extraction and the electrons sensors are necessary for both the schemes. Furthermore, undoped RG crystals represent a first phase of the more complex doped scheme, which can be thought as an advanced phase. In the next two subsections I will describe in more detail all the aspects of these two detection schemes.

3.1.1 Scheme in undoped crystals

The detection scheme proposed in undoped crystals, is based on the direct ionization of the rare gas atoms when a DM particle scatters with the target nucleus of RG. Electrons that are generated according to this process can drift within the RG crystal under an electric field toward the crystal surface. Finally, they can be extracted and then collected into suitable in-vacuum sensors characterized by a

high sensitivity and a low background. Figure 3.1 shows a sketch of the detection scheme in such undoped crystals.

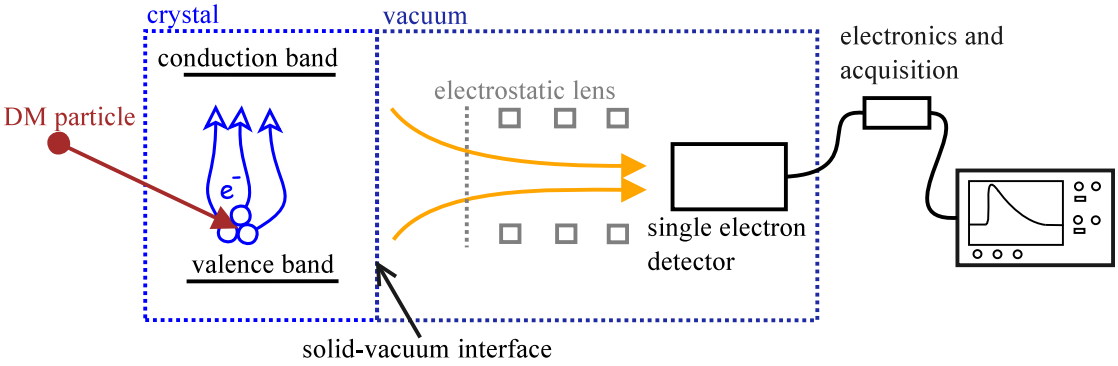

Figure 3.1: Sketch of the proposed detection scheme in undoped crystals of rare gas. Ionization process occurs when the incoming particle hits the atom of the detector. Free electrons can drift within the crystal toward the solid-vacuum interface where they can be extracted in vacuum and finally these electrons can be collected into suitable detectors.

The process of electrons' extraction from the solid-vacuum interface can be described with a formalism that takes into account the potential energy V_0 previously described in section 2.1. Electrons released after the WIMP scattering, exist in a quasi-free state in the condensed rare gas. Their behavior near the solid surface can be described in terms of a 1-dim potential energy (V) with the coordinate z orthogonal to the surface plane and the origin in the surface [116]:

$$V(z) = \begin{cases} V_0 - eE_1 z + A_1 & z < 0 \\ -eE_2 z + A_2 & z > 0 \end{cases} \tag{3.1}$$

$$A_{1,2} = \frac{-e^2(\epsilon_1 - \epsilon_2)}{4\epsilon_{1,2}(z + \beta z/|z|)(\epsilon_1 + \epsilon_2)} \tag{3.2}$$

where ϵ_1 and ϵ_2 are the dielectric constants of the RG and the vacuum, respectively and $\epsilon_1 E_1 = \epsilon_2 E_2$. β is a parameter which corresponds to the thickness of the transition layer between the solid and the vacuum. Electrons with a momentum in the z-axis p_z higher than the threshold value $p_0 \approx \sqrt{2m_e|V_0|}$ have sufficient energy and can be emitted through the solid-vacuum interface. Here, two cases have to be considerd depending on the potential barrier V_0. In solid krypton and

xenon, as shown in table 2.5, the potential barrier is negative and high in module ($|V_0| > K_bT$) and to achieve an efficient emission, electrons must be accelerated applying a strong electric field E. On the other hand in solid neon and argon, V_0 is positive and this means that only a thin potential barrier has to be crossed by the electrons. In these latter crystals, electrons emission occurs at very low electric field applied. The number of electrons that are emitted are thus controlled only by the lifetime of excess electrons before their capture by impurities or other traps and so it depends on the crystal quality.

Once electrons are released in vacuum ($P < 10^{-6}$ mbar), they can travel towards appropriate devices for their detection. Electrostatic lenses, also called Einzel lenses (EL), combined with electrostatic mirrors can be easily mounted and they allow to focus electrons in small spots where "single-electron-detection" sensors are present. EL are basically constituted by three metallic rings kept at different voltages. Inside these rings, the electric field is such that electrons' trajectories are curved, reproducing the effect of an optical lens for photons. The overall performance of the lens is due to the spread in energy of the electrons. In the case of the proposed scheme, a finite-elements simulation of the problem suggested that a good focusing effect can be achieved with a single lens coupled with an accelerating grid.

Electron sensors with sufficiently high efficiency and low background rate are commercially available. Regarding the purposes connected to the proposed scheme, three different kind of sensors have been considered: multichannel plate assembly (MCPA), channeltron systems and fast luminescence phosphor coupled with light detectors. MCPA and channeltron are similar devices that works as electrons multipliers: they take advantage of high efficiency secondary electrons emission materials. These devices have a single electron sensitivity and, depending on the dimensions, they can have a dark count rate smaller than ~ 100 mHz [117]. Luminescence phosphor instead converts the charge signal into UV light and thus it needs to be coupled to a photomultiplier tube (PMT), a silicon photomultiplier (SiPM) or other light detector. A typical efficiency of the charge-light phosphor is ~ 1 photon in the UV range every ~ 2 electrons with an energy of 6 keV [118]. In this case, the limiting factor is represented by the relative high dark count of the photomultiplier tube. A solution can be the use of SiPM, which are very sensitive to "single photon" and moreover, if cooled down at low temperature, they can have

a very low dark count rate lower than 5 mHz/mm^2 at 50 K [119, 120].

Differently from the dual phase TPCs filled with argon or xenon that exploit two light signals as described in section 1.2, the proposed scheme exploits the direct detection of "in-vacuum" electrons. This second solution can be more efficient with the respect to light collection. Regarding the light signal, one has indeed to consider the quantum efficiency of the photomultiplier tube and also the solid angle of light emission which affect the detection efficiency. As previously described in section 1.2, the detection threshold of ionization detectors that exploit only scintillation signals, such as noble liquid TPCs, is in fact limited to the level of about 10 keV of deposited energy. A direct detection of the electron emitted can instead lead in a lower energy threshold scheme as it will be discussed in section 3.1.2. Clearly, to obtain a high-vacuum level outside the crystal, which is necessary for the usage of "in-vacuum" charge detectors, it is fundamental to consider the vapor pressure of rare gas. The behavior of this crucial parameter is shown in figure 2.1 in section 2.1. A pressure lower than 10^{-5} mbar can be reached only if the RG is in the solid phase at a temperature lower than the triple point. Moreover in this condition the crystal has a higher density with respect to the liquid phase ensuring thus a higher interaction probability for the same volume.

WIMPs interaction Considering a classical scattering between a WIMP particle with mass m_W and a nucleus with mass m_N, the nuclear recoil energy is given by the following equation:

$$E_{NR} = \frac{1}{2} m_W v^2 \frac{4 m_W m_N}{(m_W + m_N)^2} \frac{1 + \cos\theta}{2} \tag{3.3}$$

where v is the velocity of the DM particle and θ is the scattering angle. Equation 3.3 describes the isotropic scattering, but in the general case one has to consider the form factor $F(q)$ that contains the entire dependence on the momentum transfer (q).

Given the density $\rho(x)$, the form factor can be expressed as the Fourier transform of the scattering site positions:

$$F(\vec{q}) = \int d^3x \rho(\vec{x}) e^{i\vec{q}\cdot\vec{x}} \tag{3.4}$$

which can be written for spin independent (SI) and spin dependent (SD) interaction

as:

$$F(\vec{q})_{\mathrm{SI}} = \frac{3[\sin(qr_n) - qr_n\cos(qr_n)]}{(qr_n)^3} e^{-(qs)^2/2} \tag{3.5}$$

and

$$F(\vec{q})_{\mathrm{SD}} = \frac{\sin(qr_n)}{qr_n} \tag{3.6}$$

Equation 3.5 is the Wood-Saxon approximation which represents the Fourier transform of a solid sphere of radius r_n, which in turn expresses the nuclear radius with a skin thickness s, while equation 3.6 is a first approximation for the spin dependent interactions that must be extended with nuclear physics calculations.

Using the same notation of spin independent and spin dependent terms it is possible to express the cross section for a WIMP-nucleus interaction in the case of zero momentum transfer [121]:

$$\sigma_{0\mathrm{WN}} = \frac{4\mu_A^2}{\pi}[Zf_p + (A-Z)f_n]^2 + \frac{32G_F^2\mu_A^2}{\pi}\frac{J+1}{J}(a_p\langle S_p\rangle + a_n\langle S_n\rangle)^2) \tag{3.7}$$

where f_p, f_n and a_p, a_n are the effective spin independent and spin dependent couplings of the WIMP to proton (p) and neutron (n), respectively. Z, A and J are the atomic number, the mass number and the total nuclear spin, respectively. μ_A is the reduced mass WIMP-nucleus expressed as:

$$\mu_A = \frac{m_W m_N}{m_W + m_N} \tag{3.8}$$

Finally, the term $\langle S_i\rangle$ with $i = p, n$, is the expectation value of the total proton (p) or neutron (n) spin operators with the nucleus $\langle S_i\rangle = \langle J|S_i|J\rangle$. These values can be found in literature for many materials [122].

In the case of spin-independent interaction $f_p \simeq f_n$ and equation 3.7 can be written as:

$$\sigma_{0,\mathrm{WN-SI}} \simeq \frac{4\mu_A^2}{\pi} f_n^2 A^2 = \sigma_{\mathrm{SI}}\frac{\mu_A^2}{\mu_n^2}A^2 \tag{3.9}$$

where $\mu_n = (m_n m_W)/(m_n + m_W)$ is the reduced mass between WIMP and nucleon. Therefore, the spin-independent WIMP-nucleus cross section can be written as follows:

$$\sigma_{\mathrm{SI}} = \frac{4\mu_n^2 f_n^2}{\pi} \tag{3.10}$$

From the dependence $\mu_A^2 A^2$ of equation 3.9 it is clear that heavy target is preferable to obtain larger signals.

Combining the equations 3.3 and 3.10 regarding the energy deposition and the cross section and the velocity distribution of the WIMP particles described in section 1.1.3, is possible to derive the rate of events expected in the detector. In a time interval dt, each nucleus of the detector interacts with any WIMP with a velocity v inside a volume $dV = \sigma_{\mathrm{WN}} v dt$. The number of WIMPs inside the volume and moving with a velocity distribution $f(\vec{v})$ as described in equation 1.12, is:

$$dN = n_0 f(\vec{v} + \vec{v_E}) \sigma_{\mathrm{WN}} v dt \tag{3.11}$$

where v_E is the velocity of the Earth with respect to the Galaxy as already described in section 1.1.3 and n_0 is the local number of WIMPs of mass m_W:

$$n_0 = \rho_{\mathrm{DM}} / m_w \tag{3.12}$$

The differential interaction rate dR between WIMPs and target atoms in the detector is thus the interaction per nucleon times the number of nuclei per kilogram of material:

$$dR = \frac{N_A}{A} n_0 f(\vec{v} + \vec{v_E}) \sigma_{\mathrm{WN}} v d^3\vec{v} \tag{3.13}$$

where N_A is the Avogadro's number $N_A = 6.022 \cdot 10^{23}$. Finally, in a simplified case where the Earth velocity can be neglected, and that the maximum WIMP energy tends to infinite, the differential rate can be written as:

$$\frac{dR}{dE_{\mathrm{NR}}}(E_{\mathrm{NR}}) = \frac{R_0}{E_0 r} e^{-E_{\mathrm{NR}}/E_0 r} \tag{3.14}$$

where r is defined as a dimensionless parameter $r = 4\mu_A^2 / m_W m_A$, $E_0 = m_W v_0^2 / 2$ is the most probable WIMP energy, and R_0 which is the total WIMPs rate, can be expressed as:

$$R_0 = \frac{2}{\sqrt{\pi}} \frac{N_A}{A} n_0 \sigma_{WN} v \tag{3.15}$$

Equations 3.14 and 3.15 allow to evaluate the global interaction rate of expected events per detector mass unit and acquisition time as a function of the recoil energy of the WIMP-nucleus scattering for fixed values of σ_{WN}, v and A. Figure 3.2 shows the integral rate as a function of the nuclear recoil energy for WIMPs of mass $100\,\mathrm{GeV/c^2}$ using as velocity and density the commonly used values of $220\,\mathrm{km/s}$ and $0.3\,\mathrm{GeV/c^2 cm^2}$, respectively. Furthermore the value of $10^{-42}\mathrm{cm^2}$=1 ab has been assumed as an arbitrary spin-independent cross section. This quantity has

been chosen because it is the order of magnitude of the actual limit in the search for light WIMPs in the mass range under 10 GeV as shown in figure 1.7. The figure 3.2 shows the simulated curve for different rare gases. In case of the more complex spin-dependent interaction one has to consider in addition the net spin of the nucleus.

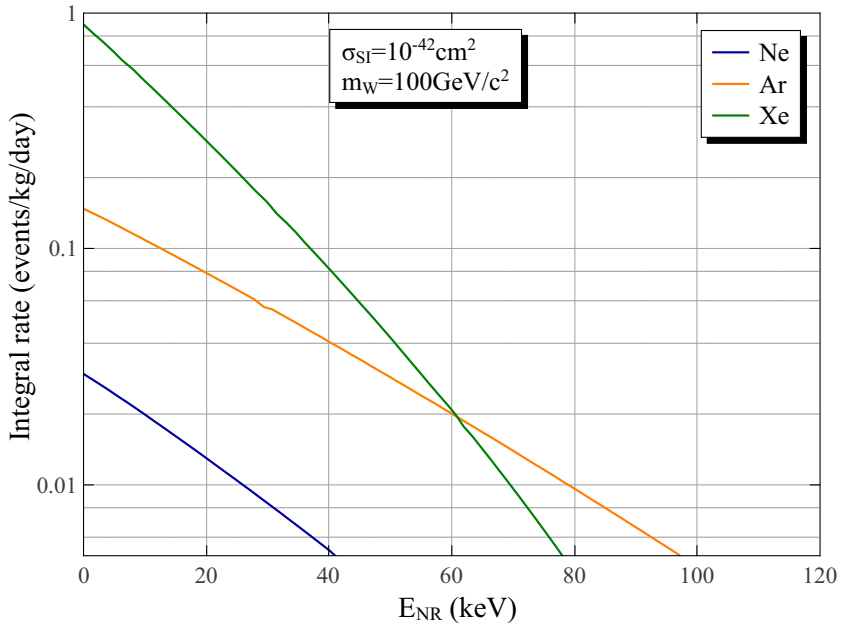

Figure 3.2: Integral rate of WIMP-nucleon scattering versus the nuclear recoil energy assuming perfect energy resolution and isothermal halo model. We used $v = 220\,\mathrm{km/s}$, $m_W = 100\,\mathrm{GeV/c^2}$ and $\sigma_{SI} = 10^{-42}\,\mathrm{cm^2}$. Curves are calculated for different rare gas materials (Ne, Ar, Xe).

Equation 3.3 can be used to calculate, for a given target atom and a fixed energy threshold, the expected WIMP mass that is possible to probe in the proposed detection scheme. For an energy threshold of 100 eV, which means few electrons detected, it results: $m_W \sim 100\,\mathrm{MeV/c^2}$ with a neon detector, $m_W \sim 300\,\mathrm{MeV/c^2}$ in argon crystals and finally $m_W \sim 500\,\mathrm{MeV/c^2}$ using xenon. Equation 3.15 gives furthermore an idea of the expected event rate for the different RG. Clearly, from equation 3.12, the rate will increase for lighter WIMPs mass, and for instance, considering $m_W \sim 500\,\mathrm{MeV/c^2}$ in a detector made of xenon, one can estimate an interaction rate of $\sim 5\,\mathrm{mHz}$ per kilogram of detector.

3.1.2 The scheme in doped matrices

A low-energy-threshold design can be obtained following a scheme similar to the infrared quantum counter (IRQC) concept proposed by the Nobel prize N. Bloembergen in the '50s to efficiently detect infrared (IR) photons [123]. This scheme takes

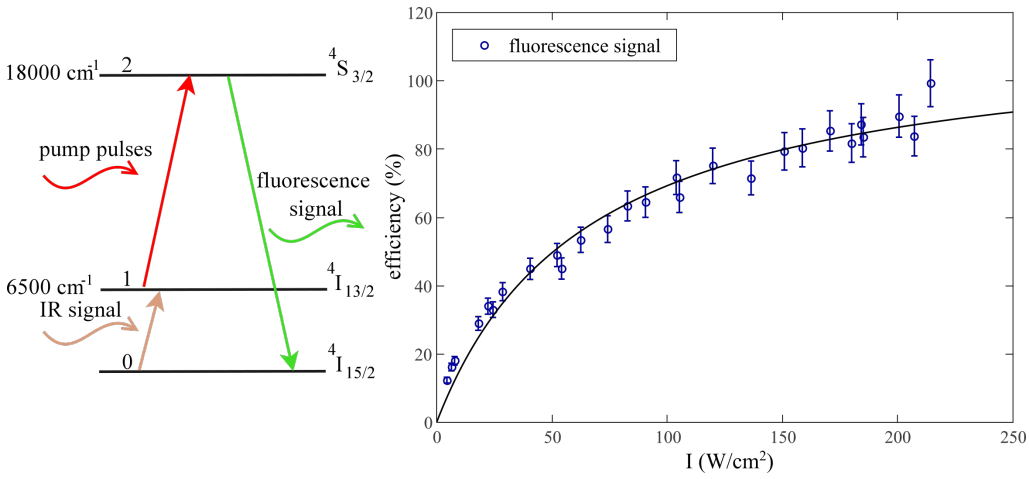

Figure 3.3: On the left side the IRQC scheme in Er^{3+} atoms. Infrared photons at $\sim$1.5 μm are absorbed between ground state (0) and first excited level (1). Here a laser pump is tuned to the transition $1 \rightarrow 2$ and finally a fluorescent photon in the visible band is emitted from level 2 to the ground state. On the right side, the efficiency of the upconversion process is shown both measured and simulated. For a laser intensity of about 200W/cm^2, the efficiency is about 90%.

advantage of the internal electronic energy levels of atoms embedded into suitable matrices, combined with pump laser upconversion. IRQC schemes are usually applied to trivalent-rare-earths-doped-oxides or fluorides crystals such as yttrium aluminum garnet (YAG), yttrium oxide (Y_2O_3), alumina (Al_2O_3), lutetium aluminum garnet (LuAG), yttrium lithium fluoride (YLF), lantanum fluoride (LaF_3), etc. In the IRQC scheme, an infrared photon is absorbed in the crystal by a low lying energy level of the dopant and successively up-converted into a photon in the visible range, exploiting a near-IR laser pump. Efficiency higher than 90% was achieved in the detection of 1.5 μm photons using an Er^{3+}:YLF crystal at 15 K, as shown in the figure 3.3 [124] on the right. In this figure, solid line is the analytical solution of the system of differential equation that takes into account the lifetime

of the level, the absorption cross section and the pump laser flux. The IRQC is a selective detector in the sense that only IR photon in a narrow-band range can be absorbed, up-converted and thus detected. This scheme is in fact resonant and the detection band is given by the linewidth of the transition from the ground state to the first excited level.

The proposed approach exploit a similar scheme to detect particles. Here, instead of IR photons, the incident energy is given by the detectable particle which releases its low-energy in the rare gas doped crystal. Furthermore, instead of a fluorescent photon, the AXIOMA scheme plans to exploit the detection of an electron whose emission from the crystal to the vacuum is triggered by the absorption of the incident particle. The figure 3.4 is a sketch of the ideal upconversion pro-

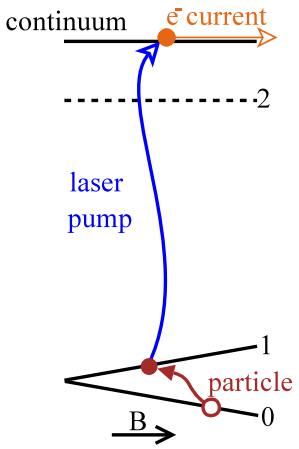

Figure 3.4: Sketch of the laser upconversion scheme proposed in doped crystals. If the energy deposited by the interacting particle is resonant with a fixed value of the magnetic field B, the atom absorbs the energy. Starting from level 1, a tunable laser upconvert the state to the continuum providing the lacking energy to ionize the atom.

cess of the proposed scheme. Once the incident particle is absorbed between the level $0 \rightarrow 1$, a laser pump (blue arrow in the figure) up-converts this level into the continuum and the so-called *laser induced ionization* can take place. Here the electron is released into the rare gas matrix where they can drift under the electric field. Since the scheme is resonant to the transition $0 \rightarrow 1$, only the particles whose released energy matches the energy Δ_{01} can be probed. To overcome this

problem and increase the detection range, the energy difference between the level 0 and 1 (Δ_{01}) can be opportunely tuned by exploiting the Zeeman effect using an external magnetic field B in the range $10^{-2}-10\,\mathrm{T}$. The meaning of the tilted lines of levels 0 and 1 in the picture 3.4 is thus the possibility to tune the levels with B.

In the proposed scheme, the laser upconversion efficiency can be easily expressed as:

$$\eta = \Phi_{ph}\sigma_1\tau_1 \tag{3.16}$$

where σ_1 is the ionization absorption cross section from level 1, τ_1 is the lifetime of the first level, and Φ_{ph} is the laser photons flux, which can be written as:

$$\Phi_{ph}=\frac{W_{laser}}{A_s \cdot h \cdot \nu} \tag{3.17}$$

where W_{laser} and ν are respectively the laser power and the laser photons frequency, h is the Planck constant and A_s is the area of the laser spot. In suitable materials, high efficiency values of the upconversion mechanisms can be obtained experimentally. An efficiency of more than 90% has been measured in a Er^{3+}:YLF crystal pumped with $\sim 870\,\mathrm{nm}$ photons, as shown in figure 3.3.

The linewidth of the transition $1 \rightarrow$ *continuum* plays an extremely important role in the scheme. This width must be thinner than the energy difference Δ_{01} to guarantee only the conversion of the atoms in the excited level. Any other laser absorption will in fact cause a spurious signal. To reduce this background noise, the transparency of the crystal at the laser pump wavelength is furthermore an important requirement. As already mentioned, impurities and crystal defects are the major causes of the absorption of the pump laser not in correspondence of the absorption of a particle in the $0-1$ transition.

A possible application of this detection scheme is to probe the existence of dark matter axions. They can in fact interact with the dopant atoms and trigger the transition $0 \rightarrow 1$. This application will be discussed in the next paragraph.

Axion interaction A well-established theoretical result is that dark matter axions can interact with fermions [125]. The interaction has the same form of the interaction of the spin magnetic moment with an effective magnetic field $\vec{H}_a$ given by:

$$\vec{H}_a = \frac{g_p}{2e}\vec{\nabla}\mathbf{a} \tag{3.18}$$

where g_p is the axion-fermion coupling constant and $\mathbf{a}$ is the axion field. Because of the large occupation number and the long De Broglie wavelength of the order of meters, the ensemble of axions can be treated as a classical field $a(x)$ named "axion wind":

$$a(x) = a_0 \exp\left(-i\frac{p^0 ct - \vec{P_E}\cdot\vec{x}}{\hbar}\right) \tag{3.19}$$

where $\vec{p_E} = m_a\vec{v_E}$, $p^0 \simeq \sqrt{m_a c^4 + \left|\vec{p_E}\right|^2 c^2} \simeq m_a c^2 + \left|\vec{p_E}\right|^2/(2m_a)$, m_a is the axion mass, v_E is the Earth velocity and a_0 is the field amplitude that can be computed by equating the total momentum transported by this field per unit of volume to the number of axions in a unitary volume (n_a) times the average momentum tensor [126]. This gives, in units of a momentum:

$$a_0 = \sqrt{\frac{n_a\hbar^3}{m_a c}} \tag{3.20}$$

The amplitude of the effective magnetic field $\vec{H_a}$ in units of Tesla is then:

$$H_a = \frac{g_p}{2e}\sqrt{\frac{n_a\hbar^3}{m_a c}}\frac{|\vec{p_E}|}{\hbar} = \frac{g_p}{\gamma m}\sqrt{\frac{n_a\hbar^3}{m_a c}}\frac{|\vec{p_E}|}{\hbar} = 9.2\cdot 10^{-}23\left(\frac{m_a}{10^{-4}\text{eV}}\right)\left(\frac{v_E}{270\text{km/s}}\right) \tag{3.21}$$

where the gyromagnetic ratio of the electron is fixed to $\gamma = 1.76\cdot 10^{11}\text{rad s}^{-1}\text{T}^{-1}$ and $g_p \simeq 4.07\cdot 10^{-11} m_a$ which derives from QCD calculations that relate mass and coupling constant of axion and neutral pion [127]. Such an equivalent magnetic field is periodic and thus equivalent to a radio frequency (RF) field and the corresponding modulation is fixed by the axion mass. The expected interaction rate R_i is finally given by [128]:

$$N_A R_i = \frac{2.13\cdot 10^3}{s}\left(\frac{\rho_a}{\text{GeV/cm}^3}\right)\left(\frac{10^1 1\text{GeV}}{f_a}\right)^2 g_i^2\left(\frac{\langle v^2\rangle}{10^{-6}}\right)\left(\frac{min(t,t_1,t_a)}{s}\right) \tag{3.22}$$

where N_A is the Avogadro's number, ρ_a is the axion density, g_i is a number of order one that gives the coupling strength of the axion to the target atoms, $\langle v^2\rangle$ is the mean square velocity of axions and finally $min(t,t_1,t_a)$ is the shortest time among the integration time, the radiative deceay time and the axion coherence time.

Since dopant atoms should stay in the ground state, the operating temperature of the crystal can be calculated comparing the thermal excitation rate (R_{th}) and

the expected axion interaction rate (R_i). In the material R_{th} is given by:

$$R_{th} = exp\left(-\frac{\Delta_{01}}{K_b T}\right) \cdot \frac{1}{\tau_1} \tag{3.23}$$

where K_b is the Boltzmann constant. For a given axion energy $E_a = h\nu_a$ in the range of milli-electronvolt, the crystal temperature must be lower than $\sim 60\,\mathrm{mK}$.

Once the electrons are released in the RG matrix, they can drift within the crystal under an electric field toward the solid vacuum interface. Here, as described in the section 3.1.1, they can be extracted and detected in-vacuum following the same scheme as in the undoped matrices. This is the reason why the scheme in undoped crystals represents also the basis for the more complex detection idea in doped matrices. Moreover, it is important to note that, since the doping is at a low concentration of the order of ‰ or %, the doped atoms do not represent a drawback for the drift of electrons, also because the rate of interaction is very low as compared with the electrons drift time.

A key role in the proposed scheme for axion detection is played by the energy difference Δ_{01} between the ground state and the first excited level. In order to absorb the axion in the material, this energy is required to be precisely tuned to the axion mass. Moreover, to maximize the energy transfer, a matching between the linewidths of the particle and of the radiative transition is requested. Regarding the axion, the scientific community agrees to consider its merit factor Q_a in the order of 10^6 for microwave transitions in haloscope experiments. On the other hand, in our system, the linewidth of the transition is fixed by the host-guest and guest-guest interaction in the matrices and it depends on the material. As an example, one of the best value of linewidth in solid crystal has been obtained in a Er^{3+}:YLF sample, where 1 Mhz [129] linewidths have been measured in optical transitions. In the presented scheme, a further limit is related to the energy difference between level 1 and 0 which has to be larger than the transition linewidth. Furthermore, since Δ_{01} is set using an external magnetic field controlled with an electromagnet, a precise current supply is needed to maintain B fixed.

Finally I want also to discuss about the possibility to use a different upconversion scheme that involves two separate laser pumps. In such approach, the first laser beam is tuned to the transition from the first excited level (1) to an intermediate energy level (3) where a non-radiative decay process bring the electron to a lower level (2). Level 2 has a long lifetime so it acts as an energy reservoir. A

second pump laser is then tuned from the level 2 to the continuum where again the electron can be emitted in the vacuum. Figure 3.5 shows schematically the idea above described. This two-laser-scheme can be preferable with respect to

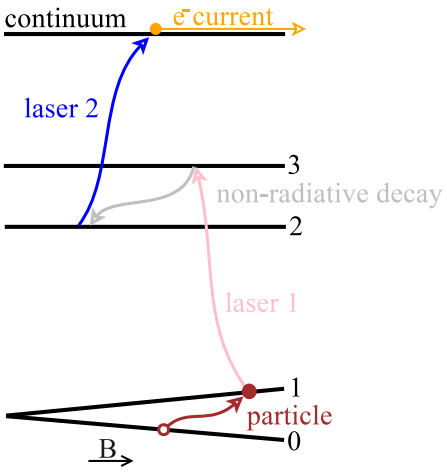

Figure 3.5: Two laser upconversion scheme. Following the transition $0 \rightarrow 1$ triggered by the incident particle, a first laser is required to up-convert the energy to an intermediate state and a second pump is necessary to ionize the atom.

the simple single-laser approach since in the single-laser scheme there is a strong constraint on the steepness of the ionization process. Considering conversely the two-laser approach, the internal energy level exploited in the transition $1 \rightarrow 3$ provides narrow lines and then the transition to the continuum must be narrower than the energy difference Δ_{3-2} which is less stringent than Δ_{0-1}. Moreover, in this scheme, the two photons of laser 1 and 2 have a lower frequency and thus the spurious absorption in a shallow level has a lower probability to happen. On the other hand, using two laser together requires a more complex experimental system, and, since two upconversion processes are involved, the total efficiency in this two-laser scheme is thus lower than that in the single laser approach.

3.2 Rare earths and alkali metals properties

In the doped scheme, the two principal properties of interest are the narrow transition linewidth and the long lifetime of the levels. The groups of atoms that present

these properties in their energy level scheme, belong basically at two different ensembles: the alkali metals and the rare earths (RE). Due to their unique properties, these atoms have been used frequently in spectroscopic studies. They have applications in both fundamental physics or quantum information [130, 131, 132, 133] and particle detection, especially as scintillators [134, 135] or IRQC [136, 137, 138]. Furthermore, our group have recently demonstrated the possibility to use Er^{3+} doped yttrium aluminum garnet and yttrium lithium fluoride in a novel scheme of particle detection [139, 140]. A brief discussion on the main properties of rare earths and alkali metals will be given in the next two subsections.

3.2.1 Rare earths

Rare earths are a group of 14 elements of the periodic table with atomic number Z between 58 and 71, that exhibit similar chemical properties. They are cerium (Ce), praseodymium (Pr), neodymium (Nd), promethium (Pm), samarium (Sm), europium (Eu), gadolinium (Gd), terbium (Tb), dysprosium (Dy), holmium (Ho), erbium (Er), thulium (Tm), ytterbium (Yb), and lutetium (Lu). Despite their name, RE atoms are not rare at all, being present in the Earth's crust with large abundances (for instance cerium is more abundant than copper). However, due to their large dispersion and the great difficulty to separate each other, RE are not easily available as other materials.

RE have a common configuration ($1s^2 2s^2 2p^6 3s^2 3p^6 3d^{10} 4s^2 4p^6 4d^{10} 5s^2 5p^6 6s^2$), occasionally an electron in the $5d$ state and an $4f$ orbital partially filled with $1 \rightarrow 14$ electrons. Often RE are present in the triply ionized form in which they lose their two electrons of the $6s$ orbital and one of the $5d$ shell. In this configuration the outermost electrons belonging to the $5p$ orbital act as a shield for the $4f$ shell that has a minor radial extension. This is the mechanism at the basis of the fact that rare earth atoms present narrow absorption and emission linewidths. The typical optical transitions in RE that are $4f \rightarrow 4f$ are forbidden due to parity conservation and can only exist because of the perturbation induced by the lattice field or other mixing phenomena. For the reason above described, RE exhibit long lifetime of the $4f \rightarrow 4f$ transitions both in absorption and in emission. Clearly, the lifetime depends on the matrix in which these atoms are embedded-in, and for instance in a crystal of potassium lead bromide (KPb_2Br_5)

doped with neodymium, it was observed a transition of 57 ms at 15 K [141]. On the other hand, these transitions are characterized by a very small cross section of about $10^{-19}\,cm^2$. The properties of RE described above, make these atoms interesting also as scintillators and for laser active media.

3.2.2 Alkali metals

Alkali metals consist of the atoms belonging to the first group of the periodic table, except for the hydrogen. They are lithium (Li), sodium (Na), potassium (K), rubidium (Rb), cesium (Cs) and francium (Fr). They have their outermost electron in a not completely filled *s-orbital* and this electronic configuration results in the similar chemical behavior of the group. The ionization energy and the Z of the alkali metals are listed in the table 3.1:

Alkali metal	Z	E_{ion}(eV)
Li	3	5.39
Na	11	5.13
K	19	4.34
Rb	37	4.17
Cs	55	3.89

Table 3.1: Atomic number and ionization energy of the alkali atoms [85].

As shown in table 3.1, alkali metals' ionization energy is very low and it is accessible using a commercial near-UV laser such as tunable optical parametric oscillator (OPO).

Alkali metals have been used a lot for fundamental physics researches and their internal energy level scheme is well known in literature [142, 143, 144, 145]. One of the best-known applications of the pure alkali elements is the use of rubidium and cesium in atomic clocks [146, 147, 148]. Moreover, many experiments of laser cooling and magneto-optical traps exploit alkali atoms because of their narrow transition lines [149, 150]. Fundamental physics researches exploiting atomic transitions of alkali metals have also been done in the last years [151, 152].

Unfortunately, the information reported in literature concerning alkali atoms embedded into rare gas matrices are very poor. Only few spectroscopic studies have

been done in the last years [153, 113, 112] and both the energy level structures and the linewidth of transitions are not well known. In this view, a goal of this thesis is also the characterization with spectroscopic methods of the behavior of these species embedded into RG solids.

Chapter 4

Extraction of electrons from solid neon

Since RG solid crystals have never been used as particle detectors except in a few tests [154, 155], at the initial stage of the AXIOMA and DEMIURGOS R&D projects, there were a lot of open questions regarding many aspects of the detection system. The feasibility of growing pure and high-quality RG crystals is the primary experimental question to deal with. It has been decided to start the tests using a neon crystal grown via the vapor deposition, since this technique requires an easier set-up with respect to the liquid freezing method. The goal was thus to find a procedure for crystal growing that provides a sufficient crystal-quality necessary for electrons' drift, and finally to demonstrate that electrons can be extracted from these solids and can be collected in vacuum.

The first objective was thus to develop an apparatus for the growth of RG crystals using the vapor deposition method that could be used for different gases without large changes in the system itself. To measure the drift of electrons within the solid, a system capable to inject charges into the crystal was also developed. In these initial tests I wanted also to understand the order of magnitude of the electric field necessary to extract free-electrons from the solid-vacuum interface.

In this chapter I will describe the set-up developed for the goals above described. I will also present a measurement regarding the electrons' extraction from a neon crystal. Finally, the results obtained will be briefly discussed.

4.1 Experimental apparatus

The experimental set-up developed for this initial stage consists of three different parts: the gas purification system, the cryogenic set-up and the optics and laser apparatus. The gas purification system is also common to other parts of the experiment, such as the large crystal growing set-up. In the following subsections all these parts will be discussed in detail. The entire apparatus is located in the high energy building at the Legnaro National Laboratory of INFN.

4.1.1 Gas purification system

The starting RG must be pure at a high level (contamination under the ppb) to avoid the quenching of the signal due to the charge trapping, which is mainly determined by high-electronegativity impurities such as oxygen [89].

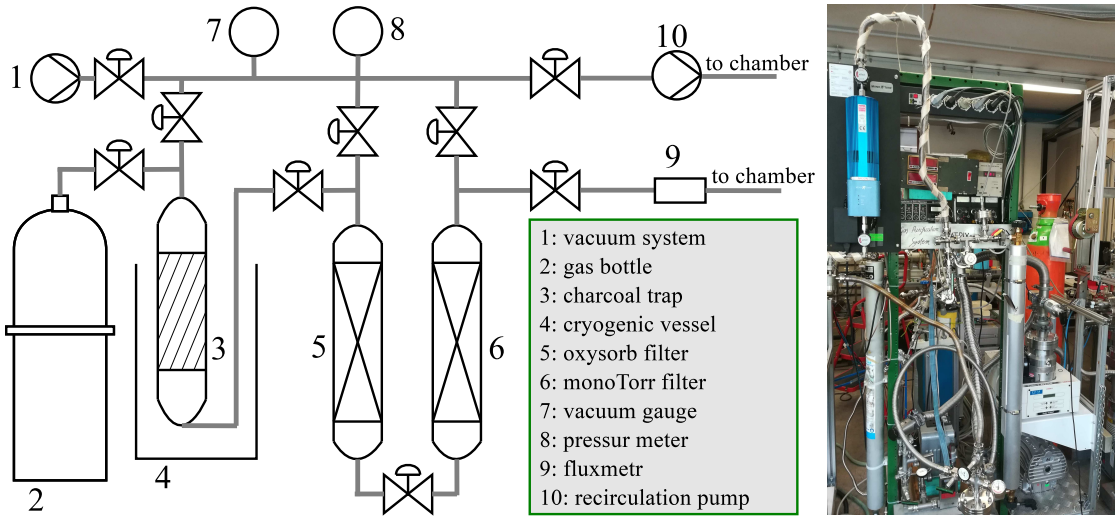

Figure 4.1: Sketch of the gas purification system. A caption of the figure is shown in the inset. On the right side there is a photo of the gas purification system mounted on a rack.

Different rare gas bottles can be connected to the gas purification system, sketched in figure 4.1. These starting materials are commercial gases with a nominal purity of 99.9999%. An activated charcoal filter (AC) is set after the gas bottle and it can be properly cooled using cryogenic liquids or pellets such as dry ice (solid CO_2), liquid nitrogen or others cooling bath mixtures. AC represents the first step in the purification system: it especially reduces the presence of hydrocarbons and moisture in the RG. The second and the third level of the purification system are an Oxysorb® and a MonoTorr® filters, respectively, and they are especially designed for oxygen, high electronegativity atoms and nitrogen impurities. Oxysorb® filter is a large cartridge made of chromium embedded in a SiO_2 lattice that absorbs oxygen and moisture by a chemical process. The MonoTorr® system is instead a heated getter material that forms irreversible chemical bonds with any oxide, carbide and nitride impurities. All-metal bakeable Nupro® valves with ConFlat® flanges connected to the adjacent components with copper O-rings have been used to avoid possible contamination. As shown in the figure 4.1, one part of the line is also equipped with a re-circulation pump. This part of the line can be used to form a loop circuit which contains the filters where the gas can be fluxed to clean the chamber and the ducts. The ducts circuit is also connected to a vacuum system made of a primary dry scroll pump [1] and a turbo-molecular pump [2] that allows a pressure lower than 10^{-7} mbar. A picture of the gas purification system is shown in the photo of the figure 4.1 on the right.

Considering the specification reported by the filters manufacturer, the purification system and the cleaning procedure described above guarantee a final impurity level in the RG gas, especially of high-electronegativity atoms, lower than ppb.

4.1.2 Cryogenic set-up

The core of the cryogenic set-up is the cryostat chamber where the crystals are grown and maintained at low temperature during the measurements. A picture of the apparatus is shown in figure 4.2 on the left side.

The chamber consists of a four-hole cross stainless-steel vessel equipped with four DN 200 ConFlat flanges. On the top flange of the chamber a two-stage-helium

[1] nXDS Edwards
[2] turbo V300 Varian

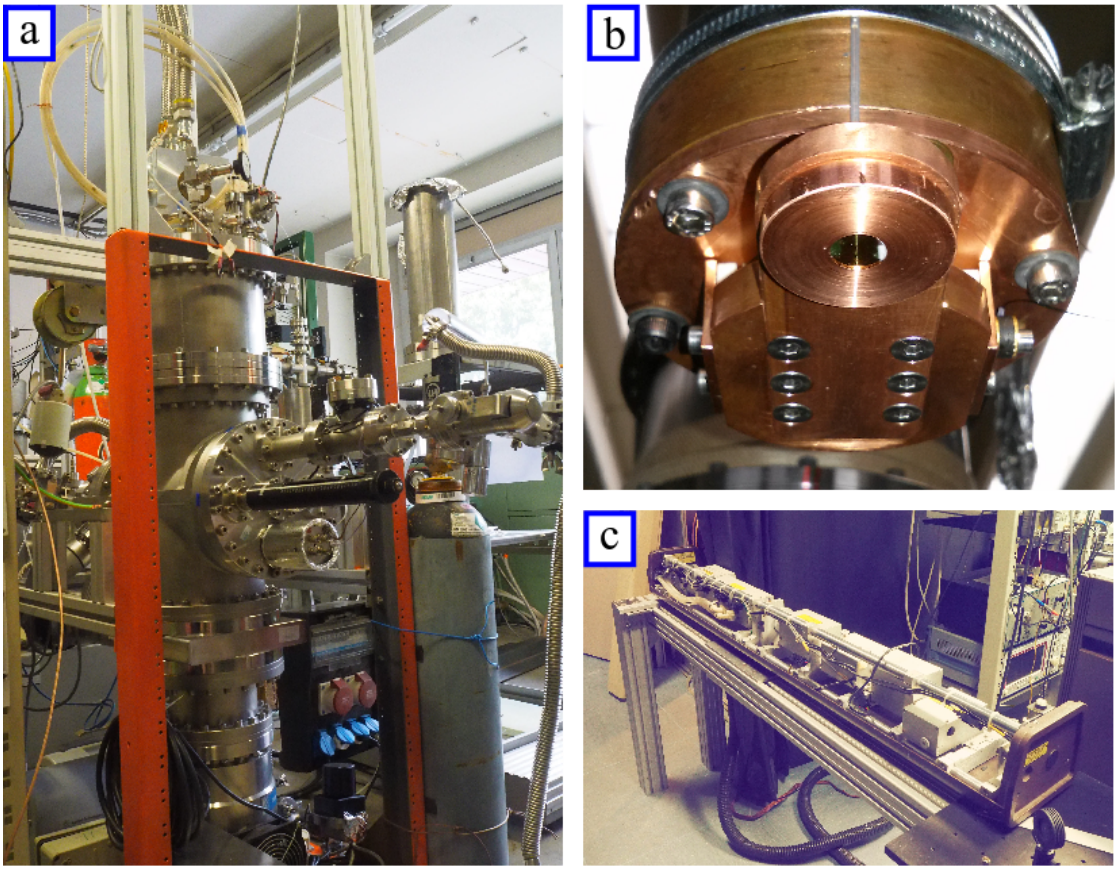

Figure 4.2: Picture a) is the photo of the cryostat chamber (front part). On the top of this picture we can see the pulse tube refrigerator and the optical fiber feedthrough. Picture b) shows the copper growth plate. In the center we can recognize the gold surface on the fused silica substrate. Finally picture c) shows the laser system.

pulse tube refrigerator [3] is mounted: it allows to reach a minimum temperature of 4.2 K with a cryogenic power of 1 W at this temperature. The cold finger of the pulse tube enters in the chamber and arrives at its center. It is also enclosed in a copper shield at 77 K covered with five foils of Mylar to reduce radiation heating. On the lower flange of the chamber, after a pneumatic gate valve, the vacuum pump system composed of a turbo-pump [4] and a scroll primary pump [5]

[3] Sumitomo RP82B2
[4] turbo V550 MacroTorr Varian
[5] nXDS Edwards

is mounted: it guarantees a pressure lower than 10^{-7} mbar. In the front side of the chamber, the vacuum manipulator is placed: it can set the position of the gas nozzle and the charge detectors inside the chamber, which can be placed in front of the cold finger. Finally, the last port on the rear is equipped with an optical window that allows a visual inspection of the chamber. Furthermore, on the back flange, two pressure gauges allow the measurement of both high vacuum [6] and pressure in the range $10 - 1000$ mbar [7].

A picture of the cold finger is shown in figure 4.2 on the right side. On the cold finger, the growth plate (GP), which consists of a 25 mm-diameter cylinder made of oxygen-free, high thermal-conductivity copper is attached. The GP is mounted off axis with respect to the center of the pulse tube and a good thermal contact between them is ensured by an indium foil placed in between. In the center of the GP, there is a 8 mm-diameter hole which is covered with a 100 nm-thickness gold foil evaporated on a substrate of 2 mm-thick UV grade fused silica window. Among the relatively-high thermal conductivity, fused silica has also a broad optical transparency from the UV to the NIR. The transmission of the UV light is indeed important because it is necessary that UV photons impinge on the gold surface. As we will see later, this is a basic request necessary to the generation of electrons in gold through the photoelectric effect. UV light is transported there using a 3 m-long quartz optical fiber that connects the laser system placed near the cryogenic set-up to the GP in the vacuum chamber.

Fine control of the GP temperature is ensured by the heating of the copper, accomplished through a 1 Ω high-power electrical resistor attached to the back part of the growth plate. The temperature is monitored using a commercial silicon diode sensor mounted in the proximity of the GP where the crystal will be grown.

In front of the growth plate, an aluminum mobile plate connected to the vacuum manipulator holds both the gas nozzle and the electrons' detectors. The gas nozzle is a 1 mm-diameter hole surrounded by a circular cone of 4 mm height and it is mounted at 30 mm-distance from the cold finger head. Next to the nozzle, two different kind of charge detectors are mounted: a charge receiver disk (CRD) and a microchannel plate assembly (MPCA). These two devices can be placed in front of the growth plate using the manipulator. The CRD consists of a 25 mm-diameter

[6] Pfeiffer PKR 251 Compact full range
[7] Balzers APR 010

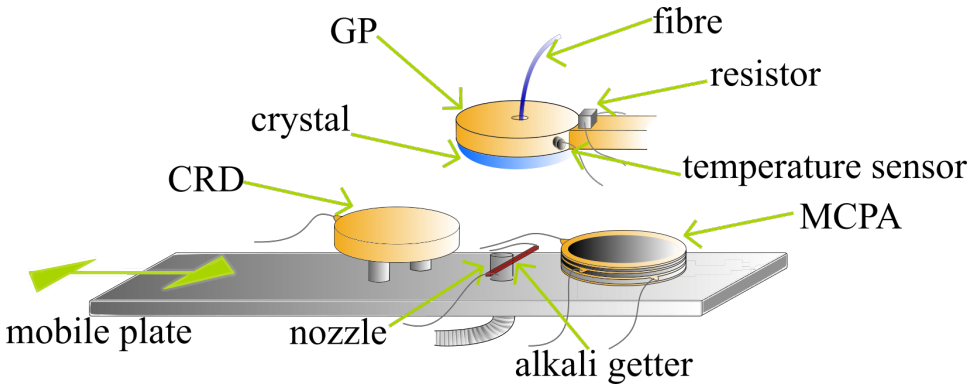

Figure 4.3: Sketch of the cold head assembly and the mobile plate in front of it. The distance between the growth plate and the electron detectors is 10 mm.

copper disk, isolated from the ground and connected by a vacuum feedthrough to an external safe-high-voltage (SHV) connector. The CRD acts as a Faraday cup for electrons collection and it can be placed at different voltage in order to obtain a variable electric field between the GP, which is at ground, and the CRD itself. The other electrons' detector is a double disk MCPA of $\pi\,\mathrm{cm}^2$-area [8]. MCPA are slabs of high resistivity material characterized also by a high-efficiency-secondary-electron emission. On these slices, a high density regular pattern of microchannels with a typical dimension of $\sim 10\,\mu$m is formed with lithographic techniques. The channels are spaced apart by $\sim 15 - 20\,\mu$m and are parallel and oriented with a small angle (generally less than 10°) with respect to the normal to the surface. They are operated by setting a high voltage, typically of 1 kV between its two surfaces. When an ion, an electron or an high-energy photon impinges on the MCPA surface, it generates a cascade of electrons that propagates through the channels and thus amplifies the original signal. At the end of the channels, where electrons exit, a Faraday cup allows to collect all the charges. In such a way, every channel acts as a continuous-dynode electron multiplier and, considering a couple of single MCP slab mounted in a chevron configuration, a very high gain up to 10^8 can be obtained, making this device capable to detect a single charge. Another peculiarity of these systems is the low dark count rate. Especially at low voltage 0.5-0.6 kV, which means gain up to 10^4, a dark rate lower that 100 mHz is possible [117] in small MCPA.

[8] Hamamatsu F1094

The two disks of the MCPA are interlaced with copper rings and connected to an external high voltage power supply. The MCPA readout is ensured by a copper receiver disk mounted into a Teflon cylinder. A sketch of the inner part of the chamber with the growth plate, the gas nozzle and the electrons' detectors is shown in figure 4.3.

4.1.3 Optics and laser apparatus

The optical part of the apparatus is necessary to generate electrons in the gold surface at the GP exploiting the photoelectric effect by means of high-energy UV pulses. UV photon are generated into a frequency-quadrupled Q-switched laser [9], which is shown in figure 4.2 on the right bottom part. Since the active medium of the laser is Nd^{3+}:YAG, the wavelength of the emitted radiation is fixed at λ_{UV} =266 nm. The duration of these pulses are ∼10 ns while the repetition rate can be varied from 100 mHz to 20 Hz. The energy of each pulse at the output of the laser is fixed at ∼2 mJ, but it can be varied inserting neutral density filters in the optical path. A sketch of the laser pulse coupling to the optical fiber is shown in figure 4.4. A short-focal quartz lens mounted on a dual-axis directional stage allows UV pulses to be focused at the entrance of the fiber which is positioned on a tri-axis stage. Particular care in the free-space to fiber coupling has been taken in order to avoid possible damage of the fiber. A vacuum feedthrough allows the 3-meter-long fused-silica optical fiber to enter in the cryostat chamber.

The energy of the pulses that enter into the optical fibre is measured with a removable bolometer [10] and usually the statistical average of the energy of 30 pulses is done. Also, a spurious reflection of the UV pulses is collected into a silicon photodiode (PD) [11] and it is used as a trigger signal for the measurements of charge extraction.

[9] Spectron Laser Q-switch system
[10] Thorlabs ES111C
[11] Thorlabs DET100A/M

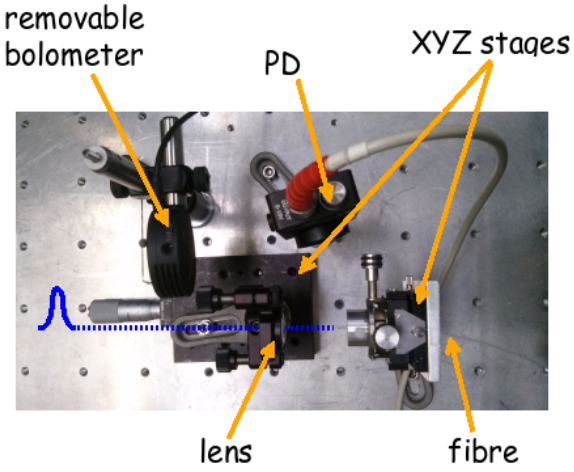

Figure 4.4: Photo of the optical part of the system where the UV pulses in air are coupled to the optical fiber.

4.2 Measurements and results

Before mounting each part in the vacuum chamber, everything was cleaned in an ultrasonic bath. Furthermore, once I obtained a vacuum level in the chamber of about 10^{-6} mbar, I closed the pneumatic gate valve and I filled the chamber with ∼200 mbar of neon. This gas was circulated between the chamber and the Oxysorb filter while externally the walls were baked at 340 K. I continued this procedure for several hours to reduce possible contamination in the chamber [156]. Before growing the crystal, the field-assisted gold photo-extraction process in vacuum was tested. As the quantum efficiency of the gold photo-extraction process is $\sim 10^{-5}$ [157] we can estimate a maximum number of $\sim 10^8$ electrons (~ 10 pC) generated by a 1 mJ energy laser pulse.

The charge signal collected at the CRD is picked-up at a capacitor (C) and then amplified using a low noise charge amplifier (CA) whose gain is 1.25 mV/fC and the decay time is $\sim 90\,\mu$s. The electrical scheme is shown in figure 4.5. The signal is displayed at an oscilloscope and acquired for off-line analysis for the reconstruction of the charge starting from the amplitude of the signal. The shape of the signal increases rapidly at the charge injection instant and then follows the CA decay

time as follows:

$$f(t) = y_0 + A \cdot \exp\left(-\frac{t}{90}\right) \tag{4.1}$$

where y_0 is the amplitude offset, A is the amplitude of the signal and t is the time in microseconds.

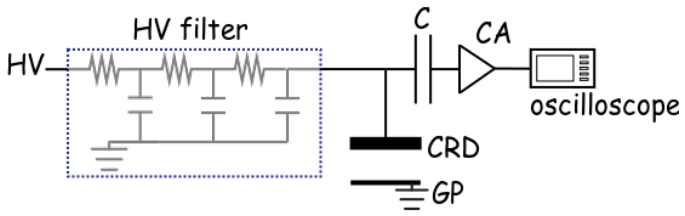

Figure 4.5: Scheme of the electrical part of the set-up. The high voltage (supply by a CAEN mod.N472) is filtered with a three stage π filter.

A first in-vacuum test regarding the behavior of the collected charge as a function of the electric field between the growth plate and the charge receiver disk ($E_{\mathrm{GP-CRD}}$) was done at a fixed laser pulse energy of $E_l = 1\,\mathrm{mJ}$. This measurement has been performed at room temperature and at a chamber pressure of $2{\cdot}10^{-7}$ mbar. Data are shown on the left side of figure 4.6.

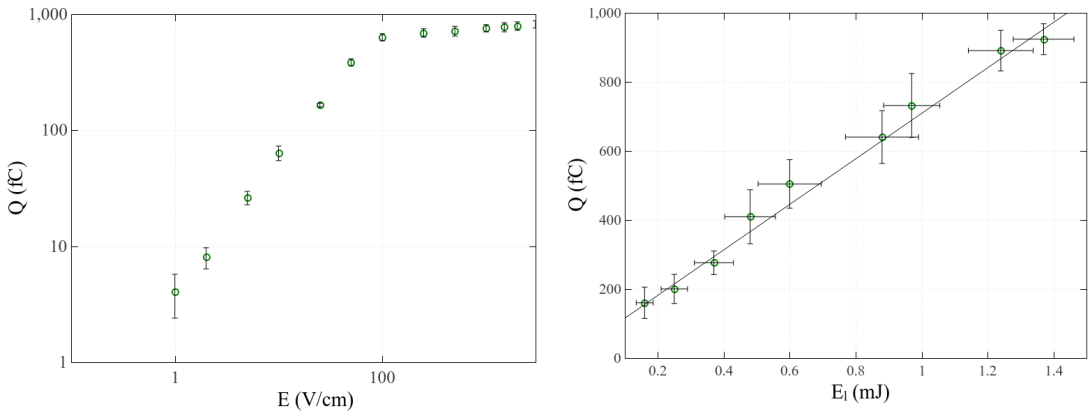

Figure 4.6: Left side: charge collected Q for several values of the electric field in vacuum. Error bars are comparable to the circles dimension. Right side: charge collected as a function of the laser pulse energy. Error bars are calculated starting from the standard deviation of the signal amplitude.

The observed trend is compatible with the results reported in the literature that have systematically investigated the in-vacuum electrons' extraction from different metallic photocathodes under laser irradiation [158]. In particular, the change in the slope that can be observed at $E_{\mathrm{GP-CRD}} \sim 100\,\mathrm{V/cm}$, can be explained in terms of space charge effects that take place within the extracted electrons bunches. The linearity of the measured charge as a function of the energy of the laser pulses E_l, for a fixed value of the electric field $E_{\mathrm{GP-CRD}} = 500\,\mathrm{V/cm}$, is shown in the right side of the figure 4.6. The constant term of the linear fit is $(30 \pm 25)\,\mathrm{fC}$ which is roughly compatible with zero as expected.

4.2.1 Crystal growing

Crystal growth occurs by spraying the purified gas on the GP cathode maintained at a fixed temperature of 9 K using the vapor deposition technique described in section 2.2. To ensure a high optical quality of the crystal, the deposition rate was kept at 0.2 l/min [159] and the pressure inside the vacuum chamber was $\sim 3 \cdot 10^{-5}\,\mathrm{mbar}$. After about three hours of deposition, the growth was stopped when the formed crystal layer was around 1 mm. The thickness is measured comparing

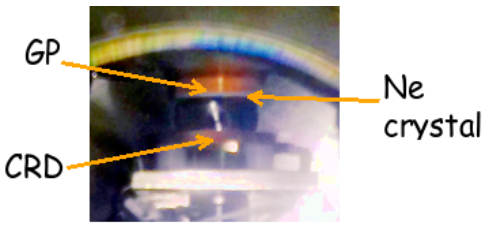

Figure 4.7: Picture of the Neon crystal taken by the back viewport of the chamber.

the crystal layer on the GP with lateral marks on the 70 K shield using the back viewport of the chamber. The uncertainty of this measure can be estimated in 200 μm. When the crystal is completely formed, the temperature of the growth plate was slowly cooled down to 4.2 K after a procedure of annealing for 1 hour at 15 K to rearrange the crystal structure. A low quality photo of the crystal is shown in figure 4.7.

4.2.2 Electrons extraction

When UV photons generated in the Q-switch laser system impinge on the gold foil at the center of the growth plate, electrons are created in the metal-crystal surface through the photoelectric effect in gold. Due to the presence of the electric field between growth plate and charge receiver $E_{\mathrm{GP-CRD}}$, electrons can drift within the matrix till they reach the neon-vacuum interface where they can finally be extracted and then be collected by the charge receiver disk. Figure 4.8 shows an

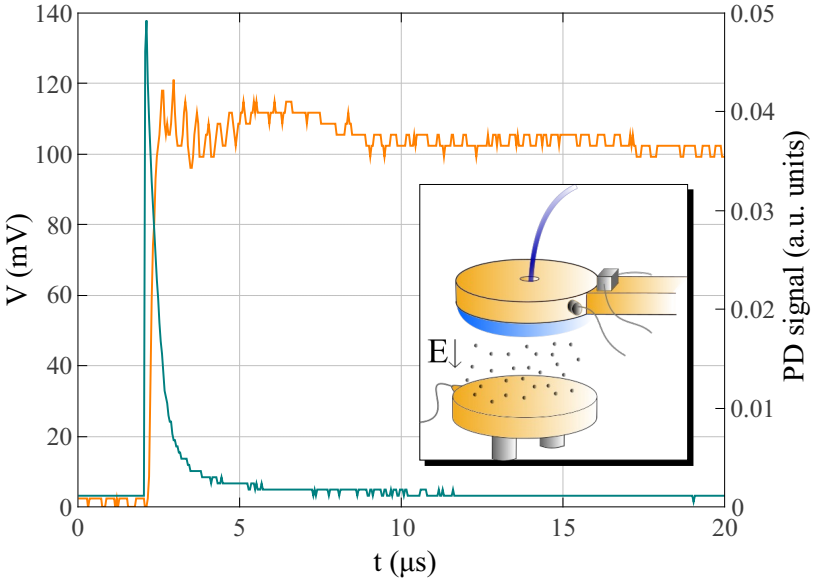

Figure 4.8: The solid orange line shows the charge signal collected at the CRD for electrons injected in a 1 mm thickness Ne crystal for $E_{\mathrm{GP-CRD}} = 1\mathrm{kV/cm}$ and E_l=1 mJ (left scale). Light blue line represents the optical trigger signal at the photodiode (right scale). The inset shows an illustration of the crystal, the CRD and the cloud of electrons.

example of the signal measured at the oscilloscope when $E_{\mathrm{GP-CRD}} = 1\,\mathrm{kV/cm}$ and the energy of the laser pulse is set to 1 mJ.

In the figure 4.8 the charge injection in the CA can be easily identified thanks to the laser trigger signal obtained at the silicon photodiode placed near the optical fiber entrance. Following equation 4.1 and using the gain of the CA, the charge at the CRD (Q) can be reconstructed. The charge collected as a function of the electric field for two different temperatures of the 1 mm-thick neon crystal is

shown in the figure 4.9. The error bars come from statistical analysis. Full charge collection is accomplished for applied electric field grater than 100 V/cm indeed, starting from this value the collected charge reaches a plateau. The different behavior of the 2 data sets in this figure at different temperatures could be explained considering a different coupling between fiber output and GP due to temperature changes.

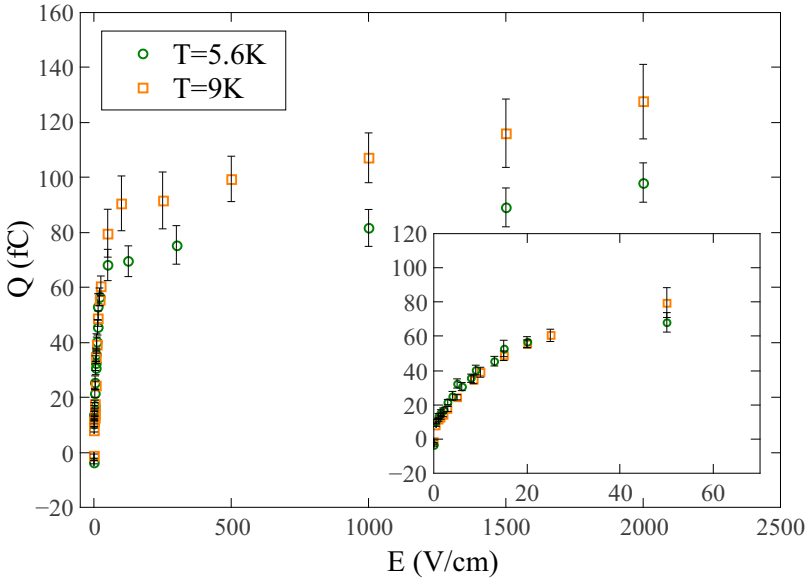

Figure 4.9: Charge extracted from the solid neon crystal and collected at the CRD as a function of the electric field. The inset shows a zoom of the first part of the curve. The two sets of data are taken at two different temperatures.

It is worth noting that the measured signals are real charge injections in the CRD and not spurious signals, due as instance to laser pulses that impinge on the CRD, because for a null electric field applied between GP and CRD, the charge collected is zero. Vice versa, if these signals were due to light, they would not present the electric field dependence which is instead shown in the figure 4.9.

4.2.3 Gas quality test

During the melting, I decided to proceed with a measurement of the purity of the neon used for the crystal growth exploiting a residual gas analyzer (RGA)

connected to the output of the turbopump. This system allows to identify atomic components in the gas till to a partial pressure of less than 10^{-11} mbar. I performed RGA analysis at different temperature monitoring the presence of neon, argon, nitrogen and water during the temperature rising. As can be seen in the plot of figure 4.10, at 27 K the unique component present in the spectrum is the neon which has a maximum at $\sim 1 \cdot 10^{-5}$ mbar over a background pressure of $\approx 9.5 \cdot 10^{-10}$ mbar. At higher temperatures (80 K) instead, small components of nitrogen and argon appear in the spectrum. The amount of these gases is however negligible with

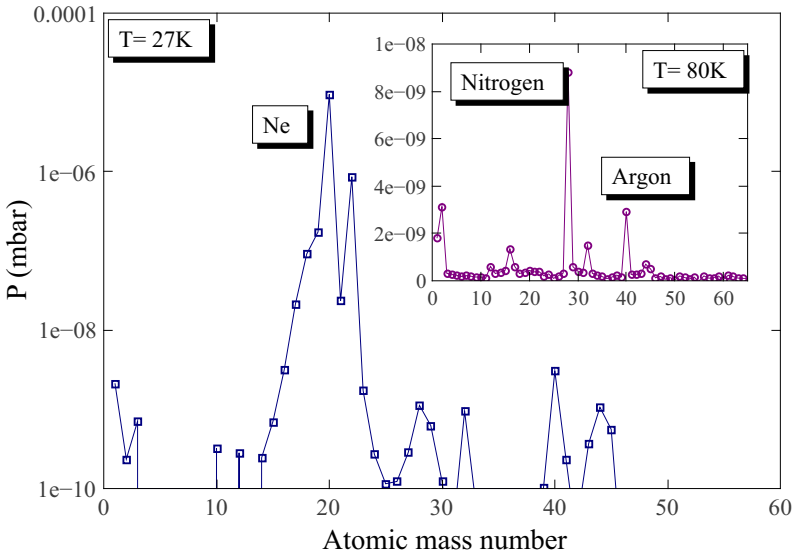

Figure 4.10: Residual gas analyzer spectrum. The pressure in the main plot is reported in logarithmic scale.

respect to the neon. This fact is supported by two reasons: first, the maximum partial pressure of background gases is 3 order of magnitude lower than neon, and second, a time integration of the single gas components from 20 K to 150 K shows that the impurity contents in the total gas used is lower than 1 ppm, which corresponds to the sensitivity of the instrument.

4.3 Discussion

The preliminary tests, performed without the crystal, guarantee that the developed electron-injector apparatus works properly. Furthermore, the crystal growing procedure allows to obtain a solid crystal of neon with a volume of about $0.5\,\mathrm{cm}^3$ and a good optical quality after a visual inspection. The signal shown in figure 4.8 allows to carry out another important consideration regarding the crystal quality itself: the amplitude of the signal in fact does not change during several hours of photoinjections in the crystal at 1 Hz repetition rate. This means that electrons can drift in the same condition of electric field and therefore no space-charge effect takes place in the solid. A high purity level and also a good quality of the crystal structure is thus ensured since impurities and imperfections in the lattice would act as charge attractors [89] immediately after the crystal growing. Reasonably, several hours of measurements can thus be considered a good compromise to test crystal quality at this level.

Similar measurements were also carried out using methane. The growing procedure adopted in this case was similar to the one in neon with the unique difference of the temperature. Methane in fact has a higher melting temperature of about 91 K, and thus the GP was maintained at $\sim$40 K during the growing, while the annealing process has been performed at 75 K. Electrons' extraction was found also in this case but the crystal quality obtained was worst than neon. During the visual inspection, this crystal in fact presents numerous opaque areas which corresponds to crackings and other defects sites.

It is also useful to note that the photoelectric effect when the gold surface is placed in contact with vacuum or crystal is different due to the different Fermi energy level at the interface in the two cases. Moreover, the number of electrons produced in neon is expected to be lower with respect to that in vacuum due to the differences in the interface that can contain impurities or defect sites that could quench the signal. Furthermore, the two measurements have been carried out at different experimental conditions of temperature and pressure so a direct comparison is not possible.

These measurements demonstrate that quasi-free electrons within the crystal can drift under an electric field toward the solid-vacuum interface. Here they can be extracted and, in neon, a value of $\sim$100 V/cm is sufficient to extract them with

a high efficiency. With such a measurement the possibility to efficiently extract free-charges from an RG crystal and detect them in vacuum has been verified.

During the development of the apparatus, as described above, I mounted also a MCPA. MCPA was placed next to the CRD in the mobile plate and in my intention it should act as detector for low numbers of electrons that can be injected in the crystal using low energy UV pulses. Unfortunately this device suffered the low temperature environment, and, although it was cooled only through radiation, it cracked and become unusable. A possible reason of the MCPA fault can be due to the ceramic composition of the slabs which is very sensitive to the temperature changes. Unfortunately, as far as I know MCPAs have never been used at low temperature and thus no comparison with literature can be done.

Chapter 5

Large RG crystals

In the previous chapter there is an experimental demonstration of the electrons' extraction from a ∼mm-thick layer of neon to the vacuum and their subsequent detection. Since the purpose of the project is related to the development of a particle detector for dark matter particles, the scalability in large dimensions of the RG crystals is the second stage that has to be demonstrated. A similar study concerning a solid xenon crystal for particle detection was done in 2010 by a group at the Fermilab National Accelerator Laboratory [160] in Batavia (USA). Similarly to this previous work, I also devised an apparatus for the growth of large specimens of rare gases and especially for xenon using the liquid freezing method. Considering the properties of RG as described in chapter 2, xenon has in fact the highest melting temperature, which is approximately 161 K. This means that the cryogenic part of the apparatus can be simple, since liquid nitrogen can be used for the cooling and other aspects can be better investigated.

This chapter contains a description of the experimental set-up based on the Bridgman-Stockbarger modified technique that has been used, of the recipe for crystal growing and a discussion of the results obtained using such xenon crystal as a detector for cosmic rays. The problems connected to the large crystal growing and the implication in the proposed detection scheme will also be discussed in

section 5.3. Furthermore, measurements about the estimation of the light yield of solid xenon at different temperatures will also be presented in section 5.4

5.1 Experimental apparatus

In section 2.2 we have seen that large single crystals of rare gases can be grown using the Bridgman-Stockbarger modified technique. I built an apparatus composed of a pyrex chamber, a cryogenic vessel and a feedback temperature controller which are necessary for the growth of large xenon crystals following this technique. A dedicated electronic chain and high voltage power supplies have also been developed. This apparatus exploits the same gas purification system used for the purification of neon previously described in subsection 4.1.1.

5.1.1 Pyrex chamber

Since pyrex is a very fragile material, especially when it is cooled at cryogenic temperatures, I adopted a custom-made chamber in which the junction between the glass and the stainless-steel flange is made of kovar. This metallic alloy ensures a good contact between the surfaces without outgassing and furthermore it has the same thermal expansion coefficient of pyrex making thus possible the cooling of the chamber without cracking. The pyrex chamber has a cylindrical shape with a semi-spherical bottom. The internal diameter is 63 mm, the total length is 120 mm and the pyrex thickness is 1.5 mm. The chamber is mounted on a DN 63CF stainless-steel flange which is connected to a 1.5-meter-long tube that exits from the LN_2 vessel and is connected to the gas purification system previously described in subsection 4.1.1. As shown in figure 5.1, also the vacuum system and the pressure meters are connected to the chamber.

The inner part of the pyrex chamber hosts the electrodes for the measurement of the electrons drift inside the xenon crystal. A dedicated mechanical structure, which is shown in figure 5.2, has been designed for this purpose. On the top flange of the chamber, three plastic (PEEK) columns hold the electrodes which are interlaced by small ceramic (macor) supports. The cathode is a 25 mm-diameter disk mounted at the bottom at a distance of 18 mm from the base of the chamber. Placed $\sim$18 mm above, the 25 mm-diameter anode is finally the last electrode. A

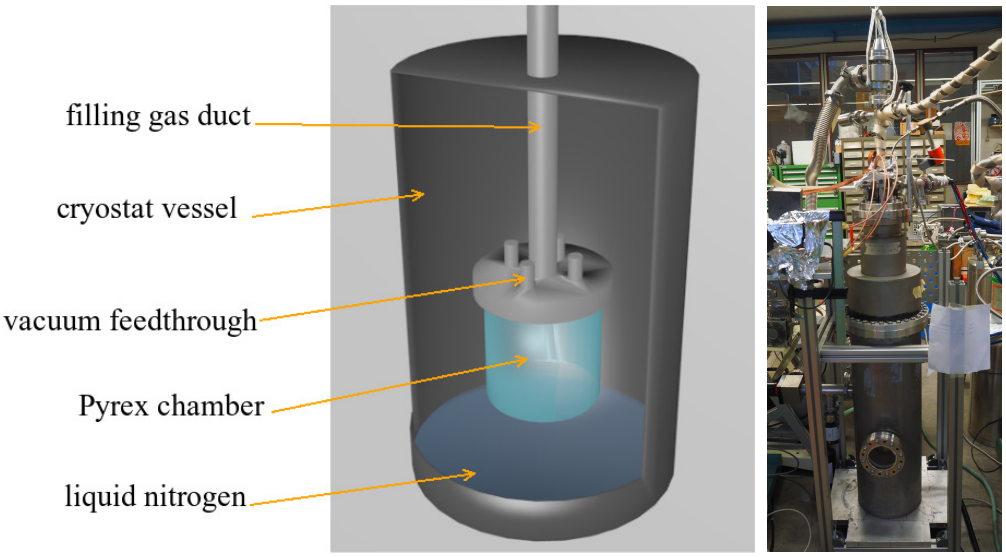

Figure 5.1: Sketch of the Pyrex chamber enclosed inside a large stainless-steel cryostat that contains also liquid nitrogen. The picture on the right shows the large vessel that contains liquid nitrogen and where the pyrex chamber can be inserted.

21 mm-inner-diameter guard-ring placed between them, ensures the homogeneity of the electric field. Finally, at a distance of 3 mm from the anode, I mounted a 97% transmittance copper grid. Anode and cathode delimit a drift volume of about 21 cm^3 while, given the chamber dimensions, the total available volume for the xenon growing is about 150 cm^3. The drift volume represent the active volume of the detector since only the events that happen inside this region can be measured. Three different high voltage power supplies provide the voltages, which are set as follow:

- anode potential: ground
- grid potential: $-520\,V$
- guard-ring potential: $-1000\,V$
- cathode potential: $-1500\,V$

In such a way the electric field in the drift region is $\sim 500\,V/cm$. A 2-dim simulation of the electric field strength is shown in figure 5.2, on the right.

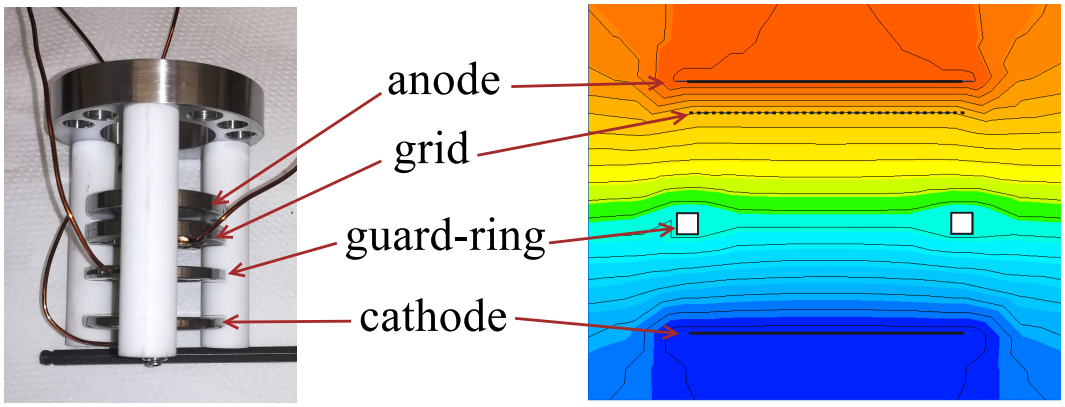

Figure 5.2: Left: picture of the inner part of the pyrex chamber with the macor holder for the electrodes. Right: simulation of the electric field inside the Pyrex chamber using QuickField program. Colors correspond to different electric field: blue stands for $\sim 0.5\,\mathrm{V/cm}$ while red for $1.6\,\mathrm{kV/cm}$. Equipotential lines are also shown.

The pyrex chamber was cleaned in an ultrasonic bath before the installation and was then baked at $40^\circ\,\mathrm{C}$ for few days in order to obtain a better cleaning. A vacuum level of $7{\cdot}10^{-7}\,\mathrm{mbar}$ was reached after three days of pumping with a turbo-molecular pump [1] connected at the entrance of a scroll pump [2].

5.1.2 Temperature controller

The pyrex chamber is surrounded by the vapor of liquid nitrogen (LN_2), which is contained into a large cryogenic vessel equipped with 2 optical ports in the correspondence of the pyrex chamber. The liquid nitrogen is continuously refilled into the vessel using a small copper duct and the distance between the bottom part of the pyrex chamber and the LN_2 is maintained at 4 cm. Due to the cryogenic vapor, the chamber's wall reaches a temperature of $\sim 90\,\mathrm{K}$.

The temperature gradient has to be set precisely along the direction of growing to obtain a good crystal. Since the pyrex thermal conductivity at 150 K is $\sim 1\,\mathrm{Wm^{-1}K^{-1}}$, I decided to fix the temperature T_{set} along the vertical direction of the chamber every 1 cm. For this reason, wire resistors with $R_{\mathrm{wire}} \sim 1\,\Omega$ are glued

[1] Turbo V-300 Varian
[2] nXDS15 Edwards

to the pyrex external wall at the desired point, as shown in the figure 5.3 on the left side. Next to each wire, a calibrated platinum resistive temperature sensor PT100 [3] measures the local temperature T_{act}. In total, I mounted four resistive wires and five temperature sensors. An electronic module that can be interfaced at the PC through an USB port was also developed to simultaneously measure the value of each temperature sensor. A picture of the electronic card is shown in figure 5.3 on the top-right side (b). Resistive wires are connected to different power supplies [4] that guarantee a maximum output of $V_{max} = 6\,\mathrm{V}$ and $I_{max} = 5\,\mathrm{A}$ and are also connected to the PC using a IEEE488-USB ports. A picture of these devices is shown in figure 5.3 on the bottom-right side (c).

The temperature along the pyrex chamber can be set and monitored through a custom Labview program specifically developed. This program is based on an active feedback system that exploits every temperature sensor and the associated resistive wire. The basic structure of this program involves one wire and the corresponding temperature sensor. The operation of a single module can be summarized in the following scheme:

1. the operator sets the output voltage of the power supply (this procedure will set the output power since the operation of a single module is in constant voltage mode);

2. the operator sets the desired temperature of the point T_{set};

3. the program acquires the actual temperature T_{act} of the point and operate a comparison with T_{set};

4. a loop cycle with an "if" condition operates in the following manner: if $T_{act} < T_{set}$ the maximum power is sent to the corresponding wire otherwise, if $T_{act} \geq T_{set}$ no voltage is applied;

5. the "STOP" button switch-off the cycle.

For simplicity reason the feedback systems of point number 4 work only in "ON-OFF" power mode without modulating the power sent to the wire. Relatively large temperature fluctuations ($\leq$1 K at 160 K) are thus present in this operational

[3] RS Pro
[4] Agilent E3631A

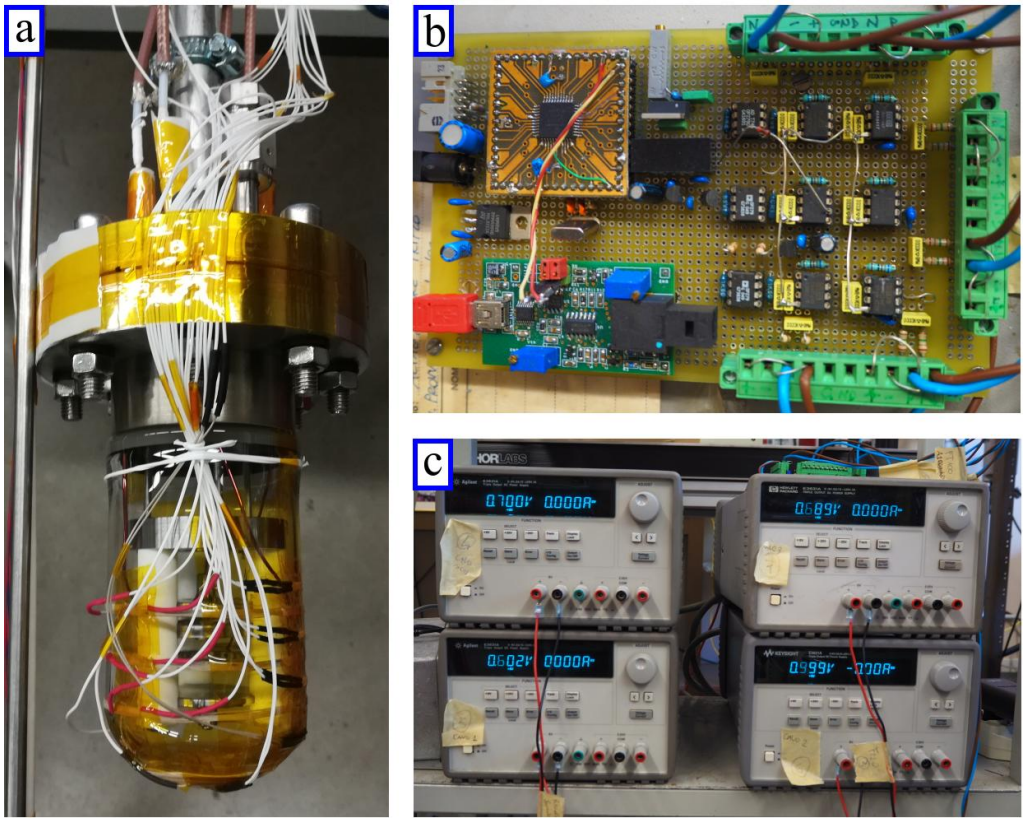

Figure 5.3: a) Pyrex chamber mounted on the CF63 flange. On the external wall we can see the cable connections with resistive wires (red sheath) and temperature sensors (black sheath). b) Electronic card; green terminal blocks are the connection for the five PT100 wires. c) Block of the four power supplies.

mode, since the maximum power is sent every time even if $T_{set} - T_{act}$ is very small. For a better stabilization of the temperature (0.1 K at 160 K) the operator can set opportunely the maximum power sent to the wire and thus a faster and more precise feedback with lower fluctuation can be realized. The scheme above described is replicated for each of the four module and thus a control of all the four wires is assured. With this system, an homogeneous temperature gradient along the direction of growing with a precision of 0.3 K can be obtained, which is sufficient to control the crystal growing.

5.2 Measurements and results

5.2.1 Crystal growth

In order to obtain a good optical quality and transparent solid [161, 162], the crystal growth was operated very slowly. Initially, the $\sim 150\,\mathrm{cm}^3$ chamber is filled with ~ 460 grams of liquid xenon at 163 K. The Xe was previously purified in the set-up described in section 2.2, which is composed of an Oxysorb filter and a hot getter. Following the Bridgman-Stockbarger growing method, a temperature gradient $\nabla T = 1\,\mathrm{K/cm}$ was applied at the Pyrex chamber along the vertical direction. Thus, the bottom of the chamber was initially at 161 K, which is sufficient to start the formation of a crystal seed. The process of crystal growth begin when the temperature gradient is progressively "moved" along vertical direction. Due to the relatively large dimensions of the chamber, the optimal velocity is $\approx 1\,\mathrm{K/hour}$. At this velocity the growing speed at the wall side is almost equal to the speed in the center and this ensures a flat growing surface. This velocity means that every one hour each set-point temperature (T_{set}) is lowered by 1 K. Under these conditions the solid xenon grows almost uniformly and homogeneously over the ~ 6 cm-diameter ~ 10 cm-long chamber.

Due to the slow growth rate, the temperature gradient requires fine adjustments that depend on the size of the crystal. In ideal conditions, the thickness of the solid xenon crystal (L) during the growth from the liquid phase can be estimated as [162]:

$$L = \sqrt{\frac{2K\Delta T}{H\rho}}\sqrt{t} \tag{5.1}$$

where t is the time, $H = 17.5\,\mathrm{J/g}$ is the latent heat of fusion for Xe, $K = 0.001\,\mathrm{W/(cm{\cdot}K)}$ is the thermal conductivity of solid xenon and ρ is the density. ΔT is the temperature difference between the bottom part and the top of the pyrex chamber. The entire process of filling the chamber with liquid and then crystal growing takes more than one day. The growing process ends when the liquid phase of the xenon is completely finished. When this condition occurs, usually the bottom part of the chamber is at 153 K.

Any substantial change of the temperature, such as for instance due to a quick shift of the liquid nitrogen level in the large vessel, produces different kind of optical

defects such as white structures or opaque stains. These solid imperfections are macroscopic volumes with a large number of voids and other kinds of defects and are generally classified as poly-crystalline regions.

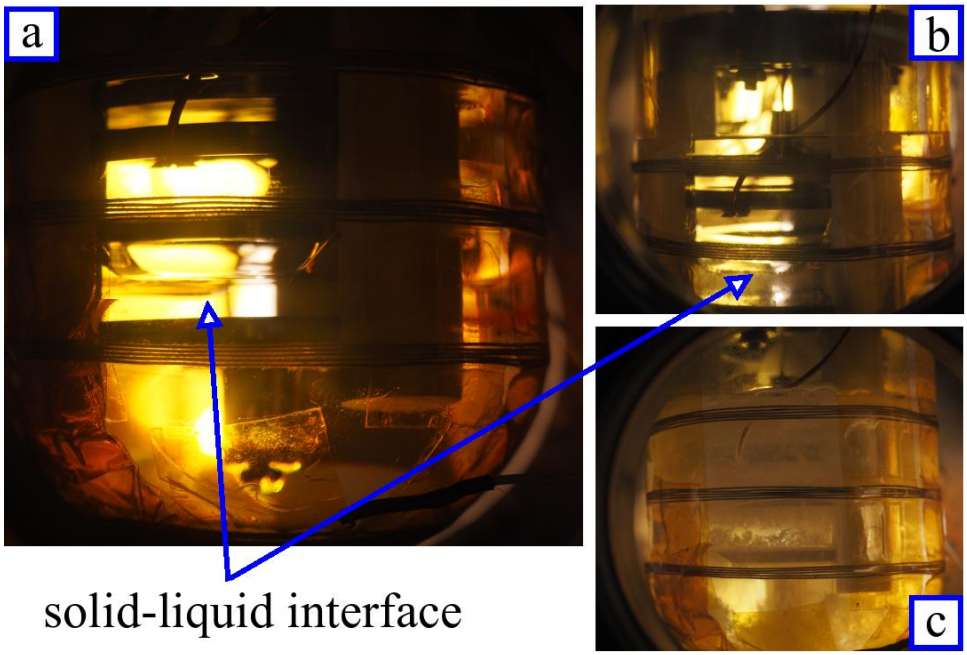

Figure 5.4: Pictures taken during crystal growing. a) represent a good crystal, in b) defects start to form while in c) a completely opaque crystal is shown.

Figure 5.4 shows three pictures taken during different crystal growing. Picture (a) is relative to a good test, in fact we can see in the bottom part a totally transparent xenon crystal and we can distinguish solid and liquid phase only for the change in the refractive index between them. Picture (b) instead shows a crystal with a discrete number of defects. This picture was taken after a too rapid decrease of the temperature of the pyrex chamber ($\sim$ 5K/30min) due to a wrong procedure in the refilling of LN_2 in the large vessel. Finally in picture (c) we can see a completely opaque crystal. In the last case, the very large amount of defects has completely destroyed the crystal structure.

5.2.2 Cosmic rays detection

Once the crystal is completely grown, it is kept at $\sim 153\,\mathrm{K}$ and the measurement can start. The active medium is the 25 mm-long, 20 mm-diameter portion of the crystal included between anode and cathode.

When comic rays pass through the xenon, they release energy by the mechanisms described in chapter 3. The most numerous charged particles at sea level are muons that are produced in the high atmosphere. Their overall angular distribution, with respect to the angle between the normal and the incoming direction (θ), is $\propto \cos^2\theta$ and the integral intensity of vertical muons above $1\,\mathrm{GeV/c}$ at sea level is $\approx 70\mathrm{m}^{-2}\mathrm{s}^{-1}\mathrm{sr}^{-1}$, which can be expressed as $\approx 1\,\mathrm{cm}^{-2}\mathrm{min}^{-1}$ for horizontal detectors [163]. Muons interaction with xenon leads in the ionization and in the subsequent production of free electrons into the crystal. A schematic view of this process can be seen in the figure 5.5. Due to the electric field, electrons can

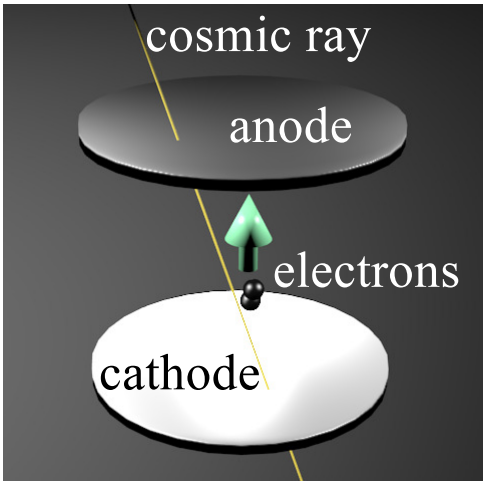

Figure 5.5: Schematic drawing of the cosmic rays detection process.

drift within the crystal and reach the anode, which is connected to a 1mV/fC gain charge amplifier (CA) with a time constant of $\sim 80\,\mu\mathrm{s}$. Also the grid is connected to a similar CA with a different time constant ($\sim 20\,\mu\mathrm{s}$) to discriminate possible fake signals. The output of the CAs have been read with an oscilloscope. Both the used CAs have been tested and calibrated before the operation by sending a known and fixed test pulse at their input channels. This procedure has been accomplished many times in order to acquire sufficient statistic necessary to calibrate the line.

An example of the charge measured is shown in the figure 5.6. The decay times of the CAs which are of the order of tens microseconds do not affect signal generation because the expected muon rate is much lower.

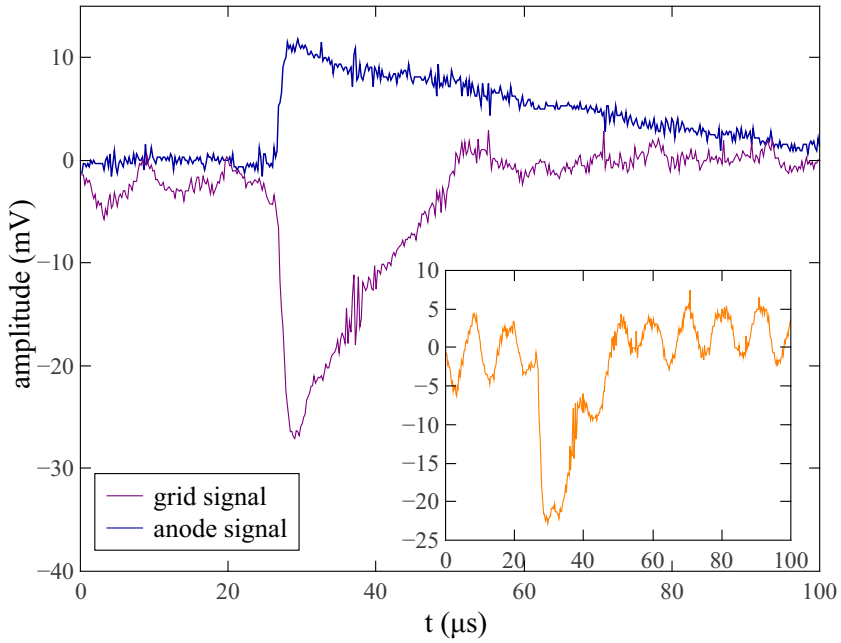

Figure 5.6: Example of the signals at the grid (violet) after data reconstruction and at the anode (blue). They have different shape because the different characteristic time of the CA used. In the inset the grid signal as measured before removing the low frequency modulation.

The amplitude of the CA output is proportional to the input charge through the gain coefficient and thus it is easy to reconstruct the charge produced in the crystal. The charge signal at the grid, as shown in the inset of figure 5.6, is quite noisy due to the different high-voltage-power-supply used for this channel. I operated an offline reconstruction of the signal removing the low frequency modulation as shown in the principal plot of the figure.

I acquired signals for about 30 minutes, collecting a total number of 115 events. Energy spectrum of these data is shown in figure 5.7. The energy spectrum is reconstructed using the anode signal amplitude, obtained as the value at the charge injection of the exponential decay function that fits the data.

Due to the length (l) of $\sim$18 mm of the active volume in the chamber, a mean

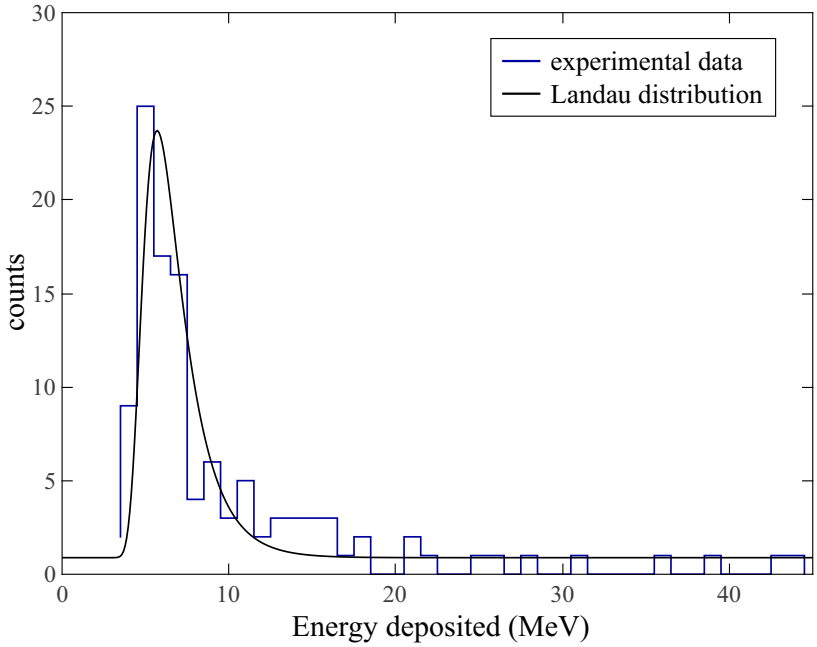

Figure 5.7: Energy spectrum of cosmic rays obtained from the signal obtain at the anode.

energy release of $\partial E/\partial x \cdot l \approx 6.6\,\text{MeV}$ is expected. Furthermore, the rate of incident cosmic muon is well established in literature [163]. The measured energy spectrum as a function of the energy (E) was in fact fitted with a Landau distribution ($\mathcal{L}$) whose analytic form is shown in equation 5.2:

$$\mathcal{L}(\beta) = \sqrt{\frac{e^{-\beta+e^{-\beta}}}{2\pi}} \tag{5.2}$$

where β is defined as:

$$\beta = R \cdot (E - E_P) \tag{5.3}$$

and R, E_P are a constant depending on the material and the most probable energy value, respectively . The reduced chi-squared is $\chi^2/\text{dof} = 2$, the maximum is of $6.3 \pm 0.2\,\text{MeV}$ and the measured rate of $3.8\,\text{events}/4.1\,\text{cm}^2\text{min} \approx 0.93\,\text{cm}^{-2}\text{min}^{-1}$ is very close to the expected rate. Good agreement can thus be found comparing measured and expected values.

5.3 Discussion

Many tests have been done in order to acquire the knowledge and the competences necessaries to grow a large solid crystal of xenon exploiting the Bridgman–Stockbarger modified technique. The crystal I grew is the largest single crystal of xenon reported in literature after a $\sim$1 kg solid xenon that has been grown in 2015 by a group in the Fermi National Laboratory in Chicago [162].

As already discussed in this thesis, thin crystals of RGs have been grown in the last years to study their physical and chemical properties. Unfortunately, only sporadic studies on crystals whose volume is larger than 10 cm^3 have been done in the past. A primary question was thus if large crystals of RG can be formed and if they could be used as particle detectors. A scalability study to test the feasibility to increase crystals' volume of about 2 order of magnitude starting from cm^3 to liters has been presented in this chapter discussing the developed set-up, the growing procedure and the recipe that has been followed. The scalability study confirms the possibility to obtain a very large (kg-scale) single crystal of rare gas. This material represents the starting point for a possible development of a particle detector based on rare gas solid crystal, as in the proposed schemes. The optimal agreement between experimental data and theoretical calculations such as in the measurement of the charge deposited in the crystal by cosmic muons, ensures the high quality of the crystal. Since the signal is constant for many hours, charge trapping can be considered negligible and consequently, impurity or cracking sites are roughly absent in the specimen. Using the crystal and the set-up based on copper electrodes, I was able to detect charge amount in the order of $\approx$ fC and thus tracking the cosmic rays interaction in the material. This is a first important test that gives a positive answer to the possibility of applying the proposed scheme in rare gas crystals in the field of particle detection.

Using the set-up described in section 5.1, I was not able to cool down the crystal at temperature lower than 153 K without cracking the crystal itself. A possible explanation of this difficulty, can be attributed to the slowness of the crystal lattice to rearrange itself after a temperature change even if the temperature is lowered very slowly. The thermal conductivity of liquid xenon is in fact very low and it is further lower in the solid phase (see the table 2.4) making extremely difficult the homogeneous cooling of the crystal, which is instead necessary to

avoid the formation of voids and fractures. These cracks make opaque and polycrystalline the solid and they can act as trapping sites for the charge motion and thus causing discharges when an intense electric field of ∼kV/cm is applied. Furthermore, the lattice parameter rearrangement passing from 160 K to 5 K is of the order of a few percent, since the measured density variation is of ∼10% [164]. The cooling tests that I performed were done lowering the temperature till 70 K at a velocity of approximately 0.5 K/h without any success to maintain a high optical quality crystal. A possible solution that can be adopted to cope with this problem is to grow crystals of more compact dimensions (∼ few cm^3) in order to allow a better homogeneity in the temperature profile within the solid. Another proposed solution can be to lower the temperature extremely slowly at a rate of 1 K/day [165]. Following these two suggestions, a new set-up for the growth of rare gas solids that avoids the formation of cracks and fractures is under development. This new system will have a volume of ∼ 10 cm^3 and it will be based on a pulse tube refrigerator that allows to keep the crystals at low temperature, much below the triple point. This will open the possibility to detect a very low amount of charge, smaller than ∼ 1 fC, thanks to the use of in-vacuum single-electron' detector.

I finally would to remark that the temperature, the pressure and their temporal variation are the only parameters that I can change during growing and the growing recipe is based on the modification of these quantities.

5.4 Light yield measuremnts

The measurements of the light yield (LY) in solid xenon at different temperatures has never been done and no data about temperature dependence of LY are present in literature. Since excitation mechanisms are strictly related to the ionization, the study of the light output from a xenon crystal is also important in order to have a more complete picture of the entire mechanisms involved in the proposed scheme. A different set-up, which includes a pulse tube refrigerator and a PMT with a high quantum efficiency in deep-UV was used for this measurement. The core of this experimental set-up is the cryostat chamber (XC) where the pure Xe is kept. It is a 12 mm-diameter and 26 mm-height stainless-steel cylinder covered with an un-coated fused-silica window which ensures light transmission of more than 80% between 170 nm and the near infrared. Into XC I also placed a hollow cylinder

of teflon smaller that the chamber. Its internal dimensions are 10 mm-diameter and 21 mm-height. The purpose of the teflon is to reflect towards the window the UV photons which are emitted in the direction of the chamber walls. It will thus increase and maximize the light output from the XC. Figure 5.8 shows a photo and a sketch of the XC which contains the teflon hollow cylinder.

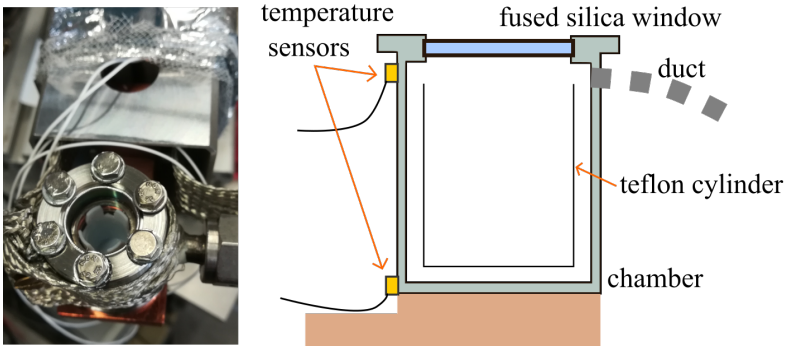

Figure 5.8: The picture on the left shows a photo of the XC mounted on the pulse tube refrigerator. The sketch on the right shows instead a schematic drawing of the XC, the internal teflon cylinder and the fused silica window.

The bottom of the XC is connected to the cold finger of the pulse tube refrigerator though oxygen-free, high-thermal-conductivity-copper bars which assure a good thermal connection and a reduction of the mechanical vibrations. Resistive heaters are placed next to the cold finger and they allow to precisely control the temperature of the XC, which is monitored with a calibrated silicon diode sensor in the bottom part and a platinum PT100 temperature sensor on the top of the chamber. The lower temperature that can be reached with this system is roughly 20 K. The XC and the pulse tube are shielded with a copper foil kept at ∼80 K surrounded by 3 foil of reflective aluminized Mylar, which prevent the radiation heating. The XC and the pulse tube refrigerator are placed into a vacuum chamber equipped also with optical ports and electrical feedthroughs. The chamber is connected through a 2 mm-diameter duct to one part of the purification system used also for other set-ups and described in subsection 4.1.1. As light detector, I used a photomultiplier tube [5] (PMT) with high quantum efficiency in the vacuum-ultraviolet (VUV), since the emission wavelength of xenon is ∼178 nm [166]. The

[5] Hamamatsu R2078

PMT is placed in front of the fused-silica window inside the vacuum chamber, because the air would completely absorb the 178 nm photons in less than 1 mm. The PMT can be removed from its position and an optical window for visual inspection can be installed in its place. A schematic view of the set-up is shown in the figure 5.9.

A cosmic rays detection module (SB) was also placed under the vacuum chamber verticaly aligned with the XC. This module is constituted by a plastic-scintillator bar coupled with a photomultiplier tube. The effective area of this system is $\approx 20 \times 20\,\mathrm{cm}^2$. Two low noise $0 - 100\,\mathrm{MHz}$ band amplifiers [6], whose gain is G_{amp}, are connected at the output of the PMT and at the SB. A $50\,\Omega$ terminated splitter, divides the xenon PMT signal into two channels, one is sent to a discriminator [7] and then to a coincidence module [8] (CM), while the other is filtered with a15 μs-integration unit and finally displayed at an oscilloscope for the acquisition. Signal coming from the SB is sent to a discriminator and then to the CM. Coincidence between the xenon PMT signal and the SB signal allows to identify and trigger only the interaction of cosmic rays in the xenon.

Since the energy deposited from a minimum ionizing particle in solid xenon is well known, I decided to use the light emitted consequently of the cosmic rays interaction in the crystal to estimate the light yield. The number of photons which impinges on the PMT is given by the following equation:

$$N_{ph} = \left(LY \cdot \frac{\partial E}{\partial x} \cdot \delta \right) \left(\frac{\partial \Omega}{\Omega} \cdot T \cdot \Gamma \right) \tag{5.4}$$

where the first factor between parentheses is the number of photons produced per incident energy in the material and is given by the multiplication of the light yield (LY) times the energy loss ($\partial E/\partial x$) in the medium of length δ. The second term between parentheses is instead the collection efficiency and is given by the solid angle ($\partial\Omega/\Omega$), the transmittance of the window (T) and the scattered reflection by teflon cylinder (Γ). The charge at the output of the PMT can thus be simply written as:

$$Q_{PMT} = e \cdot N_{ph} \cdot G_{PMT} \cdot \epsilon \tag{5.5}$$

[6] MiteQ AU1490
[7] Ortec 584
[8] Lecroy 365AL

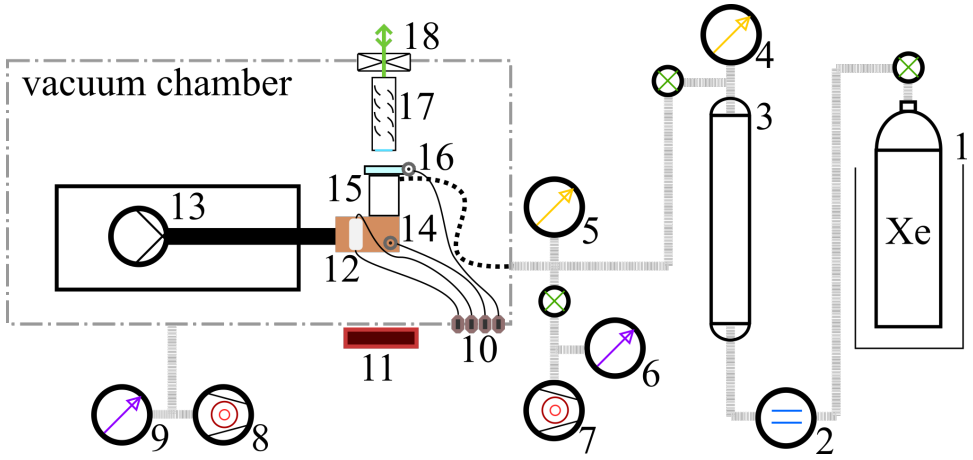

Figure 5.9: The picture shows a sketch of the apparatus used for the measure of the light yield in solid xenon. 1) Gas bottle and cryogenic vessel, 2) fluxmeter, 3)Oxysorb filter, 4-5)pressure gauges, 6-9)vacuum meters, 7-8)vacuum pump systems, 10)electrical feedthrough, 11)plastic scintillator for coincidence 12)heaters, 13)pulse tube refrigerator, 14)silicon diode sensor, 15)chamber and fused silica window, 16)Pt100 sensor, 17)PMT, 18)pneumatic gate.

where e is the electron charge while G_{PMT} and ϵ are the gain of the photomultiplier tube and the quantum efficiency, respectively. At λ =178 nm, $\epsilon = 0.1$. Since I operated the PMT at an high voltage of 1200 V, its gain is $2 \cdot 10^5$. On the other hand, the charge at the PMT can be estimated from the signal at the oscilloscope:

$$Q_{PMT} = \int i dt = \int \frac{V}{R \cdot G_{\text{amp}}} dt \tag{5.6}$$

where the current i is given by the voltage V divided by the 50Ω resistance and the amplifiers' gain G_{amp}. By a comparison between equation 5.5 and equation 5.6, light yield can in principle be estimated. However, since the geometric factor $\partial\Omega/\Omega$, the transmission T and the teflon multiplication factor Γ are not well known, only a relative yield between measurements done at different temperatures can be calculated. To overcome this issue, and estimate this unknown factors, I decided to use as calibration source the value of light yield for the xenon in the liquid phase. In the zero-field condition, these value is well measured and is (46 ± 5) ph/keV [167]. Following this procedure a roughly estimation of the absolute yield of Xe at different temperatures can be done.

Figure 5.10 shows an example of the spectrum of the charge at the PMT measured when the crystal is kept at 30 K.

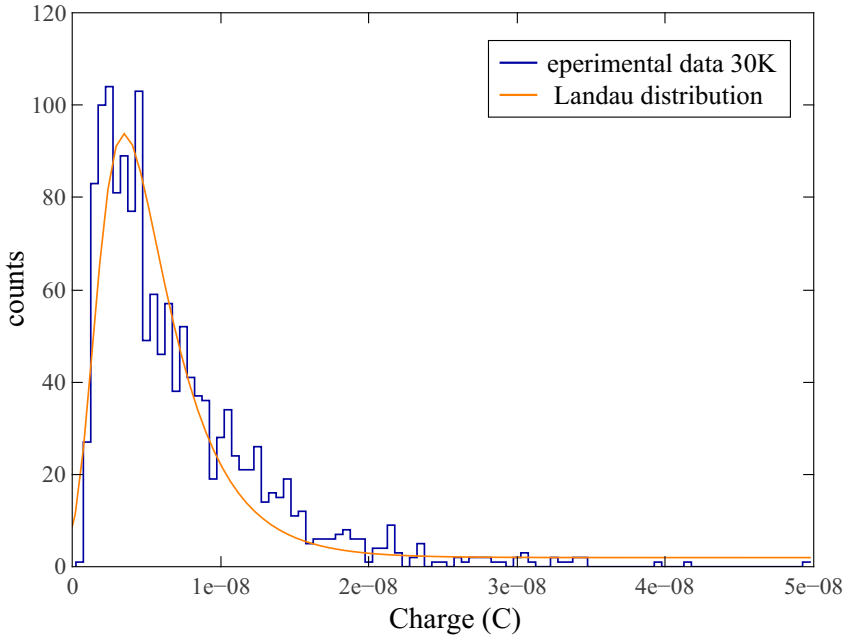

Figure 5.10: Hystogram of the charge measured at the PMT. This spectrum was obtained in the solid Xe crystal at 30 K. Orange curve is the fit of the data using a Landau distribution where the most probable value of the charge is $(3.49 \pm 0.09) \cdot 10^{-9}$ C. The uncertainty in in the charge estimation through the fit is thus $\sim 2.5\%$.

Since the trend of the data follows a Landau distribution (equation 5.2) I can estimate the most probable value of the charge and thus, using equation 5.5, the number of photons that impinges on the PMT. Equation 5.4 allows finally to obtain the light yield at this temperature since I calibrated the system using liquid xenon. Figure 5.11 shows the measured temperature dependence of the LY for xenon in the range $40 - 160$ K. The value at 163 K corresponds to the value of light yield of liquid xenon found in literature. Its error takes into account both the experimental uncertainty and the error reported in literature. The error in the value of liquid LY and in the most probable PMT charge given by the Landau distribution are the major contributions in the uncertainty estimation in the data shown in figure 5.11. The uncertainties in ϵ, G_{PMT} and in G_{amp} are instead negligible and thus they have not been taken into consideration. I would

like to note that, in this estimation of the LY, the refractive index of xenon at different temperatures has been considered constant, and also $\partial E/\partial x$ was fixed as a constant in temperature, since only sporadic and discordant values of these parameters have been found in literature.

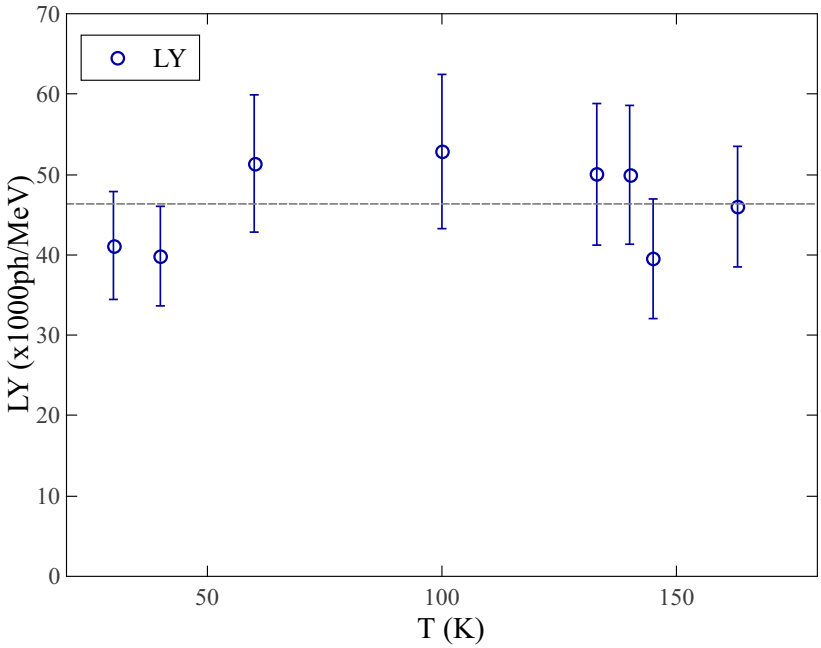

Figure 5.11: Temperature dependence of the light yield of solid and liquid xenon. Dotted line represents the mean value of the data.

As shown in figure 5.11 light yield values are roughly constant around a mean value (46 ± 7) ph/keV which corresponds approximately to the LY value in liquid Xe.

Chapter 6

Doped RG crystals

The measurements carried out in crystals of rare gases doped with alkali metals or rare earth atoms, exploiting the matrix isolation technique, are described in this chapter. For simplicity reasons, only neon and argon were used as matrices, and rubidium, samarium and neodymium were exploited as dopants. Since only few data regarding the physical behavior of these guest atoms in RG crystals have been found in literature, I decided to start the measurements from the basis and investigate these materials through optical spectroscopy both in emission and in absorption. It is indeed extremely important to understand the behavior of guests and hosts atoms in rare gas doped crystals. It is worth noting that the two important requirements necessary for the proposed detection scheme are: the narrow width of the lines and their long lifetime. Lines should in fact be narrower than the energy difference between the levels; and, in order to achieve high efficiency in the upconversion scheme, a long lifetime of the radiative emission is needed. Differently from an isolated atom, where these two requests are equivalent, in the case of an atom embedded into an interacting environment, a more complex behavior occurs. I started the investigation studying rare-earth (RE) doped systems and then I have also studied alkali doped RG crystals. These guest atoms are in fact usually characterized by narrow lines and long lifetimes.

The apparatus used for crystal growth through the vapor deposition method will be described in the first section where the optical part and the growing procedure will be also discussed. Then, the measurements carried out in these crystals will be described in section 6.2, and finally a brief discussion can be found in section 6.3.

6.1 Experimental apparatus

6.1.1 Growing chamber

The main part of the experimental apparatus is a six-hole cross stainless-steel chamber (SSC) that holds the pulse tube refrigerator (PTR) [1]. The cold finger of the PTR, that could reach a minimum temperature of 4 K, is placed in the middle of the chamber and at its center I mounted a 25 mm diameter sapphire window (SW) that holds the crystal and allows optical transmission measurements. Sapphire indeed has two suitable properties: one is the large optical transmittance from $\sim 200\,\text{nm}$ to about $5\,\mu\text{m}$ necessary to perform broadband spectroscopy. The other feature is the good thermal conductivity that sapphire has also at low temperature (at 10 K is $\approx 700\,\text{Wm}^{-1}\text{K}^{-1}$), which is not too far from the thermal conductivity of copper (at 10 K is $\approx 1100\,\text{Wm}^{-1}\text{K}^{-1}$). In correspondence of the SW, a quartz and a BK7 windows are mounted in the two ports of the SSC along the direction perpendicular to the surface of the SW. In the transverse axis, one port of the SSC is equipped with a manipulator, while the other is closed. Finally, the top hole of the SSC is directly attached to the external case of the PTR, while the bottom one is connected through a pressure gate to the vacuum pump system.

The SW temperature is measured with a Silicon diode [2], and its precise control is ensured using a 15 W heater placed in the cold finger. Exploiting the Joule effect, the power dissipated from the heater is $R \cdot i^2$ where basically R is the resistance of the heater and i is the current flow provided by a power supply [3]. By tuning the current flow, I can precisely set the power and thus the desired temperature can be easily obtained.

[1] Sumitomo RP062B
[2] Lakeshore DT670
[3] HP E 3632A Agilent

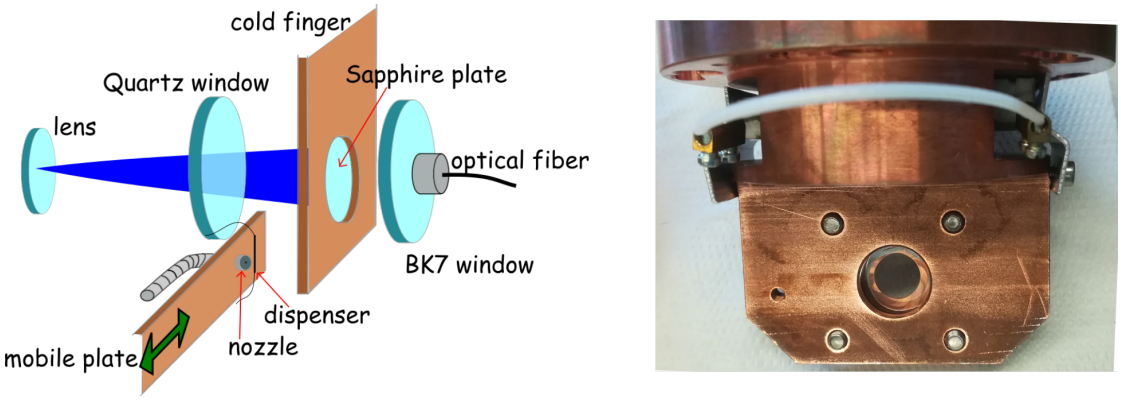

Figure 6.1: Left: a sketch of the cold finger with the sapphire window placed at its center. In front of the crystal there is the mobile plate with the gas nozzle and the doping dispenser. Right: photo of the cold finger with the sapphire window (SW) and the two heaters mounted laterally.

In the mechanical manipulator I placed both the gas nozzle for the gas spray and the alkali metal or rare-earth dispensers. These parts can be placed in front of the SW or 10 cm distant depending if the growth or the measurement is ongoing. In fact, once the crystal is grown, we can free the optical path by moving the manipulator backwards. A sketch and a picture of the apparatus described above are shown in the figure 6.1.

6.1.2 Optical setup

The broadest range for excitation was covered using different lasers systems which are tunable in the visible (VIS) and in the near-infrared (NIR) ranges. All these photons are delivered by a dye [4] or a titanium-sapphire (Ti:Sa) [5] laser. These systems are CW-single-mode lasers with a typical linewidth of $\sim$ GHz and both of them are pumped with a diode-pump-solid-state (DPSS) laser at 532 nm [6]. The output power ranges between 150 mW to 1 W depending on the wavelength.

To couple the light coming from the laser sources to the crystal, a 30 meter-long-multi-mode optical fiber, whose losses are lower than 10 dB/km, was used.

[4] Coherent 899 ring dye laser
[5] Avesta TIC laser
[6] Coherent Verdi

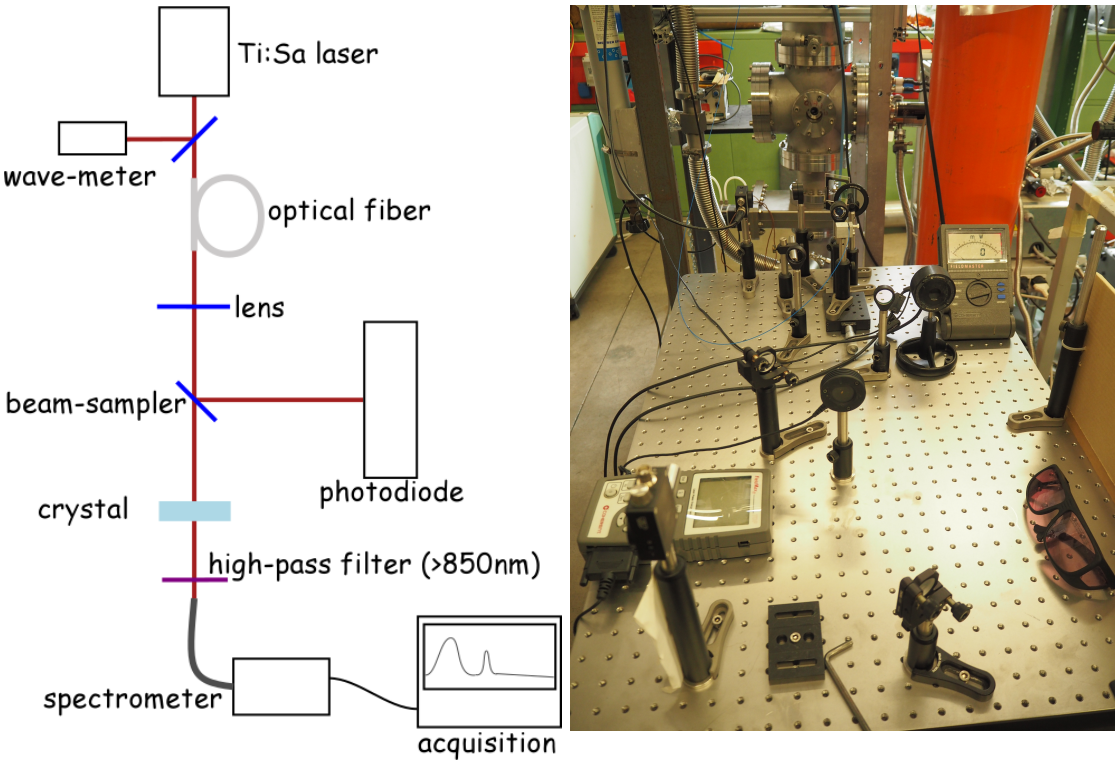

Figure 6.2: Drawing of the optical set-up used for the measurements of the doped crystals using the Ti:Sa laser system. Dye laser can replace the Ti:Sa. On the right side, a picture of the optical table behind the cryostat is shown.

The fiber output is focused onto the crystal using appropriate quartz lenses and, as shown in fig.6.2, a small fraction ($< 1\%$) of the beam is focused onto a silicon photodiode that acts as a laser system monitor. No control of the polarization was done after fiber output. Moreover, we can excite the crystal with a fixed-wavelength-laser at 447 nm. This is a laser diode whose bandwidth is about 1 nm, and its power can be as high as 2 W.

The detection system is based on different kinds of spectrometers and photodiodes. An UV spectrometer [7], two VIS spectrometers [8], and a NIR spectrometer [9] were in fact used. I also used both silicon (Si) and InGaAs photodiodes coupled with long-pass, short-pass or pass-band filters in different wavelength ranges. To

[7] Ocean Optics 200-850 nm
[8] Ocean Optics 350-1050 nm and Thorlabs 550-1050 nm
[9] Ocean Optics 950-1700 nm

minimize the background noise, the measurements were done in a dark environment.

Furthermore, the fourth harmonic at 266 nm of a Q-switched Nd^{3+}:YAG laser system [10] whose energy is ∼mJ and repetition rate 1 Hz, can be exploited to investigate the emission bands of the crystal. Through this system I can excite the matrices in the cryostat with high energy photons. These light-bunches reach the quartz window of the chamber through an air optical path without any optical fiber. In this set-up I used only two long focal length lenses and one silver coated UV mirror as shown in the photo of figure 6.2.

6.1.3 Crystal growing

Crystal growth occurs through spraying the purified gas onto the cold surface of the SW. The gas purification system, that allows an impurity level below ppb especially for high-electronegativity elements, is the one described in section 4.1.1. The rubidium [11], the neodymium [12] or the samarium [12] dispensers are connected through two vacuum-feedthroughs to a power supply that delivers up to 6 A necessary for heats the metals. Rb dispenser is a chromate mixture rod where Rb is deposited, while Nd and Sm are simple metallic wires cut from a large foil kept under argon atmosphere. The flow rate of the dopants versus the current in the dispenser is an empirical function provided by the manufacturer.

The growing parameters are the partial pressure of the gas and the dopant during the growing (P_g^{gas}, P_g^{dop}), the SW temperature (T_g) and the time (t_g) of growing. I initially grew a slab of pure rare gas of ∼100 μm-thickness and only after 30 min I activated also the doping dispenser. The gas flow rate is maintained about 1 mbar·l/s that leads in a pressure of growing of $P_g^{gas} \sim 5 \cdot 10^{-5}$ mbar (measured inside the cryostat chamber). The dispenser current is set to ∼ 3.5 A which gives a partial pressure of $P_g^{dop} \sim 5 \cdot 10^{-7}$ mbar. In this way, a crystal doped at few percent is progressively grown on the cold surface of the sapphire window. Finally, also the last 100 μm of the crystal are a deposition of only RG, indeed the dispenser current is set to zero ≈ 20 min before the end.

[10] Spectron Laser Q-Switch laser
[11] SAES Getter
[12] Goodfellow

6.2 Measurements and results

Rare gases neon and argon were used as matrices for the growth of doped crystals. In the following subsections the measurements carried out and the investigation of the light output of such crystals will be presented.

6.2.1 Rare-earths doping

Neon crystals

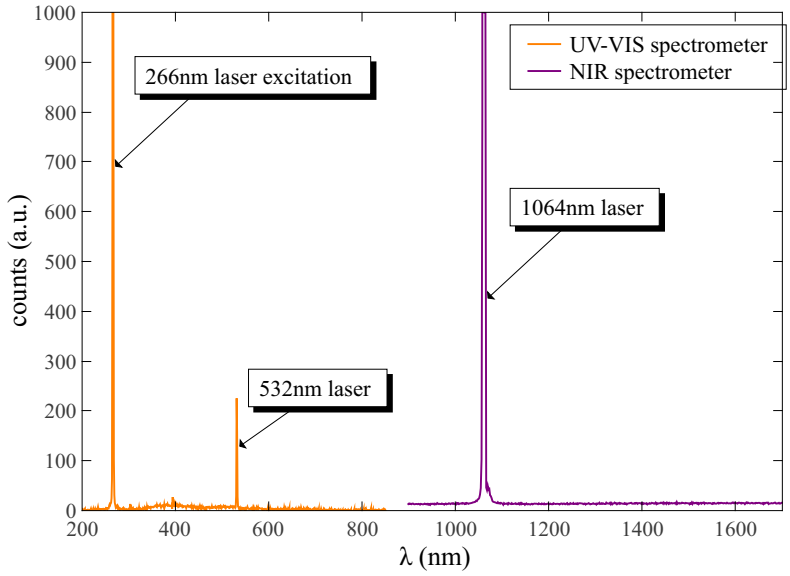

Figure 6.3: UV, VIS and NIR spectrum of a solid crystal of pure Neon under 266 nm excitation.

Neon (Ne) crystals have been grown both undoped (s-Ne) and doped with neodymium (s-Ne:Nd) or samarium (s-Ne:Sm). The starting material before the purification process is pure at 99.99990% (N6.0) and after the purification process we estimate impurities (especially for Oxygen) lower than ppb. Neon growth occurs at ∼9 K, while the measurements were carried out at $\sim 5\,K$.

The spectrum of a pure neon crystal (∼1.5 mm thickness) obtained under 266 nm excitation pulses is shown in figure 6.3. The three lines that can be see in the figure are the laser harmonic components at 1064 nm (fundamental), 532 nm

(second harmonic) and 266 nm (fourth harmonic), and no other lines are present. This means that pure Neon is totally transparent at the 4.66 eV (266 nm) photons as expected [168].

Neodymium doped Ne I grew a neon crystal doped with metallic neodymium (s-Ne:Nd) at $\sim 1\,\%$ of RE concentration. UV, VIS and NIR spectra are taken under UV excitation at 266 nm (pulses with energy in the mJ range). The data are shown in figure 6.4 on the left plot: a broadband emission centered at ≈ 500 nm with a width of ~ 100 nm has been measured.

Further investigation of the broadband emission has been done using a photomultiplier tube [13] coupled with two longpass optical filters [14]. Light signal at the PMT obtained when a 266 nm, 10 ns-pulse impinges on the crystal is shown in figure 6.4 on the right. As shown in the same plot, a fit using a negative exponential curve gives the lifetime of the broadband fluorescence signal: $\tau_{bb}(0.61 \pm 0.04)$s.

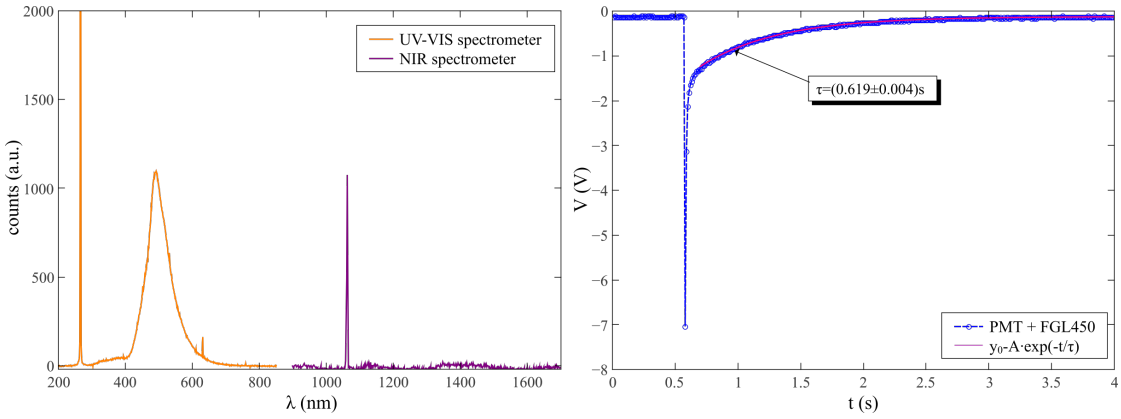

Figure 6.4: Left: UV, VIS and NIR spectrum of a solid crystal of Neon doped at % with Neodymium (s-Ne:Nd) under 266 nm excitation. Right: temporal evolution of the broadband fluorescence in s-Ne:Nd when pumped with 266 nm pulses at a repetition rate of 0.3 Hz.

Finally, I also record an absorption spectrum of s-Ne:Nd using an halogen lamp coupled with the UV-VIS and NIR spectrometer. Strangely, no absorption lines have been observed in any region, neither in the 500 nm band.

[13] R2248 Hamamatsu

[14] FEL400 and FGL435 thorlabs. Transmissions @ 500 nm are 86% and 90%, respectively.

Samarium doped Ne I also grew a crystal of neon doped with metallic samarium (s-Ne:Sm). The UV-VIS spectra recorded when 266 nm pulses impinge on the crystal is shown in figure 6.5. The same broadband emission centered at ∼500 nm, as in the s-Ne:Nd, has been found in this crystal. In the NIR range of the spectrum no emission has been recorded, thus the plot of figure 6.5 is truncated at ∼850 nm.

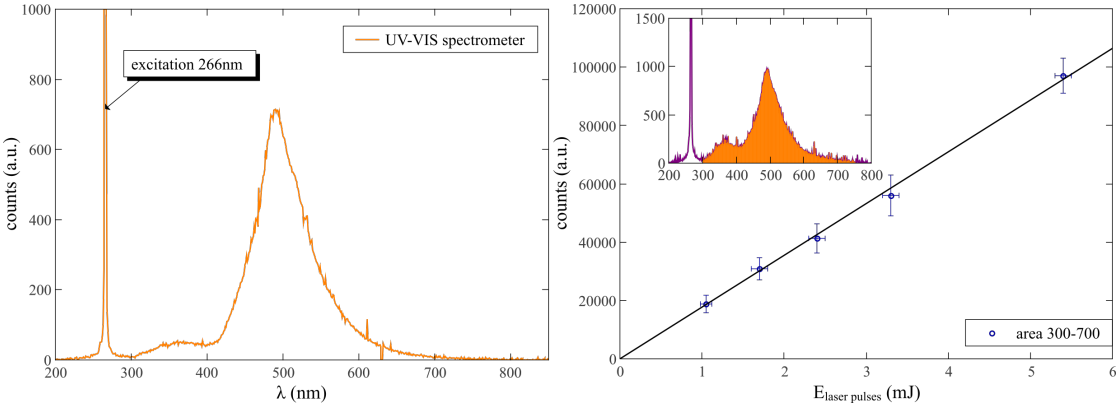

Figure 6.5: Left: UV-VIS spectrum of s-Ne:Sm when crystal is excited with 266 nm pulses. Right: experimental data and trend of the fluorescence emission 300 − 700 nm band of s-Ne:Sm as a function of the laser pulse energy. In the inset the integral used for the calculation.

A measurement of the linearity of the fluorescence band at 500 nm was also performed. As shown in the inset of figure 6.5, the spectrum signal is integrated in the range 300 − 700 nm for different energies of the excitation laser pulses from 1 to 5.5 mJ. A good linearity of the data was found.

Also in this s-Ne:Sm crystal, an absorption measurement in VIS-NIR bands was carried out, but also here no lines have been observed in the absorption spectrum.

Argon crystals

Argon (Ar) crystals have been grown both undoped (s-Ar) and doped with metallic samarium (s-Ar:Sm) following the procedure described in section 6.1.3. The melting point of Argon is at 83.8 K and this crystal has a face centered cubic stucture as previously described in chapter 2. During the growth, the temperature of the SW was maintained at ∼ 50 K and only after the growing it was lowered

slowly at $\sim 10\,\mathrm{K}$. Similarly to other RG pure crystals, also Ar is transparent to UV radiation.

Samarium doped Argon I grew samarium doped argon (s-Ar:Sm) crystal at few percent of concentration. UV-VIS and NIR spectra was recorded when crystals were excited with laser pulses at 266 nm. Figure 6.6 on the left shows the data obtained. In the visible band, the broadband emission $400-600\,\mathrm{nm}$ as in s-Ne:Nd and s-Ne:Sm is still present, but in this case the superposition of other lines is visible. These lines could be both absorption or emission structures. Moreover, in the NIR band, two lines centered at 970 nm and 1010 nm, respectively, can be observed. Probably these are samarium lines from the $4f^6(^7F)5d(^8H)6s$ to the ground state as calculated from the NIST energy levels of neutral Samarium [169].

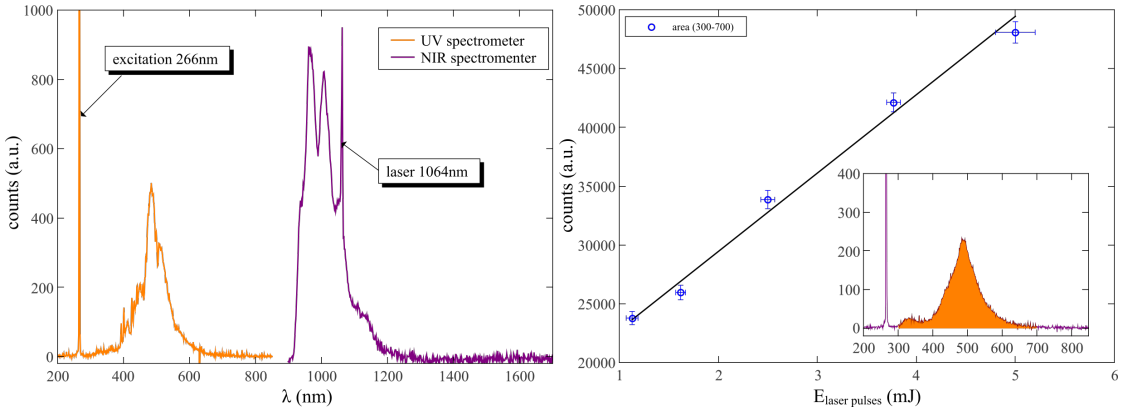

Figure 6.6: Left: UV-VIS and NIR spectra of a crystal of s-Ar:Sm excited with 266 nm pulses. Right: integral of the spectrum in the range [300-700] nm as a function of the pulse energy of the excitation at 266 nm. In the inset is shown the spectrum and the orange area is the integral value of spectrum for E_{laser} fixed.

I measured the lifetime of the broadband emission using a phomultiplier tube coupled with an optical longpass filter. In this case (s-Ar:Sm), $\tau_{bb} = (0.58 \pm 0.03)\,\mathrm{s}$, which is comparable with the lifetime of the broadband emission measured in s-Ne:Nd and s-Ne:Sm. Also an excitation with only the fundamental wave of the laser at 1064 nm (removing the 532 nm and 266 nm photons) was done in order to investigate possible multiphoton-absorption or direct excitation of the NIR bands. No emission lines were observed in the crystal when it is excited with 1064 nm

photons.

I also checked the linearity of the signal with respect to the energy of the 266 nm laser pulses. Figure 6.6 on the right side shows the area of the spectrum in the range $300 - 700$ nm (as shown in the inset of the figure) versus the energy of the laser pulses. Error bars in the energy are the statistical errors of a sample of 10 measurements of the energy pulses. A linear fit of the data is also reported and the χ^2/dof is $\sim$2 which means a good agreement of the fit with the data.

Finally, absorption spectrum using an halogen lamp was recorded in the UV-VIS and NIR bands. Data as a function of the temperature of the sapphire window are shown in figure 6.7 on the left side plot. The decrease of the signal for an increase of the temperature is due to the progressive reduction of the material which evaporates. Numerous absorption lines are present and the strongest are centered at: (423.3 ± 0.2) nm, (428.7 ± 0.2) nm, (435.5 ± 0.2) nm, (442.3 ± 0.2) nm, (460.8 ± 0.2) nm, (496.5 ± 0.2) nm, (503.2 ± 0.2) nm, (556.9 ± 0.2) nm and (630.9 ± 0.2) nm. The position of them is in agreement with lines observed in Sm according to NIST data [169, 170]. The comparison between the emission and the absorption spectrum is also shown in figure 6.7 on the right side. It seems that some lines can only be observed in emission (393 nm and 400 nm). These emission lines are however more energetic (shorter wavelength) than those in absorption. This probably means that the initial photon absorption was not from the ground state but from an excited level. In this way, the energy in excess is explained as the sum of the absorbed photon-energy and the energy of the initial level.

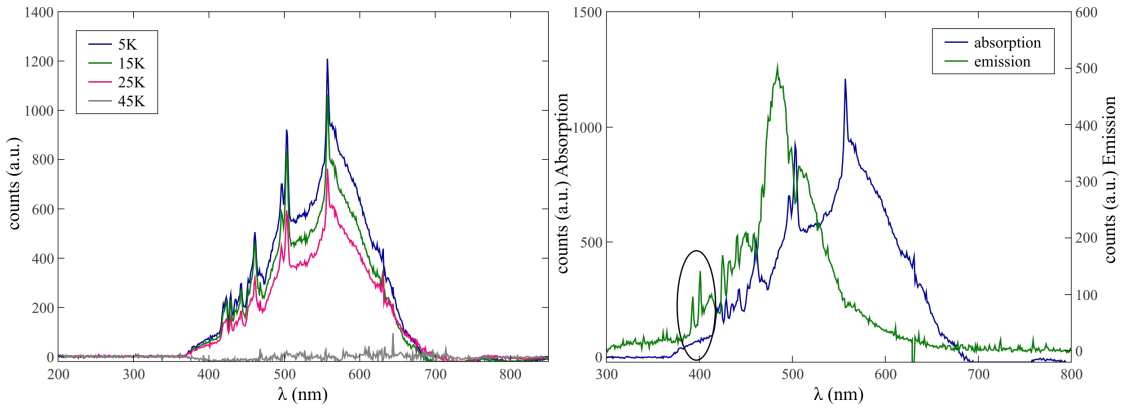

Figure 6.7: Left: absorption lines in s-Ar:Sm. Data was taken irradiating the crystal with an halogen lamp. Right: absorption and emission spectra of s-Ar:Sm.

6.2.2 Alkali doping

Rubidium doped argon Rubidium atoms are embedded into the argon crystal with a ratio between the two species of $\sim 1\%$. This value is calculated from the ratio of the different partial pressure in the chamber during the growth (P_g^{gas}/P_g^{dop}). The total thickness of the s-Ar:Rb film is about 1.5 mm at the end of the entire growing process. Growing occurs at ~ 50 K, while during measurements the temperature was lowered to $\sim$5 K. I carried out different spectroscopic measurements to investigate the behavior of the crystal obtained. Furthermore, three different samples were grown to check the reproducibility of crystals and measurements.

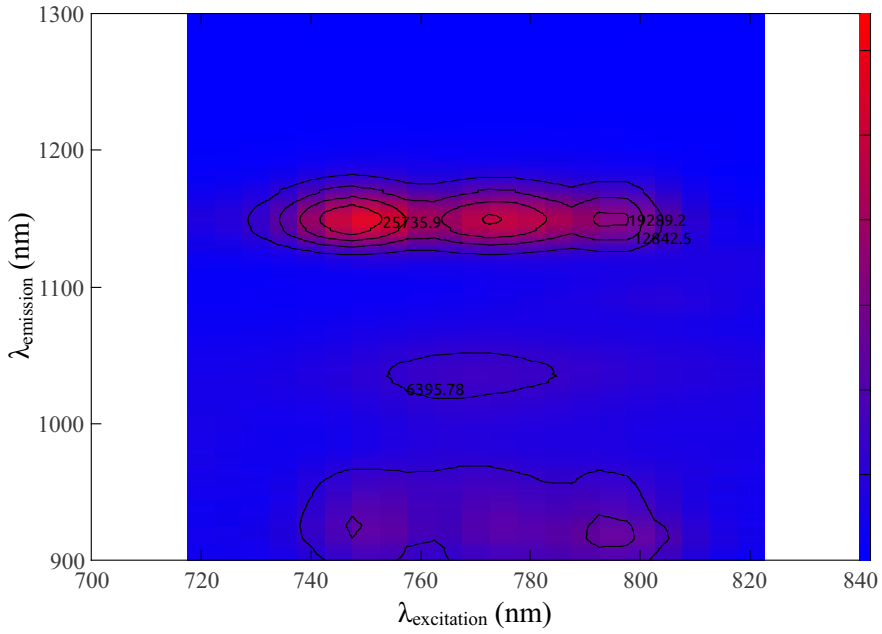

Figure 6.8: Two-dim spectrum of s-Ar:Rb crystal excited with a tunable Ti:Sa laser. The excitation wavelength (Ti:Sa laser) and the emission fluorescence are reported on the x-axis and on the y-axis, respectively. To avoid laser light directly into the spectrometer we used a 850 nm long-pass filter. The color scale is in counts from blue (low) to red (high). Some counts values are also shown in the figure.

I investigated the emission fluorescence ($\lambda_{emission}$) coming from the s-Ar:Rb crystal while it is maintained under a laser pump which was tuned from visible to near-IR. The excitation wavelength is indicated with $\lambda_{excitation}$. In the visible

excitation range, for $565\,\text{nm} < \lambda_{\text{excitation}} < 600\,\text{nm}$, no emission was found; instead scanning $\lambda_{\text{excitation}}$ between 718 nm to 822 nm I recorded the 2-dim emission spectrum which is shown in figure 6.8. The output power of the laser was maintained constant at $\sim 150\,\text{mW}$ in all the investigated range.

Figure 6.9 (a) shows a plot of the emission spectrum in the $900-1300\,\text{nm}$ NIR band of s-Ar:Rb crystal recorded for a fixed wavelength of excitation $\lambda_{\text{excitation}} = 770\,\text{nm}$. The results in plot of figure 6.9 (a) have been additionally fitted with four different independent Lorentzian curves ($L(\lambda)$), which are function of the wavelength:

$$L(\lambda) = y_0 + 2 \cdot \frac{A}{\pi} \frac{W}{4(\lambda - \lambda_c)^2 + W^2} \tag{6.1}$$

The free parameters of the curve are the area A, the central wavelength λ_c, the width W, and an offset y_0. The results of the fits are listed in the table 6.1 part (a) and are also shown in figure 6.9 superimposed to the experimental data.

peak	***A (a.u.)***	λ_c ***(nm)***	***W (nm)***
1 (a)	$(70\pm3)\cdot10^5$	927.4±0.3	71±10
2 (a)	$(56\pm5)\cdot10^5$	1034.9±0.3	92±4
3 (a)	$(151\pm3)\cdot10^5$	1154.8±0.2	39±10
4 (a)	$(79\pm4)\cdot10^2$	1624.7±0.4	37±2
1 (b)	939188±70	748.817±0.003	19.617±0.002
2 (b)	905510±85	770.018±0.005	23.213±0.002
3 (b)	255979±70	806.295±0.009	8.063±0.002
1 (c)	10028±60	748.01±0.01	21.34±0.08
2 (c)	14288±70	772.63±0.02	28.05±0.09
3 (c)	86233±50	798.022±0.008	15.28±0.06

Table 6.1: Peak parameters of the fits of figure 6.9 (a), (b), (c) using the fit function of equation 6.1.

From the table 6.1 part (a) it is clear that the largest peak is the third one which is centered at $\lambda_c \sim 1.15\,\mu\text{m}$. This peak has a width of $\approx 40\,\text{nm}$ which is in agreement with the linewidth measured in atoms embedded into solid matrices [114, 115, 113].

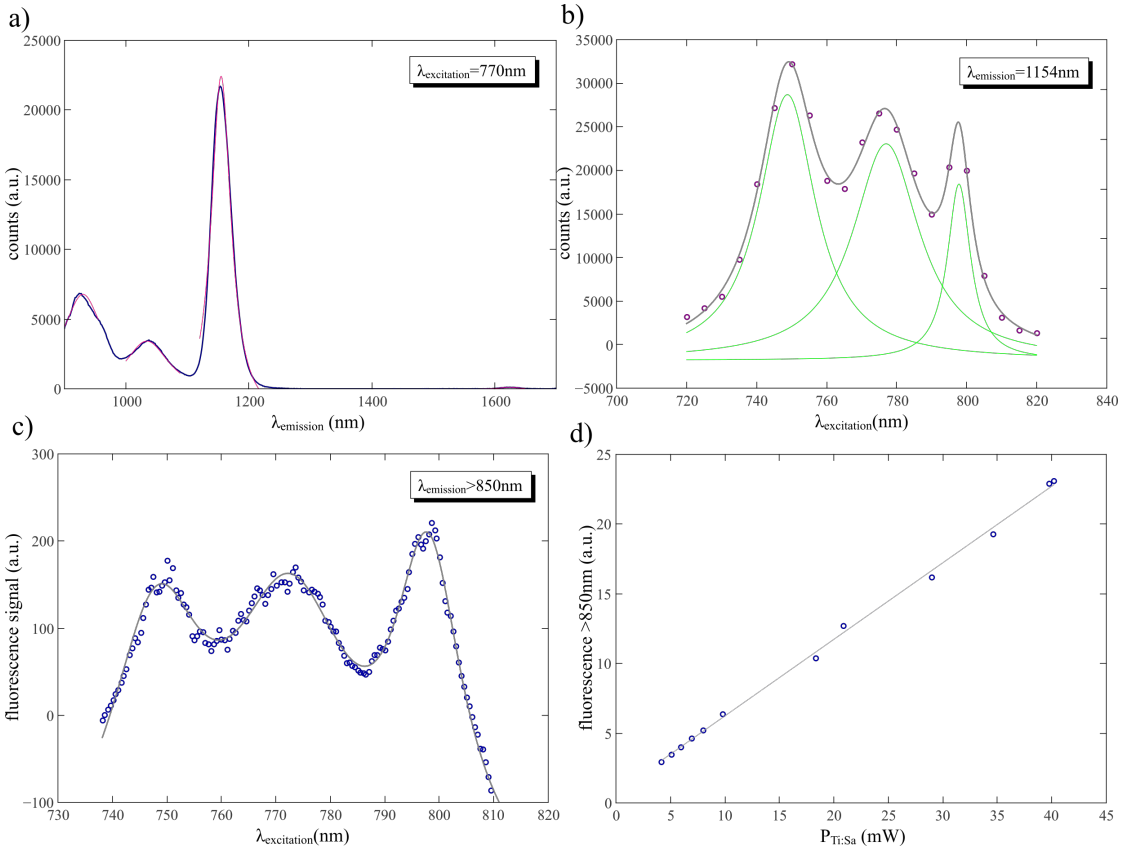

Figure 6.9: (a) Fluorescence spectrum of the s-Ar:Rb crystal excited at 770 nm. Blue line represents the experimental data, while pink curves are the Lorentzian fits. (b) Purple dots are the discrete spectrum of the s-Ar:Rb crystal obtained for variable excitation wavelength acquiring only emission at 1554 nm. Black line shows the sum of three Lorentzian fits which are singly shown in light green. (c) Spectrum of s-Ar:Rb obtained integrating the fluorescence for $\lambda_{\text{emission}} > 850$ nm and changing the excitation of the laser pump. Gray line shows the three Lorentzian fits obtained. (d) Intensity of the integrated fluorescence at $\lambda_{emission}$ >850 nm for different powers of the laser pump at $\lambda_{\text{excitation}} = 770$ nm. Error bars are comparable with dots' dimension. Gray line shows the linear ($f(P) = A \cdot P + B$) fit of the data. The constant term is compatible with zero as expected.

The plot reported in figure 6.9 (b) shows the spectrum at a fixed emission wavelength of $\lambda_{\text{emission}} = 1554$ nm for different excitation wavelength ($\lambda_{\text{excitation}}$)

from 720 nm to 820 nm. Furthermore, figure 6.9 (c) shows the emission fluorescence collected using a InGaAs cooled photodiode coupled with a long-pass filter [15], that integrates for $\lambda_{\text{emission}} > 850$ nm.

The data of the two spectra (b) and (c) of figure 6.9 have been fitted with the sum of three L(λ) (equation 6.1). In table 6.1 part (b) and (c), all the parameters of the curves are listed. I denoted with (b) the curve of plot (b) where $\lambda_{\text{emission}}$ is fixed at 1154 nm and with (c) the fit regarding the (c) plot where $\lambda_{\text{emission}} > 850$ nm.

The difference of the relative amplitude of the lines in the two plots (b) and (c) of figure 6.9 (that represent basically the same thing) depends on the different responsivity of the two detectors that were used for the measurements. In fact, in the case of the plot obtained for a fixed wavelength, I used an extended-silicon spectrometer, while in the other case an InGaAs photodiode with a long pass filter was used. Clearly, in the second case, the lines appear more broad because of the largest wavelength-band of integration of the fluorescence signal.

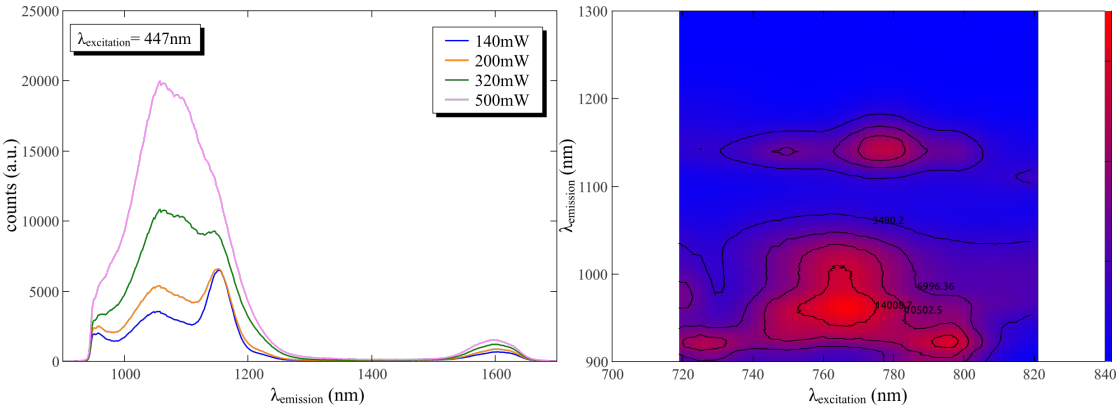

Figure 6.10: Left: emission spectrum of s-Ar:Rb crystal pumped with different power of the 447 nm laser pump. The blue curve is the first spectrum obtained pumping 140 mW for 1 min. The pink line is instead the spectrum obtained for 500 mW power for 1 min. Right: 2-dim spectrum of s-Ar:Rb crystal re-obtained using Ti:Sa laser after pumping the crystal for 5 min with 447 nm laser at 500 mW. The color scale is in counts from blue (low) to red (high). Some counts values are also shown.

Finally, I also measured the intensity of the fluorescence signal for $\lambda_{\text{emission}} >$

[15] FEL 850 thorlabs

850 nm with respect to the power of the pump laser at a fixed wavelength of $\lambda_{\text{excitation}} = 770\,\text{nm}$. A good linearity was found in the investigated power range between $\sim 5\,\text{mW}$ to $\sim 50\,\text{mW}$ as shown in figure 6.9 (d).

The crystal was also pumped with a laser diode at a fixed wavelength of 447 nm. The obtained spectra for different powers of the laser pump is shown in figure 6.10. For an increase of the power, the line at $\sim 1.05\mu$m increases more than the line at 1150 nm. At the power of 500 mW the spectrum (pink line in the plot) is dominated by a large broadband emission which is centred at about 1.1 μm. Furthermore, when we decrease the power, the spectrum that we measured again pumping with 770 nm is not the same as before the excitation with 447 nm. The new spectrum, obtained after pumping the crystal with 447 nm at 500 mW for 5 min is in fact shown in fig. 6.10 on the right side and it is quite different from fig. 6.8. For this reason, I believe that, pumping the crystal with 447 nm laser with a power grater than 150 mW, an irreversible modification in the crystal structure happens.

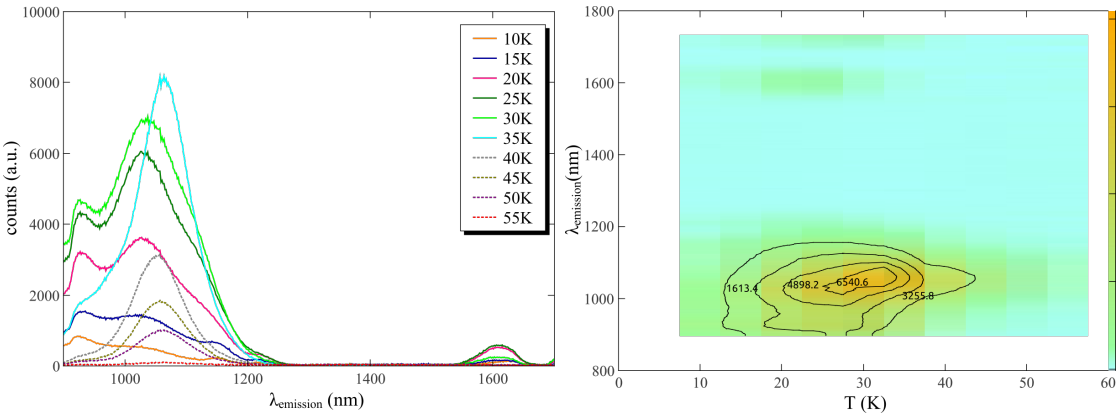

Figure 6.11: Left: various spectra obtained every 5 K while melting the crystals of s-Ar:Rb. The pump is the UV 447 nm laser diode. Right: 2-dim plot of the spectrum of s-Ar:Rb pumped at 447 nm for different temperatures.

The last measurement reported, was done during the melting of the crystal. I maintained the s-Ar:Rb under the 447 nm laser pump and I progressively increased the temperature. Different spectra were acquired every 5 K, between 10 K to 55 K. The experimental data are shown in figure 6.11 on the left side. A 2-dim plot with the emission wavelength versus the increasing temperature is shown in 6.11 on the right part. As shown in this plot, the maximum fluorescence signal corresponds to

a temperature of ∼35 K, and it is narrower than the broad emission measured at 10 K.

Rubidium doped neon Neon has a melting temperature lower than argon, indeed it solidifies at ∼ 22 K, as described in section 2.1. I grew rubidium doped neon crystals exploiting the vapor deposition technique as discussed in section 6.1.3. An optically transparent ∼ 1.5 mm layer of neon doped with rubidium at ∼ 1% was obtained (s-Ne:Rb). The fluorescence behavior of this crystal was investigated with a Ti:Sa laser and a dye laser systems.

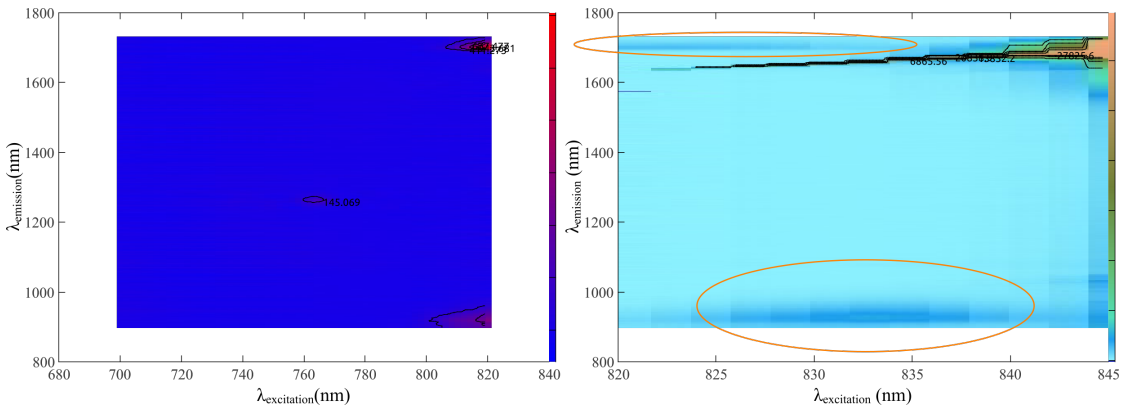

Figure 6.12: Left: 2 dimensional excitation-emission spectrum of a s-Ne:Rb crystal in the range 700 − 820 nm. Right: 2 dimensional excitation-emission spectrum in the region 820 − 845 nm. It is clearly visible the second order false signal due to the laser. The two circles underline the two peaks of emission.

A 2-dim fluorescence spectrum exciting the crystal with a tunable Ti:Sa laser between 700 nm and 845 nm was initially recorded. The acquisition was performed using the NIR spectrometer coupled with 2 long-pass filters [16], which are necessary to avoid second order false signals (See text). The obtained result is shown in figure 6.12 on the left part, while on the right part there is a zoom of this plot.

The major intensity was measured in an isolated peak whose emission wavelength is $\lambda_{\text{emission}} \sim 1270$ nm when the crystal was pumped at $\lambda_{\text{excitation}} \sim 765$ nm. The peak shape is shown in the 3-dim plot of figure 6.13 (a), and the two orthogonal sections at fixed $\lambda_{\text{emission}}$ and $\lambda_{\text{excitation}}$ are shown in the figure 6.13 (b) and (c),

[16] FEL850 and FGL850

respectively. A Lorentzian fit using the equation 6.1 was done for both of them and the results are listed in the table 6.2. Finally, the linearity of the fluorescence intensity in the band $1.24 - 1.3\,\mu$m was measured for different values of the power of the pump laser fixed at 765 nm, as shown in figure 6.13 (d).

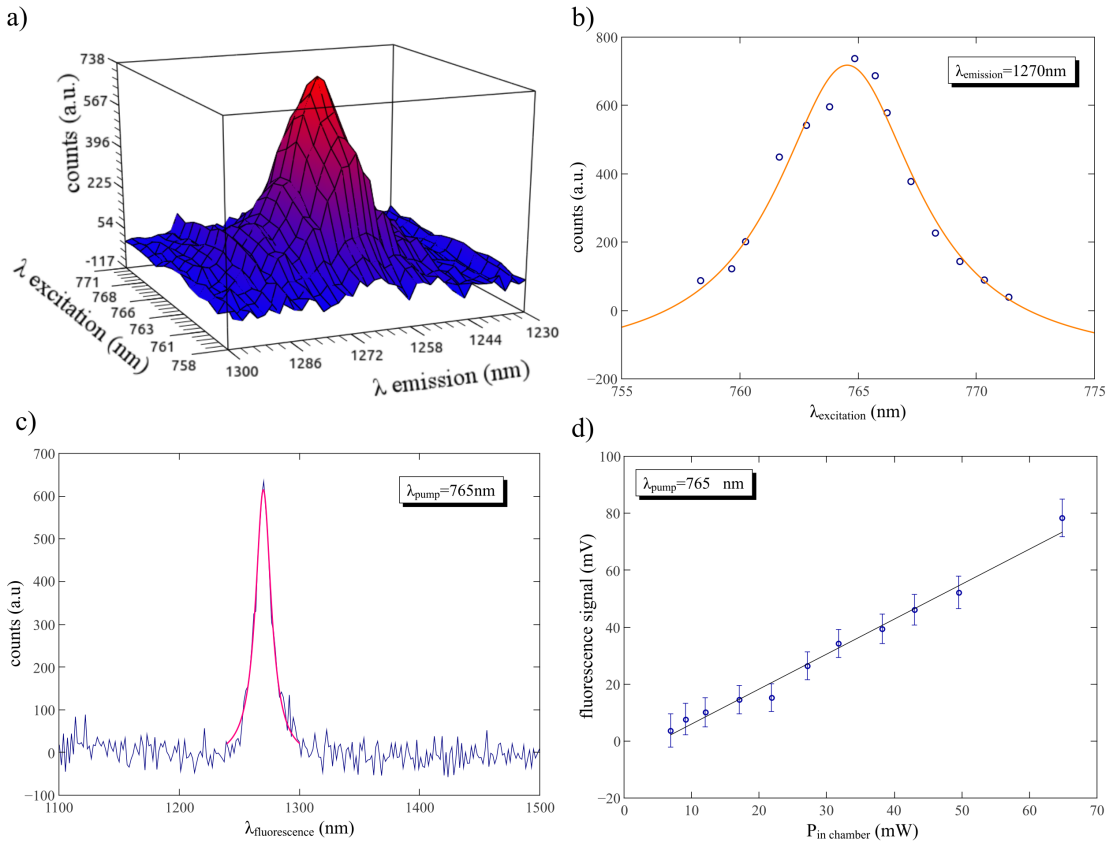

Figure 6.13: (a) 3-dim plot of emission-excitation of s-Ne:Rb in the region $758 < \lambda_{\text{excitation}} < 771$ nm, $1230 < \lambda_{\text{emission}} < 1300$ nm. (b) Blue dots show the spectrum of s-Ne:Rb crystal observing the light output at $\lambda_{emission}$=1270 nm as a function of the excitation wavelength. The orange curve is the Lorentzian $L(\lambda)$ fit of the data. (c) Blu line shows the emission spectrum of the s-Nd:Rb crystal pumped at 765 nm. Pink curve is the Lorentzian fit $L(\lambda)$ of the data. (d) Fluorescence signal integrated for $1200 < \lambda_{\text{emission}} < 1400$ nm as a function of the laser pump intensity between $\sim$ 10 and $\sim$ 70 mW with the linear fit superimposed. The excitation wavelength is fixed at 765 nm.

peak	*A (a.u.)*	λ_c *(nm)*	*W (nm)*
excitation	9900±100	764.5±0.1	7.2±0.9
emission	15700±800	1270.1±0.1	15.7±0.2

Table 6.2: Peak parameters of the fitted curve showed in figure 6.13 (b) and (c).

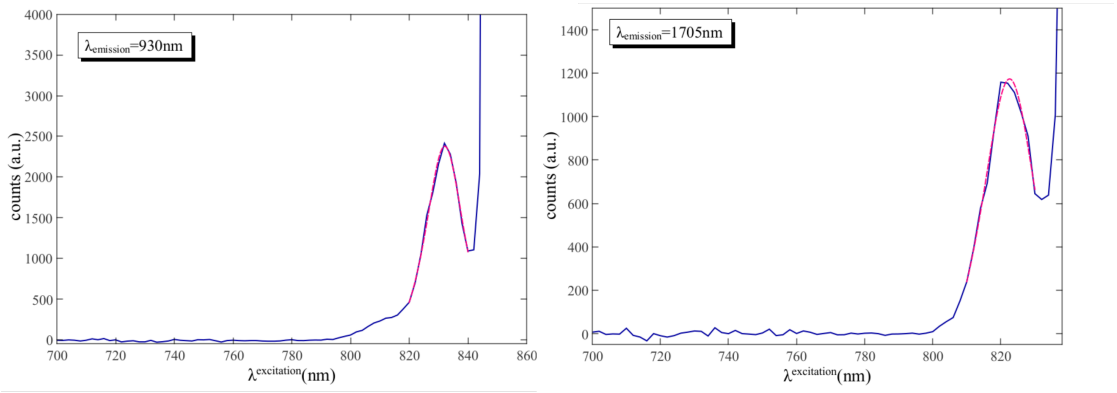

Figure 6.14: Left: spectrum of s-Ne:Rb at a fixed value of emission ($\lambda_{\text{emission}}$=930 nm) for increasing values of the excitation. The pink curve is the Lorentzian fit. On the right part the spectrum is saturated due to the tail of the laser light that passes through the long pass filters (FEL850). Right: spectrum of s-Ne:Rb at $\lambda_{\text{emission}}$=1705 nm for different values of laser pump excitation. The pink curve is the Lorentzian fit. On the right side the spectrum is saturated due to the diffraction at second order of the laser in the spectrometer grating.

The two emission lines that can be observed in the left plot of figure 6.12 at the right edge, one at short emission wavelength and the other at long emission wavelength, are best shown in the two dimensional spectrum on the right side of the same figure. The diagonal line that appears in the top-right part of the plot is due to the second order diffraction (SOD) of the laser in the spectrometer grating. This signal dominates the spectrum even though two long pass filters were inserted before the spectrometer input in order to reduce laser light. The two emission peaks, circled in figure 6.12, are best shown for a fixed emission wavelength ($\lambda_{\text{emission}}$ = 930 nm and $\lambda_{\text{emission}}$ = 1705 nm) in the figure 6.14 on the left and on the right side, respectively. The results of the Lorentzian fits using equation 6.1 are presented in the table 6.3. The peak at longest emission

wavelength is truncated because of the SOD, while the peak at shortest emission wavelength is also truncated in the right part due to the presence of the tail of the laser light that passes through the long pass filters and reaches the initial pixels of the spectrometer.

peak	*A (a.u.)*	λ_c *(nm)*	*W (nm)*
$\lambda_{\text{emission}} = 930\,\text{nm}$	84000 ± 1000	832.1 ± 0.1	18 ± 1
$\lambda_{\text{emission}} = 1705\,\text{nm}$	60000 ± 1000	822.6 ± 0.2	23 ± 3

Table 6.3: Peak parameters of the two Lorentian curves fitted on the figure 6.14.

The crystal was also pumped with a wavelength in the range $575 < \lambda_{\text{excitation}} < 605\,\text{nm}$ using a dye laser but no fluorescence was recorded in any range of the emission spectrum from 250 nm to 1.7 μm. Also pumping the crystal with 447 nm laser source did not produce any fluorescence output.

6.3 Discussion

Doped crystals are the active materials of the low-energy-scheme proposed. As discussed in chapter 3, the main characteristics necessary in the scheme, are: the narrow lines and the long lifetime of the metastable level. Levels should have in fact a linewidth narrower than the energy difference between the levels itself since only excited atoms could be ionized by the laser. Moreover, a long lifetime of the level is necessary to guarantee a high efficiency of the laser upconversion process which is indeed proportional to the lifetime.

The preliminary studies were focused on crystals doped with rare-earths and alkali atoms because in principle these two groups can satisfy both requests above discussed. In these tests the fundamental aspects and the behavior of such doped materials were studied to understand the applicability of the proposed detection scheme. In particular I developed a suitable set-up based on a pulse-tube refrigerator that allows to grow thin doped crystals using the vapor deposition technique. Using this apparatus combined with laser spectroscopic methods, I have investigated the optical properties of RE and alkali doped RG crystals, since their behavior was not well understood yet. So far in fact, only a few studies characterize these crystals [171, 114, 167], especially in the field of particle detection.

I have concentrated my research on mm-thick crystals, given the difficulty in the growth of this specimen with large dimensions. Furthermore, a recipe that allows to obtain reproducible specimens in terms of optical properties was defined. A precise set of parameters such as the temperature, the pressure of both gas and dopants in the chamber, the time of growing and the annealing process, define a recipe that guarantee the reproducibility of the specimen which is a critical aspect for the realization of the detector. Spectroscopic measurements have been in fact repeated several times to test if the measured values depends on the crystals or if they are spurious signals. The features reported in the previous sections have been found in every crystal analyzed. Furthermore, the laser probe, which has a beam waist smaller than the crystal, has been focused onto different parts of the specimen in order to test the homogeneity and uniformity of the matrices. Deviation in the measurements with imperfections lower than 1% in the signals have been found in every sample. This proves a good uniformity of all the matrices. The unique anomalous effect has been registered when laser is focused near the border of the crystals where diffraction, reflections and not controllable measurements can take place.

Regarding RG crystals doped with rare earth, interesting results have been obtained about the linewidth of some levels. In particular in the samarium doped argon matrix, as shown in figure 6.7, lines are sufficiently narrow as requested in the detection scheme. For example, the 7.2 pm-linewidth obtained in s-Ne:Rb crystal at $\sim$ 765 nm, could provide a sufficient narrow level necessary to probe an energy difference of 15 meV if used in a suitable scheme. Furthermore, a long fluorescence lifetime, which is useful for high efficiency schemes, has been measured in the 500 nm band as shown in figure 6.4. Unfortunately, the nature of this fluorescence has not been well understood.

Looking at the crystal during the measurements, I also noted the formation of a dark spot (non-emitting point) where the UV laser pulses impinge on the crystal. This spot appears after few minutes or irradiation with pulses at Hz repetition rate and energy above $\sim$1.5 mJ. When laser is switched off for some minutes, the spot disappears. This effect could be due to the formation of local defects, where the high energy pulses hit the crystal.

Interesting results have been obtained also in crystals doped with alkali, especially in terms of linewidth, as shown in figure 6.13 and in table 6.2. When alkali

atoms are embedded into solid state matrices such as RG crystals, the strong $S \rightarrow P$ transitions are shifted by the high sterical distorted lattice. Moreover, as recently reported in reference [113], it is expected that the atomic polarizability of RG atoms contributes most on the modification of the alkali spectrum as compared to the gas phase. In the measurements carried out in Rb doped crystals, a triplet state in the IR range, which was not expected, was also found. These lines could be due to the formation of alkali-RG-excimer states as a consequence of the laser irradiation of the crystal. Indeed, the formation of an alkali-RG-excimer state when these atoms are in the gas phase is reported in many studies in literature [172, 173, 174]. Comparing the lines experimentally found in the s-Ne:Rb, with that of these studies, some similarities in the position of the bands can be observed. In the gas phase, we can consider a pair of atoms or molecules in their ground state: R and N, if R absorbs energy to form R* which interacts with N, they can produce a stable excited state complex R-*-N where the excitation is shared between the components. This excited dimer, which is dissociated in its ground state, is called exciplex if R and N are different species, whereas if R and N are the same atom or molecule, the excited complex R-*-R is named excimer. The factors that contributes to the stability of this excited state complex can be easily understood considering the molecular orbital formalism. An electronically excited state * has a much stronger electron affinity and a much lower ionization potential than the ground state. Consequently, the half filled orbitals may participate in charge transfer interaction with other polar or polarizable species they encounter inter-molecularly. This energetic stabilization will in turn cause the R-*-N complex to have a longer lifetime that the corresponding R/N (ground state) complex. Considering R* and N, the major electronic interactions will involve their highest energy filled (HO) and lowest energy filled (LU) orbitals. According to the rules of perturbation theory, the HO of R will interact with the HO of N to yield new HO of the ground state of the exciplex and similarly for the LU orbitals. This new HO and LU of the excimer are split in energy with respect to the original HO and LU of R and N: one of the new HO and LU has a lower energy than the original and one has higher. Since one of the partners (R*) is electronically excited, three electrons are stabilized (two in the lower energy HO and one in the lower energy LU). Only one electron is destabilized (in the higher energy HO) as the electrons redistribute themselves from their original non-interacting orbitals to the new orbitals of the

exciplex. Thus a net gain is always achieved by the interaction of R^* and N. This naive view provides the remarkable conclusion that an electronically excited state has an inherent tendency to form a supra-molecular complex with other molecules or atoms and the only issue is the strength of the exciplex binding [175].

In the case of alkali-RG-excimer formation, as described in reference [176], transitions between the ground $^2S_{1/2}$, and the excited S and D states in alkali metals, which are forbidden in isolated atoms, become allowed-molecular-transitions when the alkali atom is very near to a noble-gas atom such as in high dense gas or in a crystal. The emission lines observed in the NIR band in the tests above described, can be due to the formation of alkali-RG exciplex states in the crystal, similarly to the excimer formation in the gas phase. Moreover, the temperature dependence of the s-Ar:Rb shown in figure 6.11 could be explained in terms of exciplex states formation. In fact, as described previously, the exciplex molecules cannot exist at temperatures above a certain value because of the major distance between atoms. As shown in the figure 6.11, there is a maximum in the emission at 35 K, while a further increase in the temperature leads in the loss of the signal. This could be a signature of excimer formation but clearly this is only a qualitative description and a more precise explanation is needed. This should take into account the temperature dependence of the atomic interaction potential which are not available. Unfortunately no studies have been found in literature that confirm or deny this hypothesis. Further investigations are thus necessary in this field.

Conclusions

The purpose of this thesis was to study the feasibility and the applicability of novel particle detection schemes based on rare gas crystals. These innovative approaches have been proposed as a new class of hybrid detectors characterized by a low-energy threshold and a low-background, necessary for the studies of feeble-interaction and ∼eV-energy-release events. Many physical issues are in fact nowadays present and, from the experimental point of view, they could be addressed exploiting innovative detection schemes. In particular, one of these challenging issues is the the lacking mass of the Universe, which is called dark matter and represents the largest part of the Universe mass. Many candidates, whose masses range from sub-eV to TeV, have been proposed in the last decades to solve this issue and many experimental works are currently ongoing in this field. The last generation of detectors employed in dark matter experiments are taking data nowadays, but unfortunately no direct-experimental evidences of DM existence have been found yet. For this reason, is important to improve the performances of the current detectors, looking for new sensors that should have a large volume and a low background level.

In the framework of two INFN projects (namely AXIOMA and DEMIURGOS), the group in which I'm involved in, proposed to investigate two different schemes that exploit rare gas crystals both pure and doped, combined with the in-vacuum single electron detection technology. These hybrid concepts could open the possibility to investigate DM candidates which can hardly be probed otherwise. In the first, less complex basic idea, the interaction of the particle in the pure crystal

will produce free electrons that can be extracted from the solid-vacuum interface and can be detected with appropriate charge sensors. In this case, a threshold of the order of $10 - 100\,\mathrm{eV}$ can be reached in kg-scale crystals. In the second, more sophisticated scheme with doped crystals, the idea is to exploit the internal energy levels of the dopant atoms embedded into the crystals. The incident particle is absorbed into a low-lying level which is then up-converted into the continuum using coherent radiation delivered by a pump laser. In such a way this low-lying state acts as an energy reservoir from where the laser-induced ionization takes place. Following this scheme, the absorption of the particle in the solid triggers the in-vacuum emission of an electron that can be detected using suitable sensors as in the first scheme.

Given the R&D nature of the project, in this thesis I studied the experimental features related to the schemes above described, which are crucial to develop solid RG particle detectors. In particular, the activities carried out during these years have concerned the following subjects:

- I developed many set-ups for the RG crystal growing exploiting different techniques, such as the vapor deposition and the liquid freezing. Cryogenic liquids and pulse tube refrigerators have been used for the cooling of the systems. In addition, I devised also recipes that guarantee the production of good quality crystals and their reproducibility in terms of optical parameters. Finally, I also implemented an apparatus for the purification of commercial rare gases which allows a final level of impurities in the ppb range.

- As concerns the electrons' extraction from the solid-vacuum interface in RG crystals, which is a key process in the proposed schemes, I performed studies in a solid neon crystal. For this investigation, I developed an apparatus that exploits the vapor deposition method and in addition I implemented a system for electrons' injection in the crystal based on the photoelectric effect in gold. In a few mm-thick crystal, I measured the electron extraction efficiency through the solid-vacuum interface as a function of the electric field applied to the crystal. More than the 90% of free electrons in the crystal can be extracted from the neon surface applying an electric field greater than $100\,\mathrm{V/cm}$.

- In order to test the feasibility of building a large detector, which is nec-

essary to maximize the particle interaction, I performed a scalability study regarding the growing of large RG crystals. In particular I grew a $\sim 150\,\mathrm{cm}^3$-volume specimen of pure xenon using the Bridgman-Stockbargher modified technique in a kovar-pyrex chamber. After many tests necessary to optimize the growing parameters, I obtained a crystal with a good optical quality which was used as detector for cosmic rays. In fact, using electrodes which were embedded into the crystal before the growing, I have measured the drift of electrons into the solid and the charge injection in the electronic system. Exploiting this apparatus, I was able to measure the interaction of cosmic muons in the crystal, which produces free charges that move within the solid under an electric field.

- Regarding the low-energy-threshold scheme proposed in doped crystals of rare gases, I performed preliminary studies in RG solids doped with alkali metals and rare-earth atoms. I implemented a suitable apparatus that exploits the matrix isolation method and thus allows to obtain doped crystals with a thickness of a few mm. Such a system is also equipped with optical viewports which are necessary to perform optical spectroscopy investigations. I grew many specimens with different doping concentrations in the range of few percent. I measured the energy position of optical transitions both in absorption and in emission, in neodymium, samarium and rubidium atoms embedded in RG matrices. I also measured the linewidth and the lifetime of these states under different experimental conditions.

All the measurements above described allow to give positive answers regarding the feasibility of the proposed schemes for a novel particle detection based on RG crystals and characterized by a low-energy threshold and a low-background. Possible applications are the detection of feeble interacting events such as dark matter researches or neutrinos investigations. Detailed studies, such as electrons extraction, large crystal growing and doping processes have been analyzed in depth showing how these phenomena could be exploited to develop the proposed particle detector. In this R&D phase, no showstopper regarding the physical mechanisms involved in the detection schemes has been found. The major difficulty in the experimental part of the projects occurred in the growth of very large RG crystals. This is probably due to the very low thermal conductivity and the large density

variation in temperature of the solid RG. To overcome this issue, among modified recipes in the growing procedure, several smaller samples of RG solids can be grown instead of a unique large crystal. Furthermore, other studies, especially regarding the low-energy detection idea in doped crystals, are necessary because the lack of knowledge of many processes in such environments. A better understanding of these systems, which is necessary to compute and simulate their behavior as particle detector, requires in fact a depth comprehension of some fundamental parameters such as the interaction potential between host-host and host-guest and the ionization potential of dopants in RG matrices. These features are in fact at the basis of the proposed scheme and must be known precisely before the application of doped matrices as particle detectors. Furthermore, the temperature dependence of charge transport properties in RG, the optical properties of RG matrices at low temperature and the effects of crystal defects and imperfection on electrical, mechanical and optical features of RG solids, are other characteristics that should be investigated in more detail.

The sensitivity of the proposed detection scheme is another important characteristics which is necessary to consider. This parameter is strictly related both to the electrons' detector efficiency and to the crystal features. In particular the limiting factor for the sensitivity is represented by the background noise. In the final detector, background signals are one of the major drawback and should be avoided or discriminated as much as possible. The dark count rate of electrons' detectors, which could be lower than $0.01\,\mathrm{Hz/mm^2}$ for single electron event, could be discriminated using a threshold of few electrons. On the other hand, cosmic rays interactions in the detector represent the largest source of false signals and they can only be diminished by placing the detector in underground laboratories where cosmic rays flux is smaller due to the large amount of rocks above the laboratory itself. As in other DM detectors, also muons veto systems can be installed in the proximity of the detector allowing thus the identification of muon interaction events. Another source of background can be related to the presence of radioactive isotopes such as potassium 40 which decays β or γ releasing $1.3\,\mathrm{MeV}$ or $1.5\,\mathrm{MeV}$, respectively. Usually, these events cannot be avoided and an inner volume, where the noise suppression is at a high level, can be identified. This region is commonly named fiducial volume with zero background and represents the active region of the detector. Moreover, regarding the approach in doped matrices, a possible

source of background noise can be the laser pump. In suitable materials, where non-resonant absorption can be neglected, laser absorption is triggered only when the first transition between 0 and 1 occurs and thus laser flux does not represent a limitation in this case. The validity of this behavior has been demonstrated in the so-called laser cooling of solids [177, 178], where, in proper conditions, tens of W/cm^2 of photons impinge on crystal and a cooling to cryogenic temperatures happen. Furthermore, due to the narrow linewidth of axions, the signal induced by these particle should be resonant with a precise value of the magnetic field and it could be thus identified from the white noise background as a sharp peak at a certain energy. All these phenomena should be investigated more in depth in order to estimate the real sensitivity of the detection schemes and compare it with the simulated one described in chapter 3. Anyhow, I believe that a working prototype of the detector can be thought and designed for a future application in particle physics.

Furthermore, I would like to remark that the studies that have been carried out regarding RG crystals, used as particle detectors, can be very useful also in other fields of researches. In particular, the study of the behavior of the rare gases in their solid phase can have applications in medicine, industry and fundamental-physics studies. As an example, these solids could be used for electric-dipole-moment (EDM) and charge-conjugation-parity (CP) violation experiments with hyper-polarized atoms. EDMs of fundamental particles, atoms and molecules are a class of experiments to constrain and potentially reveal new phenomena beyond SM, in fact, a non-zero EDM is a direct manifestation of time-reversal violation, and, equivalently, violation of the combined operation of charge-conjugation and parity inversion. Identifying new sources of CP violation can help to solve fundamental puzzles of the SM, as instance the observed matter-antimatter asymmetry in the Universe. The most precise EDM limit was measured in the diamagnetic mercury atom ^{199}Hg ($d_{Hg} < 3.1 \cdot 10^{-29}\, e{\cdot}cm$) [179]. In particular a strong scientific effort has been focused in the last decade through hyperpolarized noble gases, such as ^{129}Xe atoms, that can be used to search for EDM. In this view, to get more stringent limits, solid crystals of RG can be used to obtain high particle density ($10^{22}\, cm^{-3}$ which is 10^8 times higher with respect to gaseous ^{199}Hg) and a high maximum dielectric strength that could greatly improve the statistical sensitivity of the experiments. Another possible application can be instead in

positron-emission tomography (PET) detectors that are of paramount importance in nuclear medicine and in other human health applications. Many efforts are underway to obtain efficient PET detectors that could potentially localize with high precision cancer cells allowing therefore minimally invasive surgery. In this scenario, noble gas detectors can play an important role because of their good performance in terms of energy and spatial resolution. Furthermore, they can be scaled up to large volume as required in PET devices. Many efforts are nowadays directed to liquid Xe and Ar [180], but also solid RG crystals could be promising in PET system thanks to their strong scintillation and charge yield and to their high density. More compact systems with a high spatial resolution could be thus accomplished in solid RG crystals with respect to liquid detectors.

Finally, the study of the behavior of the dopant atoms embedded into RG matrices can provide important information regarding both the rare gases (as instance their polarizability) and the dopants themselves.

Chapter A

Channeltron tests

The detection of low-energy events following the proposed schemes, can only be accomplished using a set-up capable to detect, with high sensitivity, a small number of in-vacuum electrons. As already described in this thesis, the main requests of the electrons' detectors, are:

- high efficiency ("single electron" detection);
- low dark count;
- ultra-high-vacuum grade;
- compact system;

Channel electron multipliers (channeltrons) [181] could be a good choice, and furthermore they can be "easily" bought. In addition to these sensors, I also designed an electrostatic lens that focuses charges into the channeltron itself. In this appendix I will describe the development and the tests of this integrated system made of a commercial channeltron and an homemade electrostatic lens.

A.1 Channeltron

Electron multipliers have been used in the last 50 years as an important electrons-ions and photons detectors in many applications as for instance in mass spectrometers and in magnetic-sector instruments. They are basically of two types: discrete-dynode multipliers [182], that derive from the photomultiplier technology and include for example the copper-berylium dynode, and the continuous-dynode multipliers [183]. Examples of the latter are the channel electron multipliers (CEM) also named channeltron and the microchannel plates already described in chapter 4 which are a series of many CEM of μm dimensions. A CEM is basically a channel of few mm-inner diameter made of a specially formulated lead-silicate glass that exhibits the properties of electrical conductivity and high secondary emission [184].

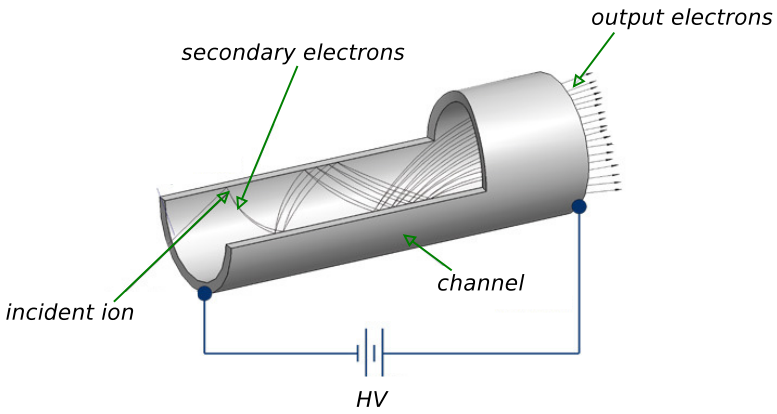

Figure A.1: Schematic view of a channeltron detector.

In figure A.1 is shown the basic operation of the channeltron. When the charge particle (electron or ion) strikes the wall in the beginning of the inner part of the channel (cathode), two-three secondary electrons are then typically produced. These e^- are accelerated down the channel by a positive voltage bias and strike again the channel walls producing more additional electrons. At the output of the channel (anode) a pulse of $10^5 - 10^8$ electrons emerges depending on the voltage difference (ΔV) applied between the cathode and anode. A Faraday cup is finally

coupled to collect electrons. As shown in figure A.2, the gain depends on the applied ΔV that ranges from 1500 V to 3000 V.

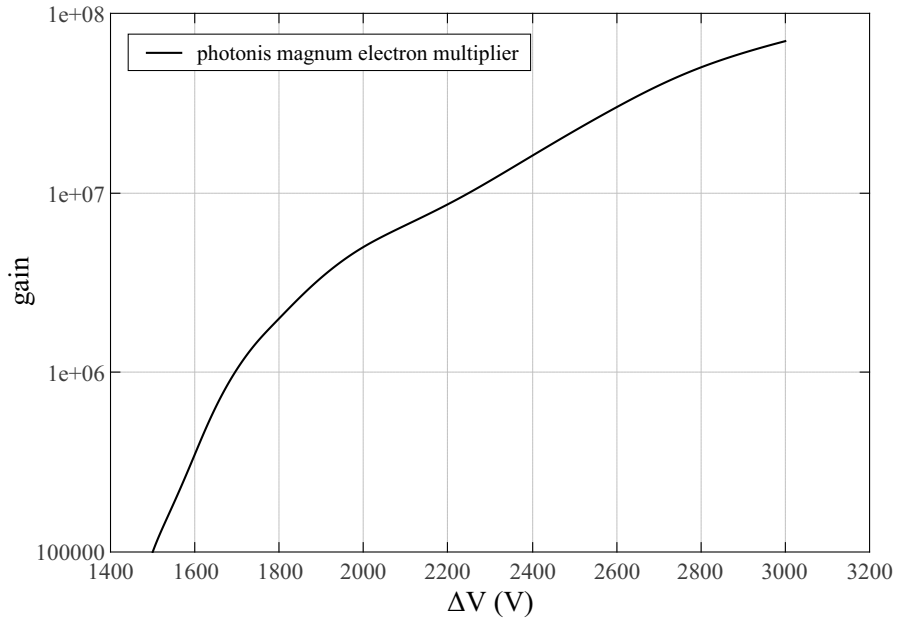

Figure A.2: Channeltron gain versus ΔV applied between cathode and anode for Photonis Magnum 5900 model.

The device that has been used in the tests is a Photonis Magnum electron multiplier 5900 and its main features are reported in the table A.1.

feature	value
length	3.96 cm
inner diameter	1 cm
resistance	38 MΩ

Table A.1: Pnotonis Magnum 5900 channeltron specifications.

I mounted the CEM into a teflon cylindrical holder where three metallic connectors guarantee the necessary voltage to the different parts of the channeltron. Two different bolts screwed up in the teflon ensure the contacts between CEM's anode-cathode and the corresponding wires, while a metallic pin connects directly the Faraday cup to the appropriate wire. The channeltron was maintained at a

fixed ΔV applied between cathode and anode. I designed an electrical scheme that takes into account every resistive parts of the system that includes the power supply, the HV filter and the channeltron. A photo of the CEM mounted into the bottom side of the holder is shown in the figure A.3.

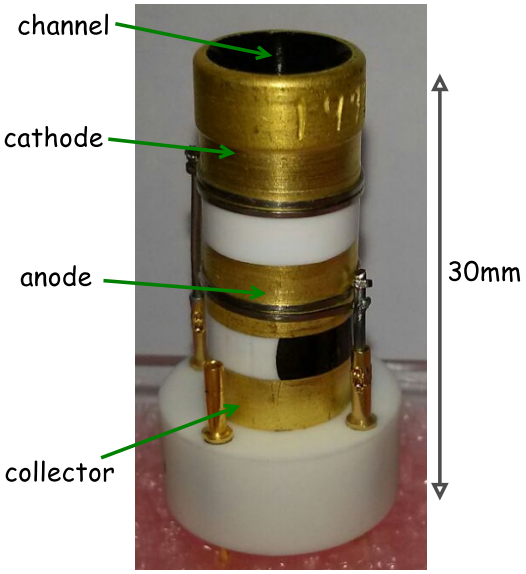

Figure A.3: Picture of the CEM mounted into the bottom teflon holder.

A.2 Electrostatic lens

The Einzel lens or unipotential lens is an electrostatic module that is used for focusing charged particles. In the scheme that I designed, it consists of three metallic rings at a different voltage in series along an axis. The inner diameter of these three rings (L1, L2, L3) is 23 mm. The electric field between these rings allows to change the radial velocity of the particles that will therefore converge on the axis. Before the lens (EL) I placed one initial accelerating grid (G) made of a copper mesh with a transparency of $\sim 90\%$. A wire is connected at every rings through a mini screw and it sets the potential. Three macor cylindrical columns hold all the rings at a fixed position, and a stainless-steel cylinder with diameter 40 mm, connected to the ground, encloses the lens in order to minimize the electric field dispersion. I also devised a set-up to test the behavior of the EL

and the channeltron. In this apparatus, the grid is placed at 20 mm from a gold foil deposited on a fused silica substrate where electrons are generated through photo-electric effect. The lens is instead mounted at 20 mm from the grid. L1, L2 and L3 are distant respectively 12 mm. The total length from the gold to the channeltron entrance is finally 100 mm.

A numerical simulation of the electric field was done using the program QuickField, and also the particle trajectory of electrons were simulated. This simulation was used in the choice of the correct values of the voltages necessary to focus electrons onto the 10 mm-entrance-diameter of the channeltron. The best parameters obtained in the simulation are listed in the table A.2, and in such a way, an electrostatic lens that focuses electrons into a spot of $5-6$ mm diameter at a distance of $\sim$35 mm from the last metallic ring (L3) can be obtained.

part	applied voltage (V)
G	1000
L1	700
L2	1700
L3	1300
mask	variable
channeltron cathode	2000
channeltron anode	3500

Table A.2: Einzel lens and channeltron voltage parameters.

Figure A.4 shows the simulated electric field in the system. Electrons trajectories are also drawn with pink lines. These electrons start from the gold substrate with an energy of 1 eV and the initial angle of the trajectory ranges between 0° to 180°.

A.2.1 Channeltron-mask

Background noise in single electron detection is one of the most critical issues in the proposed detection scheme. Besides the intrinsic channeltron dark count, every free negative charge in the vacuum chamber is accelerated toward the CEM resulting in an effective increase of the background counts. This effect can be

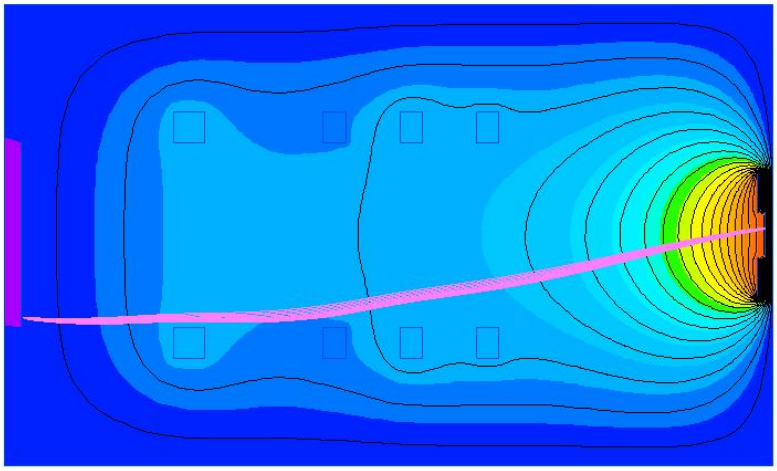

Figure A.4: Simulated electric field inside the electrostatic lens. Pink lines are the trajectory of electrons generated in the left part that corresponds to the gold substrate. It is clear the curvature effect on the trajectory due to the EL.

reduced, since only the electrons that come from the crystal contribute to the right signal. Knowing exactly the position of these electrons (they start their path where the crystal will be grown, which corresponds to the gold surface in the test set-up), all the other can be removed. I thus develop a system for the collection of all the electrons in the chamber that does not come from the EL that otherwise will enter in the channeltron. I called this system channeltron mask since it covers the top and lateral side of the CEM. The mask is a cylinder with a ring attached at one side. The diameter of the ring hole is 11 mm while the outer diameter, which coincides with the diameter of the cylinder, is 16 mm. The total length of the mask is 13 mm. The mask can be fixed at a certain voltage thanks to an opportune wire connection with a HV power supply.

A.3 Chamber

The tests have been carried out in a six-hole-cross, stainless-steel chamber that reproduces the cryostat environment. Vacuum pumps are directly connected to the chamber and they ensure a pressure $P_{chamber} \sim 3 \cdot 10^{-5}$ mbar. The front side of the chamber is equipped with a fused silica window that allows the entrance of UV laser radiation necessary for the generation of electrons through photoelectric

effect. In fact, electrons are generated when the UV photons impinge on the gold layer deposited at the internal side of the window. By so doing, electrons at the entrance of the electrostatic lens can be easily created. Neutral density filters (ND filters) can be placed before the chamber entrance on the UV beam to decrease the input energy and thus the number of electrons generated. Figure A.5 shows the channeltron and electrostatic lens test-set-up inside the vacuum chamber.

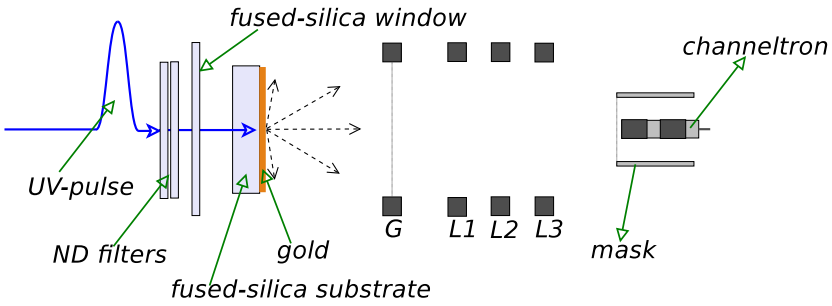

Figure A.5: Transversal section sketch of the set-up inside the vacuum chamber. On the left part the fused silica window allows the entrance of UV photons that impinge on gold substrate. The grid G and the Einzel lens made of three rings L1, L2, L3 allow electrons acceleration and focus into the channeltron which is covered by the mask. Different neutral density filters can be placed in the optical path to reduce the energy of UV pulses.

A.3.1 Electronics

High voltage necessary for the channeltron, the mask and the Einzel lens, is supplied by two different four-outputs NIM modules [1]. The HV necessary to operate the channeltron is furthermore filtered from the high frequency switching of the power supply using a π-filter. The channeltron collector, which is at the same high voltage as the anode, is connected to a capacitor that picks-up the charge signal that is then amplified. The grid, the electrostatic lens and the mask are instead directly connected to the power supply.

[1] CAEN N472 HV power supply

A.4 Tests

All the tests reported here were carried out at room temperature and at a pressure of $\approx 10^{-6}$ mbar.

A.4.1 Dark count measurements

I measured the dark count rate of the system *electrostatic lens plus channeltron* with a constant gain (G$\sim 3 \cdot 10^5 \rightarrow \Delta$V =1500 V) for different values of the mask voltage. Due to conditioning reasons, measurements are carried out ~ 30 min after the switch-on of the system. I saved 30 minutes of continuous acquisition of the signal triggering at a level that corresponds of less than a single electron (26 mV). The amplitude and the rate of the pulses are then obtained through off-line analysis of the data. The data of the dark count rate versus the voltage of the mask are shown in table A.3. Looking at the results, it is clear that, when the mask is

$V_{mask}(V)$ (mW)	Dark count (Hz)
1700	0.15
1300	0.26
700	1.38
0	7.6

Table A.3: Dark count rate of EL-channeltron system for different values of the channeltron mask voltage.

operated at a voltage which is just little bit higher than the channeltron anode voltage, the dark count drops to a very low level. This means that the major part of the counts come from real negative charges located in some part of the vacuum chamber that are accelerated toward the channeltron. These electrons are instead captured by the mask when it is switched on.

Dark spectrum with the mask at 1700 V and a gain of about $\sim 3 \cdot 10^5$ is shown in figure A.6. For a given gain of the channeltron and of the amplification chain it is possible to reconstruct with a high precision the number of electrons starting from the amplitude of the signal. Trigger was fixed at a level lower than the amplitude expected for a single electron (26 mV). Few electrons peaks are clearly visible in

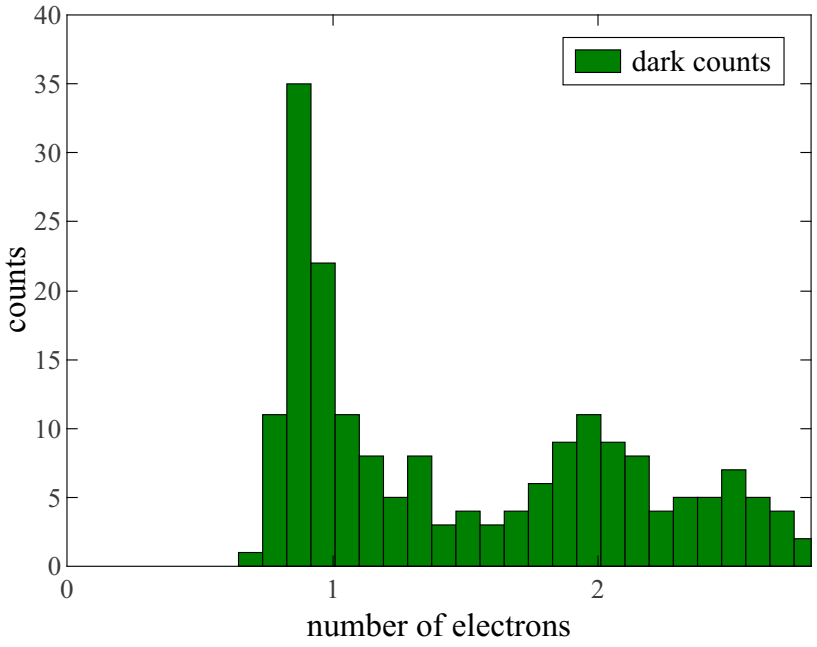

Figure A.6: Dark count spectrum of the Photonis Magnum 5900 CEM placed in our set-up.

the figure A.6.

A.4.2 Electrons measurements

Finally I tested the EL-channeltron system as a detector for few electrons. Electrons are created at the entrance of the EL, where the crystal will be placed, using photoelectric effect in the gold substrate as described in section A.3. Electrons generation takes place when the UV-laser pulses impinge on the gold surface. The duration of single pulse is $\sim$10 ns and the repetition rate is in the Hz range. The energy of the pulses can be tuned from 0.1 nJ to 50 μJ to achieve a different number of electrons injected into the system.

System calibration A calibration of the photocathode was necessary prior other tests to know the real number of electrons injected per unit of energy of the laser pulse. As already said, the photon-electron conversion efficiency in gold is strictly dependent of the surface characteristics and there is not any absolute

value in literature. Therefore, I measured directly the charge produced when a high energy pulse impinges on the gold. A negative voltage is applied at the photocatode and, through a capacitor, the signal, which is then amplified with a charge-amplifier (G∼0.66mV/fC) was picked-up. This test was done at a energy of $\sim \mu$J to obtain a measurable signal of a tens of mV. After many tests, a mean value of 125701 electrons per 1μJ of incident energy in the gold substrate can be calculated for the window I used. It is worth noting also that the number of electrons produced is strictly related to the position in which the laser strikes the gold surface. This is probably due to the imperfection in the Au surface itself. I also believe that pulses with energy major that $\sim$30 μJ creates damage effect in the gold surface. In fact, the pulses that follow one with a high energy, have a lower efficiency in the production of electrons. Due to these aspects, an uncertainty of about 20% in the number of electrons generation have been estimated.

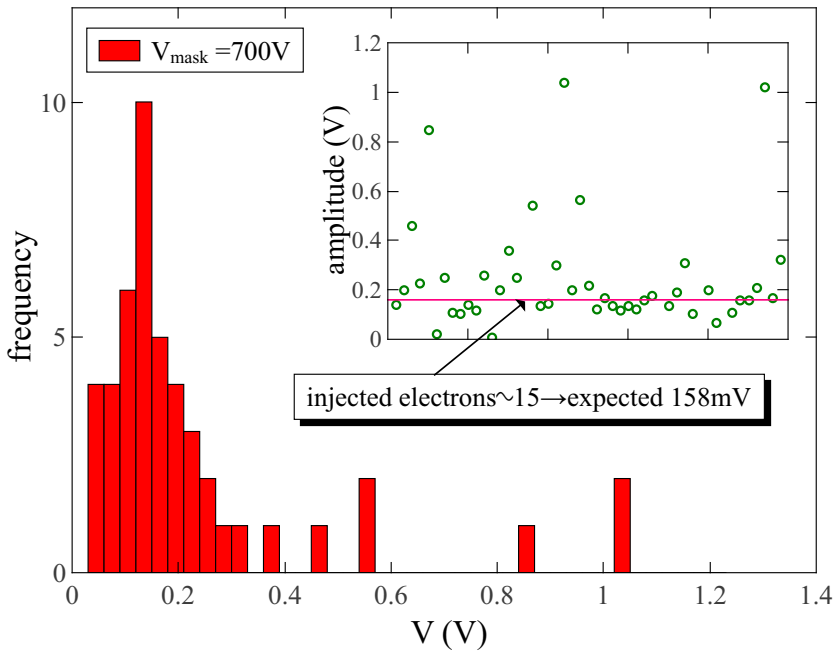

Figure A.7: Example of the detection of 15 electrons with our system. Pink line in the inset represents the expected amplitude value of the signal.

Few-electrons detection With the calibration above described I was able to set precisely the number of electrons, by setting directly the energy of the UV pulses

using neutral-density absorptive optical-filters. Figure A.7 shows as an example a number of 15 electrons injected in the electrostatic lens when channeltron gain is $3 \cdot 10^5$ and the mask voltage is 700 V. Electrons are injected at a rate of 0.5 Hz for 2 minutes and signals are acquired using an oscilloscope [2]. The expected value of ∼160 mV of amplitude is in well agreement with the maximum value obtained which is ∼ 150 mV. Large dispersion is due to the fluctuations in the low energy UV pulses.

A.5 Discussion

The development of a system for the test of the channeltron and an electrostatic lens is reported in this appendix. I measured the dark count of the system and I furthermore designed an innovative system capable to reduce of a factor ∼10 the number of dark counts. I also tested the system as electrons detector using laser-generated photo-electrons in a gold surface. A very low dark count of less than 10 mHz was measured, confirming the feasibility to implement a similar system for the proposed detection schemes also due to its very high efficiency and gain. The system is stable and it is easy to use in different set-ups. More tests concerning the possible application of such a system at cryogenic temperatures need to be done.

[2] Lecroy Wavesurfer 3054Z

Acknowledgments

The past five years have been extremely challenging for me. I had to deal with many aspects and issues of the "lab life" that I had never thought before. Fortunately, I was surrounded by many talented people with also a great patience that helped and supported me during these years: many thanks to all of you!

In particular, I would like to thank Giovanni Carugno, that has taught me a great deal of things! I have learnt not only physics from him, but many more valuable skills of the academic life. Furthermore many thanks to Caterina Braggio, Luca Tomassetti, Roberto Calabrese and Eleonora Luppi that put a lot of trust in me, and pointed me in the right direction during all these years.

I am indebted also with Mario Tessaro, who helped me many times! He gave me a lot of precious suggestions especially regarding the electronics and the signal formation. Moreover I wish to thank the technical team in Legnaro: Enrico Berto and Fulvio Calaon that contributes enormously to create my mechanical-fantasies and apparatus.

A big thanks goes to my office mates, my companions in the lab and, above all, my friends: Federico Chiossi, Nicolò Crescini and Sebastiano Gallo, with whom we discussed a lot about important issues (not only regarding physics...) and we passed great moments together! They kept me in the human world! Many thanks also to Alen Khanbekyan and Sergey Vasiukov with whom I passed hours in the lab.

Last, but not least by any means, I thank my parents, my brothers and my sister

which have been a fundamental support in all my life. They always push me to do the best!

Bibliography

[1] M. Battaglieri, A. Belloni, A. Chou, P. Cushman, B. Echenard, R. Essig, J. Estrada, J. L. Feng, B. Flaugher, P. J. Fox, *et al.*, "Us cosmic visions: new ideas in dark matter 2017: community report," *arXiv preprint arXiv:1707.04591*, 2017.

[2] F. Zwicky, "Die rotverschiebung von extragalaktischen nebeln," *Helvetica Physica Acta*, vol. 6, pp. 110–127, 1933.

[3] G. Bertone, D. Hooper, and J. Silk, "Particle dark matter: Evidence, candidates and constraints," *Physics reports*, vol. 405, no. 5-6, pp. 279–390, 2005.

[4] K. Begeman, A. Broeils, and R. Sanders, "Extended rotation curves of spiral galaxies: Dark haloes and modified dynamics," *Monthly Notices of the Royal Astronomical Society*, vol. 249, no. 3, pp. 523–537, 1991.

[5] J. F. Navarro, C. S. Frenk, and S. D. White, "A universal density profile from hierarchical clustering," *The Astrophysical Journal*, vol. 490, no. 2, p. 493, 1997.

[6] J. Buch, S. C. J. Leung, and J. Fan, "Using gaia dr2 to constrain local dark matter density and thin dark disk," *Journal of Cosmology and Astroparticle Physics*, vol. 2019, no. 04, p. 026, 2019.

[7] P. F. de Salas, "Dark matter local density determination based on recent observations," *arXiv preprint arXiv:1910.14366*, 2019.

[8] D. Walsh, R. F. Carswell, and R. J. Weymann, "0957+ 561 a, b: twin quasistellar objects or gravitational lens?," *Nature*, vol. 279, no. 5712, p. 381, 1979.

[9] T. E. Collett and M. W. Auger, "Cosmological constraints from the double source plane lens sdssj0946+ 1006," *Monthly Notices of the Royal Astronomical Society*, vol. 443, no. 2, pp. 969–976, 2014.

[10] A. A. Penzias and R. W. Wilson, "A measurement of excess antenna temperature at 4080 mc/s.," *The Astrophysical Journal*, vol. 142, pp. 419–421, 1965.

[11] R. Durrer, *The cosmic microwave background*, vol. 401. Cambridge University Press Cambridge, 2008.

[12] P. A. Ade, N. Aghanim, M. Arnaud, M. Ashdown, J. Aumont, C. Baccigalupi, A. Banday, R. Barreiro, J. Bartlett, N. Bartolo, *et al.*, "Planck 2015 results-xiii. cosmological parameters," *Astronomy & Astrophysics*, vol. 594, p. A13, 2016.

[13] N. Aghanim, Y. Akrami, M. Ashdown, J. Aumont, C. Baccigalupi, M. Ballardini, A. Banday, R. Barreiro, N. Bartolo, S. Basak, *et al.*, "Planck 2018 results. vi. cosmological parameters," *arXiv preprint arXiv:1807.06209*, 2018.

[14] J. L. Feng, "Dark matter candidates from particle physics and methods of detection," *Annual Review of Astronomy and Astrophysics*, vol. 48, pp. 495–545, 2010.

[15] A. V. Zasov, A. S. Saburova, A. V. Khoperskov, and S. A. Khoperskov, "Dark matter in galaxies," *Physics-Uspekhi*, vol. 60, no. 1, p. 3, 2017.

[16] P. F. de Salas and S. Pastor, "Relic neutrino decoupling with flavour oscillations revisited," *Journal of Cosmology and Astroparticle Physics*, vol. 2016, no. 07, p. 051, 2016.

[17] A. Loureiro, A. Cuceu, F. B. Abdalla, B. Moraes, L. Whiteway, M. McLeod, S. T. Balan, O. Lahav, A. Benoit-Lévy, M. Manera, R. P. Rollins, and H. S. Xavier, "Upper bound of neutrino masses from combined cosmological observations and particle physics experiments," *Phys. Rev. Lett.*, vol. 123, p. 081301, Aug 2019.

[18] R. D. Peccei, "The strong cp problem and axions," in *Axions*, pp. 3–17, Springer, 2008.

[19] J. Preskill, M. B. Wise, and F. Wilczek, "Cosmology of the invisible axion," *Physics Letters B*, vol. 120, no. 1-3, pp. 127–132, 1983.

[20] V. B. Klaer and G. D. Moore, "The dark-matter axion mass," *arXiv preprint arXiv:1708.07521*, 2017.

[21] L. F. Abbott and P. Sikivie, "A cosmological bound on the invisible axion," *Physics Letters B*, vol. 120, no. 1-3, pp. 133–136, 1983.

[22] L. D. Duffy and K. Van Bibber, "Axions as dark matter particles," *New Journal of Physics*, vol. 11, no. 10, p. 105008, 2009.

[23] J. E. Kim, "Weak-interaction singlet and strong cp invariance," *Physical Review Letters*, vol. 43, no. 2, p. 103, 1979.

[24] M. Dine and W. Fischler, "The not-so-harmless axion," *Physics Letters B*, vol. 120, no. 1-3, pp. 137–141, 1983.

[25] T. Asaka, K. Ishiwata, and T. Moroi, "Right-handed sneutrino as cold dark matter," *Physical Review D*, vol. 73, no. 5, p. 051301, 2006.

[26] J. Ellis, K. A. Olive, Y. Santoso, and V. C. Spanos, "Gravitino dark matter in the cmssm," *Physics Letters B*, vol. 588, no. 1-2, pp. 7–16, 2004.

[27] J. L. Feng, K. T. Matchev, and F. Wilczek, "Neutralino dark matter in focus point supersymmetry," *Physics Letters B*, vol. 482, no. 4, pp. 388–399, 2000.

[28] M. Pospelov, A. Ritz, and M. Voloshin, "Secluded wimp dark matter," *Physics Letters B*, vol. 662, no. 1, pp. 53–61, 2008.

[29] B. Audren, J. Lesgourgues, G. Mangano, P. D. Serpico, and T. Tram, "Strongest model-independent bound on the lifetime of dark matter," *Journal of Cosmology and Astroparticle Physics*, vol. 2014, no. 12, p. 028, 2014.

[30] X. Collaboration, E. Aprile, J. Aalbers, F. Agostini, M. Alfonsi, L. Althueser, F. Amaro, M. Anthony, F. Arneodo, L. Baudis, *et al.*, "Dark matter search results from a one ton-year exposure of xenon1t," *Physical Review Letters*, vol. 121, no. 11, p. 111302, 2018.

[31] B. Moore, S. Ghigna, F. Governato, G. Lake, T. Quinn, J. Stadel, and P. Tozzi, "Dark matter substructure within galactic halos," *The Astrophysical Journal Letters*, vol. 524, no. 1, p. L19, 1999.

[32] R. Catena and P. Ullio, "A novel determination of the local dark matter density," *Journal of Cosmology and Astroparticle Physics*, vol. 2010, no. 08, p. 004, 2010.

[33] A. K. Drukier, K. Freese, and D. N. Spergel, "Detecting cold dark-matter candidates," *Physical Review D*, vol. 33, no. 12, p. 3495, 1986.

[34] K. Freese, J. Frieman, and A. Gould, "Signal modulation in cold-dark-matter detection," *Physical Review D*, vol. 37, no. 12, p. 3388, 1988.

[35] J. Liu, X. Chen, and X. Ji, "Current status of direct dark matter detection experiments," *Nature Physics*, vol. 13, no. 3, p. 212, 2017.

[36] E. Brown, C. Hanley, U. Hommerich, A. Bluiett, and S. Trivedi *J. Lumin.*, vol. 133, pp. 244–248, 2013.

[37] P.-A. Amaudruz, M. Batygov, B. Beltran, J. Bonatt, M. Boulay, B. Broerman, J. Bueno, A. Butcher, B. Cai, M. Chen, *et al.*, "Deap-3600 dark matter search," *arXiv preprint arXiv:1410.7673*, 2014.

[38] R. Bernabei, P. Belli, R. Cerulli, F. Montecchia, M. Amato, G. Ignesti, A. Incicchitti, D. Prosperi, C. Dai, H. He, *et al.*, "Search for wimp annual modulation signature: Results from dama/nai-3 and dama/nai-4 and the global combined analysis," *Physics Letters B*, vol. 480, no. 1-2, pp. 23–31, 2000.

[39] M. Fairbairn and T. Schwetz, "Spin-independent elastic wimp scattering and the dama annual modulation signal," *Journal of Cosmology and Astroparticle Physics*, vol. 2009, no. 01, p. 037, 2009.

[40] G. Adhikari, P. Adhikari, E. B. de Souza, N. Carlin, S. Choi, M. Djamal, A. Ezeribe, C. Ha, I. Hahn, E. Jeon, *et al.*, "Search for a dark matter-induced annual modulation signal in nai (tl) with the cosine-100 experiment," *Physical review letters*, vol. 123, no. 3, p. 031302, 2019.

[41] E. B. de Souza, J. Cherwinka, A. Cole, A. Ezeribe, D. Grant, F. Halzen, K. Heeger, L. Hsu, A. Hubbard, J. Jo, *et al.*, "First search for a dark matter annual modulation signal with nai (tl) in the southern hemisphere by dm-ice17," *Physical Review D*, vol. 95, no. 3, p. 032006, 2017.

[42] J. Amare, S. Cebrian, C. Cuesta, E. Garcia, M. Martinez, M. Olivan, Y. Ortigoza, A. O. de Solorzano, C. Pobes, J. Puimedon, *et al.*, "Status of the anais dark matter project at the canfranc underground laboratory," in *Journal of Physics: Conference Series*, vol. 718, p. 042052, IOP Publishing, 2016.

[43] S.-T. Lin, H.-B. Li, X. Li, S. Lin, H. Wong, M. Deniz, B. Fang, D. He, J. Li, C. Lin, *et al.*, "New limits on spin-independent and spin-dependent couplings of low-mass wimp dark matter with a germanium detector at a threshold of 220 ev," *Physical Review D*, vol. 79, no. 6, p. 061101, 2009.

[44] C. E. Aalseth, P. S. Barbeau, J. Colaresi, J. Collar, J. D. Leon, J. E. Fast, N. Fields, T. W. Hossbach, A. Knecht, M. S. Kos, *et al.*, "Cogent: A search for low-mass dark matter using p-type point contact germanium detectors," *Physical Review D*, vol. 88, no. 1, p. 012002, 2013.

[45] K.-J. Kang, J.-P. Cheng, J. Li, Y.-J. Li, Q. Yue, Y. Bai, Y. Bi, J.-P. Chang, N. Chen, N. Chen, *et al.*, "Introduction to the cdex experiment," *Frontiers of Physics*, vol. 8, no. 4, pp. 412–437, 2013.

[46] A. Aguilar-Arevalo, D. Amidei, X. Bertou, M. Butner, G. Cancelo, A. C. Vazquez, B. C. Vergara, A. Chavarria, C. Chavez, J. de Mello Neto, *et al.*, "Search for low-mass wimps in a 0.6 kg day exposure of the damic experiment at snolab," *Physical Review D*, vol. 94, no. 8, p. 082006, 2016.

[47] M. Crisler, R. Essig, J. Estrada, G. Fernandez, J. Tiffenberg, M. S. Haro, T. Volansky, T.-T. Yu, S. Collaboration, *et al.*, "Sensei: first direct-detection constraints on sub-gev dark matter from a surface run," *Physical review letters*, vol. 121, no. 6, p. 061803, 2018.

[48] C. Amole, M. Ardid, D. M. Asner, D. Baxter, E. Behnke, P. Bhattacharjee, H. Borsodi, M. Bou-Cabo, S. Brice, D. Broemmelsiek, *et al.*, "Dark matter search results from the pico-2l c 3 f 8 bubble chamber," *Physical review letters*, vol. 114, no. 23, p. 231302, 2015.

[49] R. Strauss, J. Rothe, G. Angloher, A. Bento, A. Gutlein, D. Hauff, H. Kluck, M. Mancuso, L. Oberauer, F. Petricca, *et al.*, "Gram-scale cryogenic calorimeters for rare-event searches," *Physical Review D*, vol. 96, no. 2, p. 022009, 2017.

[50] C. Arnaboldi, F. Avignone Iii, J. Beeman, M. Barucci, M. Balata, C. Brofferio, C. Bucci, S. Cebrian, R. Creswick, S. Capelli, *et al.*, "Cuore: a cryogenic underground observatory for rare events," *Nuclear Instruments and Methods in Physics Research Section A: Accelerators, Spectrometers, Detectors and Associated Equipment*, vol. 518, no. 3, pp. 775–798, 2004.

[51] T. C. I. Group, "Cupid: Cuore (cryogenic underground observatory for rare events) upgrade with particle identification," *arXiv preprint arXiv:1504.03599*, 2015.

[52] D. Artusa, F. Avignone III, J. Beeman, I. Dafinei, L. Dumoulin, Z. Ge, A. Giuliani, C. Gotti, P. de Marcillac, S. Marnieros, *et al.*, "Enriched teo2 bolometers with active particle discrimination: Towards the cupid experiment," *Physics Letters B*, vol. 767, pp. 321–329, 2017.

[53] S. Pirro and P. Mauskopf, "Advances in bolometer technology for fundamental physics," *Annual Review of Nuclear and Particle Science*, vol. 67, pp. 161–181, 2017.

[54] D. Akerib, S. Alsum, H. Araújo, X. Bai, A. Bailey, J. Balajthy, P. Beltrame, E. Bernard, A. Bernstein, T. Biesiadzinski, *et al.*, "Calibration, event reconstruction, data analysis, and limit calculation for the lux dark matter experiment," *Physical Review D*, vol. 97, no. 10, p. 102008, 2018.

[55] D. Akerib, S. Alsum, H. Araújo, X. Bai, J. Balajthy, P. Beltrame, E. Bernard, A. Bernstein, T. Biesiadzinski, E. Boulton, *et al.*, "Search for annual and diurnal rate modulations in the lux experiment," *Physical Review D*, vol. 98, no. 6, p. 062005, 2018.

[56] X. Collaboration, E. Aprile, J. Aalbers, F. Agostini, M. Alfonsi, L. Althueser, F. Amaro, M. Anthony, F. Arneodo, L. Baudis, *et al.*, "Dark matter search results from a one ton-year exposure of xenon1t," *Physical Review Letters*, vol. 121, no. 11, p. 111302, 2018.

[57] X. Collaboration, E. Aprile, J. Aalbers, F. Agostini, M. Alfonsi, L. Althueser, F. Amaro, M. Anthony, V. Antochi, F. Arneodo, *et al.*, "Constraining the spin-dependent wimp-nucleon cross sections with xenon1t," *Physical review letters*, vol. 122, no. 14, p. 141301, 2019.

[58] E. Aprile, J. Aalbers, F. Agostini, M. Alfonsi, F. Amaro, M. Anthony, L. Arazi, F. Arneodo, C. Balan, P. Barrow, *et al.*, "Physics reach of the xenon1t dark matter experiment.," *Journal of Cosmology and Astroparticle Physics*, vol. 2016, no. 04, p. 027, 2016.

[59] X. Cui, A. Abdukerim, W. Chen, X. Chen, Y. Chen, B. Dong, D. Fang, C. Fu, K. Giboni, F. Giuliani, *et al.*, "Dark matter results from 54-ton-day exposure of pandax-ii experiment," *Physical review letters*, vol. 119, no. 18, p. 181302, 2017.

[60] H. Zhang, A. Abdukerim, W. Chen, X. Chen, Y. Chen, X. Cui, B. Dong, D. Fang, C. Fu, K. Giboni, *et al.*, "Dark matter direct search sensitivity of the pandax-4t experiment," *SCIENCE CHINA Physics, Mechanics & Astronomy*, vol. 62, no. 3, p. 31011, 2019.

[61] P. Agnes, T. Alexander, A. Alton, K. Arisaka, H. Back, B. Baldin, K. Biery, G. Bonfini, M. Bossa, A. Brigatti, *et al.*, "First results from the darkside-50 dark matter experiment at laboratori nazionali del gran sasso," *Physics Letters B*, vol. 743, pp. 456–466, 2015.

[62] J. Howlett and E. Aprile, "The xenonnt dark matter search experiment," *Bulletin of the American Physical Society*, vol. 64, 2019.

[63] D. Akerib, C. Akerlof, S. Alsum, H. Araújo, M. Arthurs, X. Bai, A. Bailey, J. Balajthy, S. Balashov, D. Bauer, *et al.*, "Projected wimp sensitivity of the lux-zeplin (lz) dark matter experiment," *arXiv preprint arXiv:1802.06039*, 2018.

[64] J. Aalbers, F. Agostini, M. Alfonsi, F. Amaro, C. Amsler, E. Aprile, L. Arazi, F. Arneodo, P. Barrow, L. Baudis, *et al.*, "Darwin: towards the ultimate dark matter detector," *Journal of Cosmology and Astroparticle Physics*, vol. 2016, no. 11, p. 017, 2016.

[65] E. García, J. Puimedón, M. Sarsa, L. Torres, N. Coron, P. de Marcillac, J. Gironnet, J. Leblanc, and T. Redon, "High performance scintillating bolometers in the search for wimps: Rosebud experiment," in *The Identification Of Dark Matter*, pp. 302–307, World Scientific, 2007.

[66] F. Petricca, G. Angloher, P. Bauer, A. Bento, C. Bucci, L. Canonica, X. Defay, A. Erb, F. v. Feilitzsch, N. F. Iachellini, *et al.*, "First results on low-mass dark matter from the cresst-iii experiment," *arXiv preprint arXiv:1711.07692*, 2017.

[67] A. Barabash, D. Chernyak, F. Danevich, A. Giuliani, I. Ivanov, E. Makarov, M. Mancuso, S. Marnieros, S. Nasonov, C. Nones, *et al.*, "Enriched znmoo scintillating bolometers to search for ..... decay of mo with the lumineu experiment," *The European Physical Journal C*, vol. 74, no. 10, p. 3133, 2014.

[68] R. Agnese, A. Anderson, M. Asai, D. Balakishiyeva, R. B. Thakur, D. Bauer, J. Billard, A. Borgland, M. Bowles, D. Brandt, *et al.*, "Search for low-mass weakly interacting massive particles using voltage-assisted calorimetric ionization detection in the supercdms experiment," *Physical review letters*, vol. 112, no. 4, p. 041302, 2014.

[69] R. Agnese, A. Anderson, T. Aramaki, I. Arnquist, W. Baker, D. Barker, R. B. Thakur, D. Bauer, A. Borgland, M. Bowles, *et al.*, "Projected sensitivity of the supercdms snolab experiment," *Physical Review D*, vol. 95, no. 8, p. 082002, 2017.

[70] P. W. Graham, I. G. Irastorza, S. K. Lamoreaux, A. Lindner, and K. A. van Bibber, "Experimental searches for the axion and axion-like particles," *Annual Review of Nuclear and Particle Science*, vol. 65, pp. 485–514, 2015.

[71] N. Du, N. Force, R. Khatiwada, E. Lentz, R. Ottens, L. Rosenberg, G. Rybka, G. Carosi, N. Woollett, D. Bowring, *et al.*, "Search for invisible axion dark matter with the axion dark matter experiment," *Physical review letters*, vol. 120, no. 15, p. 151301, 2018.

[72] R. Khatiwada, "First results from the generation-2 axion dark matter experiment (admx)," *Bulletin of the American Physical Society*, vol. 64, 2019.

[73] L. Zhong, S. Al Kenany, K. Backes, B. Brubaker, S. Cahn, G. Carosi, Y. Gurevich, W. Kindel, S. Lamoreaux, K. Lehnert, *et al.*, "Results from phase 1 of the haystac microwave cavity axion experiment," *Physical Review D*, vol. 97, no. 9, p. 092001, 2018.

[74] R. Barbieri, C. Braggio, G. Carugno, C. S. Gallo, A. Lombardi, A. Ortolan, R. Pengo, G. Ruoso, and C. C. Speake, "Searching for galactic axions through magnetized media: the quax proposal," *Physics of the Dark Universe*, vol. 15, pp. 135–141, 2017.

[75] V. Anastassopoulos, S. Aune, K. Barth, A. Belov, H. Bräuninger, G. Cantatore, J. Carmona, J. Castel, S. Cetin, F. Christensen, *et al.*, "New cast limit on the axion–photon interaction," *Nature Physics*, vol. 13, no. 6, p. 584, 2017.

[76] E. Armengaud, F. Avignone, M. Betz, P. Brax, P. Brun, G. Cantatore, J. Carmona, G. Carosi, F. Caspers, S. Caspi, *et al.*, "Conceptual design of the international axion observatory (iaxo)," *Journal of Instrumentation*, vol. 9, no. 05, p. T05002, 2014.

[77] A. Garcon, D. Aybas, J. W. Blanchard, G. Centers, N. L. Figueroa, P. W. Graham, D. F. J. Kimball, S. Rajendran, M. G. Sendra, A. O. Sushkov, *et al.*, "The cosmic axion spin precession experiment (casper): a dark-matter search with nuclear magnetic resonance," *Quantum Science and Technology*, vol. 3, no. 1, p. 014008, 2017.

[78] B. Majorovits and J. Redondo, "Madmax: A new dark matter axion search using a dielectric haloscope," *arXiv preprint arXiv:1611.04549*, 2016.

[79] J. Abdallah, A. Ashkenazi, A. Boveia, G. Busoni, A. De Simone, C. Doglioni, A. Efrati, E. Etzion, J. Gramling, T. Jacques, *et al.*, "Simplified models for dark matter and missing energy searches at the lhc," *arXiv preprint arXiv:1409.2893*, 2014.

[80] A. M. Sirunyan, A. Tumasyan, W. Adam, F. Ambrogi, E. Asilar, T. Bergauer, J. Brandstetter, M. Dragicevic, J. Erö, A. E. Del Valle, *et al.*, "Search for dark matter particles produced in association with a top quark pair at s= 13 tev," *Physical review letters*, vol. 122, no. 1, p. 011803, 2019.

[81] D. Abercrombie, N. Akchurin, E. Akilli, J. A. Maestre, B. Allen, B. A. Gonzalez, J. Andrea, A. Arbey, G. Azuelos, P. Azzi, *et al.*, "Dark matter benchmark models for early lhc run-2 searches: report of the atlas/cms dark matter forum," *arXiv preprint arXiv:1507.00966*, 2015.

[82] G. Aad, T. Abajyan, B. Abbott, J. Abdallah, S. A. Khalek, A. Abdelalim, O. Abdinov, R. Aben, B. Abi, M. Abolins, *et al.*, "Search for dark matter candidates and large extra dimensions in events with a jet and missing transverse momentum with the atlas detector," *Journal of High Energy Physics*, vol. 2013, no. 4, p. 75, 2013.

[83] O. Buchmueller, M. J. Dolan, S. A. Malik, and C. McCabe, "Characterising dark matter searches at colliders and direct detection experiments: vector mediators," *Journal of High Energy Physics*, vol. 2015, no. 1, p. 37, 2015.

[84] D. R. Lide, *CRC handbook of chemistry and physics*, vol. 85. CRC press, 2004.

[85] W. M. Haynes, *CRC handbook of chemistry and physics*. CRC press, 2014.

[86] M. L. Klein and J. A. Venables, *Rare gas solids*, vol. 1. Academic Press, 1976.

[87] R. Platzman, "Total ionization in gases by high-energy particles: An appraisal of our understanding," *The International Journal of Applied Radiation and Isotopes*, vol. 10, no. 2-3, pp. 116–127, 1961.

[88] A. C. Sinnock and B. L. Smith, "Refractive indices of the condensed inert gases," *Phys. Rev.*, vol. 181, pp. 1297–1307, May 1969.

[89] E. Aprile, A. E. Bolotnikov, A. I. Bolozdynya, and T. Doke, *Noble gas detectors*. John Wiley & Sons, 2006.

[90] P. Sorensen, A. Manzur, C. Dahl, J. Angle, E. Aprile, F. Arneodo, L. Baudis, A. Bernstein, A. Bolozdynya, L. Coelho, *et al.*, "The scintillation and ionization yield of liquid xenon for nuclear recoils," *Nuclear Instruments and Methods in Physics Research Section A: Accelerators, Spectrometers, Detectors and Associated Equipment*, vol. 601, no. 3, pp. 339–346, 2009.

[91] A. Bondar, A. Buzulutskov, A. Dolgov, E. Grishnyaev, V. Nosov, V. Oleynikov, S. Polosatkin, L. Shekhtman, E. Shemyakina, and A. Sokolov, "Measurement of the ionization yield of nuclear recoils in liquid argon using a two-phase detector with electroluminescence gap," *Journal of Instrumentation*, vol. 12, no. 05, p. C05010, 2017.

[92] W. Von Zdrojewski, J. Rabe, and W. Schmidt, "Photoelectric determination of v0-values in solid rare gases," *Zeitschrift fur Naturforschung A*, vol. 35, no. 7, pp. 672–674, 1980.

[93] W. Schmidt, *Liquid state electronics of insulating liquids*. CRC Press, 1997.

[94] W. Tauchert, H. Jungblut, and W. F. Schmidt, "Photoelectric determination of v 0 values and electron ranges in some cryogenic liquids," *Canadian Journal of Chemistry*, vol. 55, no. 11, pp. 1860–1866, 1977.

[95] A. Hitachi, "Properties of liquid xenon scintillation for dark matter searches," *Astroparticle Physics*, vol. 24, no. 3, pp. 247–256, 2005.

[96] A. Hitachi, "Exciton kinetics in condensed rare gases," *The Journal of chemical physics*, vol. 80, no. 2, pp. 745–748, 1984.

[97] K. Niebel and J. Venables, "An explanation of the crystal structure of the rare gas solids," *Proceedings of the Royal Society of London. A. Mathematical and Physical Sciences*, vol. 336, no. 1606, pp. 365–377, 1974.

[98] P. Schwerdtfeger, N. Gaston, R. P. Krawczyk, R. Tonner, and G. E. Moyano, "Extension of the lennard-jones potential: Theoretical investigations into rare-gas clusters and crystal lattices of he, ne, ar, and kr using many-body interaction expansions," *Physical Review B*, vol. 73, no. 6, p. 064112, 2006.

[99] A. P. Mills Jr and E. Gullikson, "Solid neon moderator for producing slow positrons," *Applied Physics Letters*, vol. 49, no. 17, pp. 1121–1123, 1986.

[100] G. Testera, S. Aghion, C. Amsler, A. Ariga, T. Ariga, A. Belov, G. Bonomi, P. Braunig, J. Bremer, R. Brusa, *et al.*, "The aegis experiment," *Hyperfine Interactions*, vol. 233, no. 1-3, pp. 13–20, 2015.

[101] A. M. Stoneham, *Theory of defects in solids: electronic structure of defects in insulators and semiconductors*. Oxford University Press, 2001.

[102] J. P. Hirth and L. Kubin, *Dislocations in solids*, vol. 15. Elsevier, 2009.

[103] F. R. Nabarro and M. S. Duesbery, *Dislocations in solids*, vol. 11. Elsevier, 2002.

[104] A. Baldini, C. Bemporad, F. Cei, T. Doke, M. Grassi, A. Grebenuk, D. Grigoriev, T. Haruyama, K. Kasami, J. Kikuchi, *et al.*, "Absorption of scintillation light in a 100 l liquid xenon γ-ray detector and expected detector performance," *Nuclear Instruments and Methods in Physics Research Section A: Accelerators, Spectrometers, Detectors and Associated Equipment*, vol. 545, no. 3, pp. 753–764, 2005.

[105] S. Rotman, "The effect of defects on inorganic luminescent materials," in *Wide-Gap Luminescent Materials: Theory and Applications*, pp. 139–190, Springer, 1997.

[106] F. Forstmann and S. Ossicini, "The influence of a rare-gas matrix on the electronic levels of isolated atoms," *The Journal of Chemical Physics*, vol. 73, no. 12, pp. 5997–6002, 1980.

[107] I. R. Dunkin, *Matrix-isolation techniques: a practical approach*. Oxford University Press Oxford, 1998.

[108] S. Cradock and A. Hinchcliffe, *Matrix Isolation: A technique for the study of reactive inorganic species*. CUP Archive, 1975.

[109] W. Weyhmann and F. Pipkin, "Optical absorption spectra of alkali atoms in rare-gas matrices," *Physical Review*, vol. 137, no. 2A, p. A490, 1965.

[110] T. Momose and T. Shida, "Matrix-isolation spectroscopy using solid parahydrogen as the matrix: application to high-resolution spectroscopy, photochemistry, and cryochemistry," *Bulletin of the Chemical Society of Japan*, vol. 71, no. 1, pp. 1–15, 1998.

[111] S. Tam, M. E. Fajardo, H. Katsuki, H. Hoshina, T. Wakabayashi, and T. Momose, "High resolution infrared absorption spectra of methane molecules isolated in solid parahydrogen matrices," *The Journal of chemical physics*, vol. 111, no. 9, pp. 4191–4198, 1999.

[112] A. N. Kanagin, S. K. Regmi, P. Pathak, and J. D. Weinstein, "Optical pumping of rubidium atoms frozen in solid argon," *Physical Review A*, vol. 88, no. 6, p. 063404, 2013.

[113] I. Gerhardt, K. Sin, and T. Momose, "Excitation and emission spectra of rubidium in rare-gas thin-films," *The Journal of chemical physics*, vol. 137, no. 1, p. 014507, 2012.

[114] R. Lambo, A. Buchachenko, L. Wu, Y. Tan, J. Wang, Y. Sun, A.-W. Liu, and S.-M. Hu, "Electronic spectroscopy of ytterbium in a neon matrix," *The Journal of chemical physics*, vol. 137, no. 20, p. 204315, 2012.

[115] C.-Y. Xu, S.-M. Hu, J. Singh, K. Bailey, Z.-T. Lu, P. Mueller, T. O Connor, U. Welp, *et al.*, "Optical excitation and decay dynamics of ytterbium atoms embedded in a solid neon matrix," *Physical review letters*, vol. 107, no. 9, p. 093001, 2011.

[116] A. I. Bolozdynya, "Two-phase emission detectors: foundations and applications," *IEEE transactions on dielectrics and electrical insulation*, vol. 13, no. 3, pp. 616–623, 2006.

[117] G. Fraser, J. Pearson, and J. Lees, "Dark noise in microchannel plate x-ray detectors," *Nuclear Instruments and Methods in Physics Research Section A: Accelerators, Spectrometers, Detectors and Associated Equipment*, vol. 254, no. 2, pp. 447–462, 1987.

[118] H. corporation, "Phoshor efficiency in low-energy electrons detection." private comunication, 2017.

[119] A. Gola, F. Acerbi, M. Capasso, M. Marcante, A. Mazzi, G. Paternoster, C. Piemonte, V. Regazzoni, and N. Zorzi, "Nuv-sensitive silicon photomultiplier technologies developed at fondazione bruno kessler," *Sensors*, vol. 19, no. 2, p. 308, 2019.

[120] Y. Sun, K. Choi, J. Maricic, M. D. Cruz, C. Nelson, M. Rosen, and R. Milincic, "Silicon photomultiplier low temperature characterization for future neutrino detectors," in *Journal of Physics: Conference Series*, vol. 888, p. 012068, IOP Publishing, 2017.

[121] R. W. Schnee, "Introduction to dark matter experiments," in *Physics of the Large and the Small: TASI 2009*, pp. 775–829, World Scientific, 2011.

[122] J. Engel, S. Pittel, and P. Vogel, "Nuclear physics of dark matter detection," *International Journal of Modern Physics E*, vol. 1, no. 01, pp. 1–37, 1992.

[123] N. Bloembergen, "Solid state infrared quantum counters," *Physical Review Letters*, vol. 2, no. 3, p. 84, 1959.

[124] "Infn lnl internal report of infrared quantum counters." private comunication, 2015.

[125] G. G. Raffelt, "Astrophysical axion bounds," in *Axions*, pp. 51–71, Springer, 2008.

[126] D. J. Marsh, "Axion cosmology," *Physics Reports*, vol. 643, pp. 1–79, 2016.

[127] P. Sikivie, "Experimental tests of the" invisible" axion," *Physical Review Letters*, vol. 51, no. 16, p. 1415, 1983.

[128] P. Sikivie, "Axion dark matter detection using atomic transitions," *Physical review letters*, vol. 113, no. 20, p. 201301, 2014.

[129] R. Wannemacher, D. Boye, Y. Wang, R. Pradhan, W. Grill, J. Rives, and R. Meltzer, "Zeeman-switched optical-free-induction decay and dephasing in ylif 4: Er 3+," *Physical Review B*, vol. 40, no. 7, p. 4237, 1989.

[130] D. DeMille, "Quantum computation with trapped polar molecules," *Physical Review Letters*, vol. 88, no. 6, p. 067901, 2002.

[131] C. Thiel, T. Böttger, and R. Cone, "Rare-earth-doped materials for applications in quantum information storage and signal processing," *Journal of luminescence*, vol. 131, no. 3, pp. 353–361, 2011.

[132] S. Bertaina, S. Gambarelli, A. Tkachuk, I. Kurkin, B. Malkin, A. Stepanov, and B. Barbara, "Rare-earth solid-state qubits," *Nature nanotechnology*, vol. 2, no. 1, p. 39, 2007.

[133] B. Arora, M. Safronova, and C. W. Clark, "Tune-out wavelengths of alkali-metal atoms and their applications," *Physical Review A*, vol. 84, no. 4, p. 043401, 2011.

[134] T. Yanagida, "Study of rare-earth-doped scintillators," *Optical Materials*, vol. 35, no. 11, pp. 1987–1992, 2013.

[135] K. Kramer, P. Dorenbos, H.-U. Gudel, and C. Van Eijk, "Development and characterization of highly efficient new cerium doped rare earth halide scintillator materials," *Journal of Materials Chemistry*, vol. 16, no. 27, pp. 2773–2780, 2006.

[136] L. Esterowitz, A. Schnitzler, J. Noonan, and J. Bahler, "Rare earth infrared quantum counter," *Applied optics*, vol. 7, no. 10, pp. 2053–2070, 1968.

[137] R. A. Hewes and J. F. Sarver, "Infrared excitation processes for the visible luminescence of er 3+, ho 3+, and tm 3+ in yb 3+-sensitized rare-earth trifluorides," *Physical Review*, vol. 182, no. 2, p. 427, 1969.

[138] J. Wright, "Up-conversion and excited state energy transfer in rare-earth doped materials," in *Radiationless processes in molecules and condensed phases*, pp. 239–295, Springer, 1976.

[139] A. Borghesani, C. Braggio, G. Carugno, F. Chiossi, A. Di Lieto, M. Guarise, G. Ruoso, and M. Tonelli, "Particle detection through the quantum counter concept in yag: Er3+," *Applied Physics Letters*, vol. 107, no. 19, p. 193501, 2015.

[140] C. Braggio, G. Carugno, F. Chiossi, A. Di Lieto, M. Guarise, P. Maddaloni, A. Ortolan, G. Ruoso, L. Santamaria, J. Tasseva, *et al.*, "Axion dark matter detection by laser induced fluorescence in rare-earth doped materials," *Scientific reports*, vol. 7, no. 1, p. 15168, 2017.

[141] E. Brown, E. Kumi-Barimah, U. Hömmerich, A. Bluiett, and S. Trivedi, "Material purification, crystal growth, and spectroscopy of tm-doped kpb2cl5 and kpb2br5 for 2 μm photonic applications," *Journal of Crystal Growth*, vol. 393, pp. 159–162, 2014.

[142] S. Mukherjee and S. P. S. Gupta, *Frontiers in Atomic, Molecular and Optical Physics, Vol. 3.* Allied Publishers, 2003.

[143] A. J. Leggett, "Bose-einstein condensation in the alkali gases: Some fundamental concepts," *Reviews of Modern Physics*, vol. 73, no. 2, p. 307, 2001.

[144] I. I. Sobelman, *Atomic spectra and radiative transitions*, vol. 12. Springer Science & Business Media, 2012.

[145] J. M. Hollas, *Modern spectroscopy.* John Wiley & Sons, 2004.

[146] J. D. Prestage, R. L. Tjoelker, and L. Maleki, "Atomic clocks and variations of the fine structure constant," *Physical review letters*, vol. 74, no. 18, p. 3511, 1995.

[147] T. Hong, C. Cramer, W. Nagourney, and E. Fortson, "Optical clocks based on ultranarrow three-photon resonances in alkaline earth atoms," *Physical review letters*, vol. 94, no. 5, p. 050801, 2005.

[148] Y.-Y. Jau, A. Post, N. Kuzma, A. Braun, M. V. Romalis, and W. Happer, "Intense, narrow atomic-clock resonances," *Physical review letters*, vol. 92, no. 11, p. 110801, 2004.

[149] L.-A. Liew, S. Knappe, J. Moreland, H. Robinson, L. Hollberg, and J. Kitching, "Microfabricated alkali atom vapor cells," *Applied Physics Letters*, vol. 84, no. 14, pp. 2694–2696, 2004.

[150] J. Guena, P. Rosenbusch, P. Laurent, M. Abgrall, D. Rovera, G. Santarelli, M. E. Tobar, S. Bize, and A. Clairon, "Demonstration of a dual alkali rb/cs fountain clock," *IEEE transactions on ultrasonics, ferroelectrics, and frequency control*, vol. 57, no. 3, pp. 647–653, 2010.

[151] L. Corradi, B. Behera, E. Fioretto, A. Gadea, A. Latina, A. Stefanini, S. Szilner, M. Trotta, Y. Wu, S. Beghini, *et al.*, "Excitation functions for fr 208–211 produced in the o 18+ au 197 fusion reaction," *Physical Review C*, vol. 71, no. 1, p. 014609, 2005.

[152] M. Maric, J. McFerran, and A. Luiten, "Frequency-comb spectroscopy of the d 1 line in laser-cooled rubidium," *Physical Review A*, vol. 77, no. 3, p. 032502, 2008.

[153] S. Upadhyay, A. N. Kanagin, C. Hartzell, T. Christy, W. P. Arnott, T. Momose, D. Patterson, and J. D. Weinstein, "Longitudinal spin relaxation of optically pumped rubidium atoms in solid parahydrogen," *Physical review letters*, vol. 117, no. 17, p. 175301, 2016.

[154] D. Peek, I. Fujita, M. Schmidt, and R. Simmons, "Single-particle kinetic energies in solid neon," *Physical Review B*, vol. 45, no. 17, p. 9680, 1992.

[155] R. Michniak, R. Alleaume, D. McKinsey, and J. Doyle, "Alpha and beta particle induced scintillations in liquid and solid neon," *Nuclear Instruments and Methods in Physics Research Section A: Accelerators, Spectrometers, Detectors and Associated Equipment*, vol. 482, no. 1-2, pp. 387–394, 2002.

[156] G. Carugno, G. Bressi, S. Cerdonio, E. Conti, A. Meneguzzo, R. Onofrio, D. Zanello, U. Beriotto, S. De Biasia, M. Nicoletto, *et al.*, "A large liquid xenon time projection chamber for the study of the radiative pion decay,"

Nuclear Instruments and Methods in Physics Research Section A: Accelerators, Spectrometers, Detectors and Associated Equipment, vol. 376, no. 2, pp. 149–154, 1996.

[157] J. Fischer and T. Rao-Srinivasan, "technical report," tech. rep., Brookhaven National Lab., 1988.

[158] F. Le Pimpec, C. Milne, C. Hauri, and F. Ardana-Lamas, "Quantum efficiency of technical metal photocathodes under laser irradiation of various wavelengths," *Applied Physics A*, vol. 112, no. 3, pp. 647–661, 2013.

[159] B. A. Tom, S. Bhasker, Y. Miyamoto, T. Momose, and B. J. McCall, "Producing and quantifying enriched para-h 2," *Review of scientific instruments*, vol. 80, no. 1, p. 016108, 2009.

[160] D. N. Balakishiyeva, R. Mahapatra, T. Saab, and J. Yoo, "Solid xenon project," in *AIP Conference Proceedings*, vol. 1274, pp. 138–143, AIP, 2010.

[161] H. J. Scheel, "The development of crystal growth technology," *Crystal Growth Technology*, pp. 3–14, 2003.

[162] J. Yoo, H. Cease, W. Jaskierny, D. Markley, R. Pahlka, D. Balakishiyeva, T. Saab, and M. Filipenko, "Scalability study of solid xenon," *Journal of Instrumentation*, vol. 10, no. 04, p. P04009, 2015.

[163] M. Tanabashi, K. Hagiwara, K. Hikasa, K. Nakamura, Y. Sumino, F. Takahashi, J. Tanaka, K. Agashe, G. Aielli, C. Amsler, *et al.*, "Review of particle physics," *Physical Review D*, vol. 98, no. 3, p. 030001, 2018.

[164] D. R. Sears and H. P. Klug, "Density and expansivity of solid xenon," *The Journal of Chemical Physics*, vol. 37, no. 12, pp. 3002–3006, 1962.

[165] J. Yoo and W. Jaskierny, "Electron drift in a large scale solid xenon," *Journal of Instrumentation*, vol. 10, no. 08, p. P08011, 2015.

[166] E. Aprile and T. Doke, "Liquid xenon detectors for particle physics and astrophysics," *Reviews of Modern Physics*, vol. 82, no. 3, p. 2053, 2010.

[167] K. Ueshima, K. Abe, T. Iida, M. Ikeda, K. Kobayashi, Y. Koshio, A. Minamino, M. Miura, S. Moriyama, M. Nakahata, *et al.*, "Scintillation yield of liquid xenon at room temperature," *Nuclear Instruments and Methods in Physics Research Section A: Accelerators, Spectrometers, Detectors and Associated Equipment*, vol. 594, no. 2, pp. 148–154, 2008.

[168] W. Andreoni, F. Perrot, and F. Bassani, "Excitons in large-gap insulators: Solid neon," *Physical Review B*, vol. 14, no. 8, p. 3589, 1976.

[169] N. I. for Standards and Technology, "Atomic data for samarium." Online.

[170] J. Emsley *et al.*, *Oxford Chemistry Guides*. 1991.

[171] L.-G. Tao, N. Kleshchina, R. Lambo, A. Buchachenko, X.-G. Zhou, D. Bezrukov, and S.-M. Hu, "Heat-and light-induced transformations of yb trapping sites in an ar matrix," *The Journal of chemical physics*, vol. 143, no. 17, p. 174306, 2015.

[172] J. Eden, B. Cherrington, and J. Verdeyen, "Optical absorption and fluorescence studies in high pressure cesium-xenon mixtures," *IEEE Journal of Quantum Electronics*, vol. 12, no. 11, pp. 698–704, 1976.

[173] W. West, P. Shuker, and A. Gallagher, "The effects of multiperturber interactions on the sodium–rare gas excimer bands," *The Journal of Chemical Physics*, vol. 68, no. 8, pp. 3864–3877, 1978.

[174] A. Tam, T. Yabuzaki, S. Curry, and W. Happer, "Visible excimer bands of the k-noble-gas and na-noble-gas molecules: Comparison of experiment with theory," *Physical Review A*, vol. 18, no. 1, p. 196, 1978.

[175] N. J. Turro, V. Ramamurthy, V. Ramamurthy, and J. C. Scaiano, *Principles of molecular photochemistry: an introduction*. University science books, 2009.

[176] G. Moe, A. Tam, and W. Happer, "Absorption studies of excimer transitions in cs-noble-gas and rb-noble-gas molecules," *Physical Review A*, vol. 14, no. 1, p. 349, 1976.

[177] D. V. Seletskiy, S. D. Melgaard, S. Bigotta, A. Di Lieto, M. Tonelli, and M. Sheik-Bahae, "Laser cooling of solids to cryogenic temperatures," *Nature Photonics*, vol. 4, no. 3, pp. 161–164, 2010.

[178] D. V. Seletskiy, R. Epstein, and M. Sheik-Bahae, "Laser cooling in solids: advances and prospects," *Reports on Progress in Physics*, vol. 79, no. 9, p. 096401, 2016.

[179] W. Griffith, M. Swallows, T. Loftus, M. V. Romalis, B. Heckel, and E. Fortson, "Improved limit on the permanent electric dipole moment of hg 199," *Physical review letters*, vol. 102, no. 10, p. 101601, 2009.

[180] P. Ferrario, V. Herrero-Bosch, J. M. Benlloch-Rodriguez, C. Romo-Luque, and J. J. Gomez-Cadenas, "Petalo: Time-of-flight pet with liquid xenon," in *2018 IEEE Nuclear Science Symposium and Medical Imaging Conference Proceedings (NSS/MIC)*, pp. 1–2, IEEE, 2018.

[181] W. Shockley and J. Pierce, "A theory of noise for electron multipliers," *Proceedings of the Institute of Radio Engineers*, vol. 26, no. 3, pp. 321–332, 1938.

[182] C. Spindt and K. Shoulders, "Stable, distributed-dynode electron multiplier," *Review of Scientific Instruments*, vol. 36, no. 6, pp. 775–779, 1965.

[183] G. Goodrich and W. Wiley, "Continuous channel electron multiplier," *Review of Scientific Instruments*, vol. 33, no. 7, pp. 761–762, 1962.

[184] M. Kristo and C. Enke, "Channeltron electron multiplier handbook for mass spectrometry applications," 1991.